Formation and Field-switching Dynamics of Nematic Droplets

by

Fred Fu

A thesis
presented to the University of Waterloo
in fulfillment of the
thesis requirement for the degree of
Master of Applied Science
in
Chemical Engineering (Nanotechnology)

Waterloo, Ontario, Canada, 2017

This thesis consists of material all of which I authored or co-authored: see Statement of Contributions included in the thesis. This is a true copy of the thesis, including any required final revisions, as accepted by my examiners.

I understand that my thesis may be made electronically available to the public.

Statement of Contributions

Chapter 4 of this thesis contains the results of a study, to which I made major contributions, that was performed in collaboration with Pouya Khayyatzadeh, who conceived the idea for the work. It is reproduced here with his permission. The work was originally published in: P. Khayyatzadeh, F. Fu, and N. M. Abukhdeir. *Physical Review E*, 92(6):062509, 2015.

All other work in this thesis was performed by myself under the supervision of Professor Nasser Mohiedden Abukhdeir. Figures from external sources have been used with permission according to their respective licenses.

Abstract

Liquid crystals (LCs) refer to a class of materials which have anisotropic properties. They are used in many technological applications ranging from displays to biological sensors. One example of a category of technologically relevant LC applications is optical functional materials, which include polymer-dispersed liquid crystal (PDLC) films. In these films, non-deformable micron-scale LC droplets are dispersed in a solid polymer matrix. Application of an electric field through the thickness of a PDLC film results in "switching" between a transparent "on" state (field-on) and a translucent "off" state (field-off). Thus the main application of these films are as switchable windows. Key to this mechanism is the ability for external fields to reorient the direction LC molecules within the droplets.

In this work, the LC phase formation and external electric field-switching dynamics of orientationally-ordered LC droplets are studied using the continuum Landau–de Gennes model. The model is able to capture phase transition and reorientation dynamics on device-relevant length and time scales when combined with numerical methods such as the finite element method. Formation dynamics correspond to transitioning from a high-temperature disordered liquid phase to an orientationally-ordered phase referred to as a nematic LC. Field-switching dynamics correspond to the imposition and release of an external (electric) field. Particular emphasis is placed on non-spherical droplets, which may form naturally or intentionally under controlled conditions in the manufacturing of PDLC films. The interactions between shape, LC/polymer interfacial effects, electric field strength, and other parameters are first investigated for capillary geometries using a simplified model, which is then followed by fully three-dimensional droplet simulations.

Finally, simulation results predicting a symmetry-breaking phase transformation process for spherical droplet domain are presented. This observation is found to be predicted when using physically-realistic material parameters approximating the LC compound pentyl-cyanobiphenyl (5CB), but not for simulations with a typical simplification of nematic elasticity known as the single elastic constant approximation.

Acknowledgements

Firstly, I would like to express my gratitude to Professor Nasser Mohiedden Abukhdeir for his extensive support throughout (as well as prior to) my graduate studies. I am deeply grateful for his mentorship during this experience.

Thank you also to Dr. Jun-ichi Fukuda, who hosted me during the summer of 2016 at the National Institute of Advanced Industrial Science and Technology (AIST) in Tsukuba, Japan.

I would also like to thank Pouya Khayyatzadeh for taking the initial steps that culminated in this work and Angela Krone for her contribution to writing the code for generating the three-dimensional droplet visualizations. Thank you also to Ryan Neufeld and Tanyakarn Treeratanaphitak for many insightful discussions and advice regarding Python and FEniCS, as well as to all of the members of the Computational Multiphysics Research Group (CMRG) for their moral support (and office chitchat).

Finally, let me acknowledge the following external sources of funding that helped to support this research and improve my quality of life over these past two years: the Natural Sciences and Engineering Research Council of Canada (NSERC), the Waterloo Institute for Nanotechnology (WIN), and the Ontario Graduate Scholarship (OGS) program. Last but not least, I would not have been able to carry out this work without the computing resources of the Shared Hierarchical Academic Research Computing Network (SHARCNET) and Compute Canada.

Dedication

To my family.

Table of Contents

List of Tables

List of Figures

List of Symbols

The following is a list of commonly used symbols in this thesis which appear multiple times. Note that tensors can be expressed using both Gibbs (boldface) notation ($\mathbf{Q}$) and index notation (Q_{ij}). SI units are indicated in parentheses where applicable.

α	Surface anchoring strength ($\mathrm{J/m^2}$)
$\boldsymbol{\delta}$	Identity tensor
$\epsilon_{\parallel}$	Relative dielectric permittivity parallel to the director
$\epsilon_{\perp}$	Relative dielectric permittivity perpendicular to the director
λ_e	Characteristic length of electric field ($\mathrm{m^3}$)
λ_n	Nematic coherence length ($\mathrm{m^3}$)
λ_s	Characteristic length of surface anchoring ($\mathrm{m^3}$)
μ_r	Rotational viscosity ($\mathrm{Ns/m^2}$)
$\mathbf{E}$	Electric field vector ($\mathrm{V\,m^{-1}}$)
$\mathbf{k}$	Surface unit normal vector / easy axis of anchoring
$\mathbf{n}$	Nematic director
$\mathbf{n}_d$	Droplet director
$\mathbf{Q}$	Second-order alignment tensor
$\mathbf{Q}_d$	Droplet order parameter

$\mathbf{x}$	Position vector
A	Surface area of domain (m^2)
a_0	Coefficient in Landau–de Gennes bulk free energy density ($\mathrm{J/m^3/K}$)
b	Coefficient in Landau–de Gennes bulk free energy density ($\mathrm{J/m^3}$)
c	Coefficient in Landau–de Gennes bulk free energy density ($\mathrm{J/m^3}$)
E	Electric field strength ($\mathrm{V\,m^{-1}}$)
E_c	Critical electric field strength ($\mathrm{V\,m^{-1}}$)
F	Total free energy (J)
f_b	Bulk or thermodynamic free energy density ($\mathrm{J/m^3}$)
f_s	Surface free energy density ($\mathrm{J/m^2}$)
f_{el}	Landau–de Gennes elastic free energy density ($\mathrm{J\,m^{-1}}$)
f_e	Electric free energy density ($\mathrm{J/m^3}$)
k_i	Frank-Oseen elastic constants — k_{11} / k_{22} / k_{33} / k_{24} ($\mathrm{J\,m^{-1}}$)
L_i	Landau–de Gennes elastic constants — L_1 / L_2 / L_3 / L_{24} ($\mathrm{J\,m^{-1}}$)
P	Biaxial order parameter
R	Aspect ratio (of ellipse or spheroid) in Chapters 4 and 5 Droplet radius in Chapters 2 and 6 (m)
S	Uniaxial/scalar order parameter
S_d	Droplet scalar order parameter
S_{eq}	Bulk equilibrium value of S
t	Time (s)
V	Volume of domain (m^3)
T	Temperature (K)

T_{ni} Nematic-isotropic phase transition temperature (K)

T_{ni}^{*} Supercooling temperature used in Landau–de Gennes model, slightly below T_{ni} (K)

Chapter 1

Introduction

1.1 Research Motivation

Liquid crystals (LCs) are phases of matter between that of a liquid and crystalline solid, consisting of anisotropically-shaped molecules which flow similarly to a liquid but possess some degree of orientational and translational order. This results in an inherent anisotropy of their material properties which has resulted in their application to several technological areas. Most notably, LCs are optically tunable—application of an external field is capable of reorienting the internal molecular arrangement or LC "texture", which in turn affects how light propagates within the material [1].

While the most commercially successful application of LCs, liquid crystal displays, are likely to be familiar to the reader, other LC-based technologies also exist. In particular, there are many novel composite materials which incorporate non-deformable liquid crystal droplets dispersed in polymer matrix [2]. These so-called polymer-dispersed liquid crystals (PDLCs) have been incorporated into various applications, including flexible displays [3, 4], holographic recording media [5], and switchable windows [6]. The last application, which is also known as "smart" glass, involves the application of an electric field to a PDLC film. Application of the field switches the device from an optically translucent ground state to a transparent field-driven state, which occurs due to the reorientation of the LC texture within the dispersed droplets [6]. While this technology has achieved some commercial interest, it still requires further study in order to be successful in the marketplace [7].

Liquid crystal droplets such as those present in PDLCs also offer a means to study the fundamental physics of LC confinement, which is a major area of interest [8]. Small

micron-scale droplets are a convenient means of studying the interactions between surface and bulk effects in LCs and topological defects present within LC droplet texture [9]. Ultimately, both the texture and reorientation behaviour within a confined LC domain depends on a complex, coupled set of parameters, including droplet size and shape, surface energy, LC material parameters, and applied external field.

In contrast to experiments, computer simulations have the ability to easily traverse this large parameter space. A particular challenge is that the effects of nanoscale droplet size and anisotropic droplet shape are difficult to study experimentally. Traditional analytical techniques for determining LC texture have been limited to observations of micron-scale features and have low temporal resolution. Simulations, however, have proven invaluable for predicting new LC-based phenomena and correcting inaccurate assumptions related to droplet structure. Unfortunately, many model simplifications are often used in past LC simulations from the literature, which can be detrimental to the quality of any obtained results. In order for simulation results to be relevant to not only fundamental physics, but also to engineering applications, these simplifications must also be addressed.

1.2 Objectives

The overall goal of this work is to study the formation and electric field-switching dynamics of non-deformable nematic liquid crystal droplets, such as those found in PDLC films. The theory used for simulations is continuum-based in order to capture phenomena at experimentally-relevant length and time scales. Specific objectives include:

1. Implementing a numerical solver for the transient three-dimensional nonlinear partial differential equation system resulting from the continuum model.

2. Implementing enhancements to the continuum model which take into account typically neglected nematic phenomena such as simulation of nematic phase formation, "weak" surface anchoring, and differences in nematic elasticity.

3. Studying the effects of anisotropy in domain shape, such as in elliptic capillaries (2D) and spheroids (3D), on nematic phase formation and electric field-switching dynamic mechanisms, including any relevant time scales.

4. Analyzing simulations results using quantitative metrics such as volume-averaged order parameters and canonical nematic deformation modes (splay, twist, bend, saddle-splay).

This thesis is organized into seven chapters. First, background material is presented in Chapter 2, which covers the fundamentals of liquid crystals, and Chapter 3, which discusses the basis for the employed continuum model and its numerical implementation. Next, results are given for phase formation and field-switching simulations of LCs confined to elliptic capillaries and spheroid-shaped droplets in Chapters 4 and 5, respectively. In Chapter 6, A novel dynamic phenomenon is observed for a spherical droplet when resolving certain model simplifications. Finally, conclusions and recommendations for future work are presented in Chapter 7.

Chapter 2

Background

2.1 Liquid Crystals

In 1888, Austrian botanist Friedrich Reinitzer observed that a certain plant cholesterol appeared to melt twice upon heating. The substance, now known to be cholesteryl benzoate, first melted from a solid phase to a cloudy liquid at 145.5 °C, and appeared to melt again into a clear liquid at 178.5 °C [10]. Today, we know that the intermediate cloudy phase which he first observed was actually an example of a *liquid crystal* phase: an intermediate state of matter with properties between a liquid and a crystalline solid.

More precisely, liquid crystals are distinguished from liquids and solids by their degree of molecular *order*. In general, order can be either *translational* (the tendency of molecules to have discrete translational symmetry) or *orientational* (the tendency of molecules to align in a certain direction). A crystalline solid has both types of order: the molecules are uniformly arranged in a tight lattice structure (translational order) and their orientation is similarly correllated across long distances with respect to the molecular scale (orientational order). In contrast, a disordered or *isotropic* liquid has neither translational or orientational order: while the molecules are still closely packed, they are randomly distributed and have random orientation. Liquid crystals phases have characteristics somewhere in between these two states [1].

Given this broad definition, it should not be surprising that there is no single liquid crystal phase. Instead, a broad range of different liquid crystal phases, called *mesophases*, exist which involve variations in translational and orientational order. The observation of these mesophases is influenced by the chemistry of the liquid crystal molecule or *mesogen*.

Generally, all mesogens are associated with some sort of structural or shape anisotropy [1]. An example of this is the rod-like liquid crystal pentyl-cyanobiphenyl (5CB), shown in Figure 2.1, which is a very well-studied mesogen that is often used in research. While the molecule is not perfectly symmetric, 5CB and other similar mesogens are often depicted as cylindrical rods or ellipsoids due to the presence of the cyanobiphenyl group which imparts a degree of rigidity to the molecule [1].

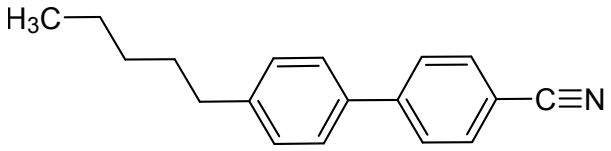

Figure 2.1: Molecular structure of pentyl-cyanobiphenyl (5CB).

Liquid crystals such as 5CB are *thermotropic*: the phase transitions between the liquid, liquid crystal, and solid phases are most dependent on temperature. This is demonstrated in Figure 2.2, which shows various phases being exhibited at different temperature ranges. At the higher end of the temperature spectrum, the *nematic* phase is characterized by high orientational order but translational disorder. As a result, molecules in this phase tend to self-align but still remain fluid, without any long-range correlation between the positions of the molecules. At the lower end of the spectrum, *smectic* phases, in addition to high orientational order, also possesses translational order, as demonstrated by the tendency for molecules in this phase to form distinct layers. The alignment within each layer can be either perpendicular to the plane of the layer (smectic A) or tilted (smectic C). While smectic phases still maintain fluidity, they are typically more viscous than the nematic phase. Figure 2.2 also indicates the nematic-isotropic transition temperature T_{ni}, which marks the temperature of the first-order (discontinuous) phase transition between the nematic (high orientational order) and isotropic (zero order) phases of a thermotropic LC.

While a myriad of other mesophases have been discovered, this work will primarily focus on rod-like thermotropic nematic liquid crystals, which are the most relevant to the outlined objectives. These types of LCs are relatively simple to model and have historically been the most technologically successful.

2.2 Molecular Description

On the molecular scale, a nematic liquid crystal (NLC) system can be approximated by a collection of cylindrical rods representing individual mesogens. Each rod is described by

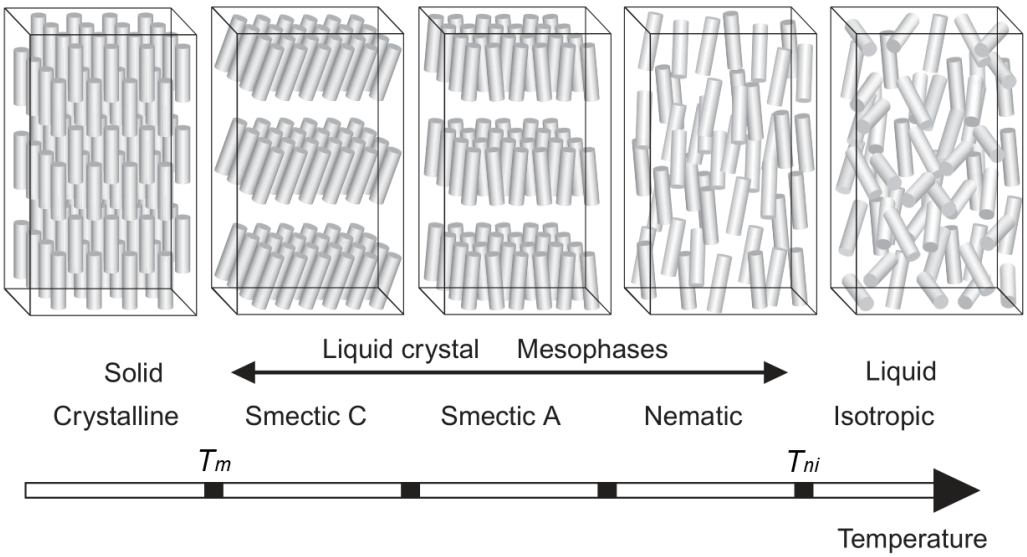

Figure 2.2: Possible phases that could be exhibited for a rod-like thermotropic mesogen. From ref. [10].

its position and the orientation of its axis of symmetry. As depicted in Figure 2.3a, the orientation can be represented with respect to a fixed coordinate system by a polar angle θ and azimuthal angle ϕ. Locally, these rods will tend to align parallel or antiparallel to each other due to the presence of intermolecular forces between them as well as for entropic reasons [11], resulting in short-range orientational order. A snapshot of a local group of rods can be collectively described by an orientational distribution function $f(\theta, \phi)$. However, it would be much more concise to be able to characterize this system using scalar or vector order parameters. One possibility is to use the average orientation of the rods, represented by a vector $\mathbf{n}$ called the director. This description is shown in Figure 2.3b.

However, $\mathbf{n}$ alone is insufficient to describe the state fully, since it does not characterize the *degree* of alignment of the rods (i.e. the orientational order). For example, consider Figure 2.4, in which the orientational distribution function in Figure 2.4b is more diffuse than the one in Figure 2.4a. To address this, an order parameter S can be defined in which $S = 0$ corresponds to the isotropic phase and $S = 1$ corresponds to a fully aligned nematic. If the orientational distribution of the molecular long axes is uniform about the director (referred to as *uniaxial*), then we can ignore the azimuthal angle ϕ and represent this by the following expression [1]:

$$S = \frac{1}{2}\langle 3\cos^2\theta - 1\rangle = \int_0^\pi f(\theta)\frac{1}{2}(3\cos^2\theta - 1)\,d\theta \tag{2.1}$$

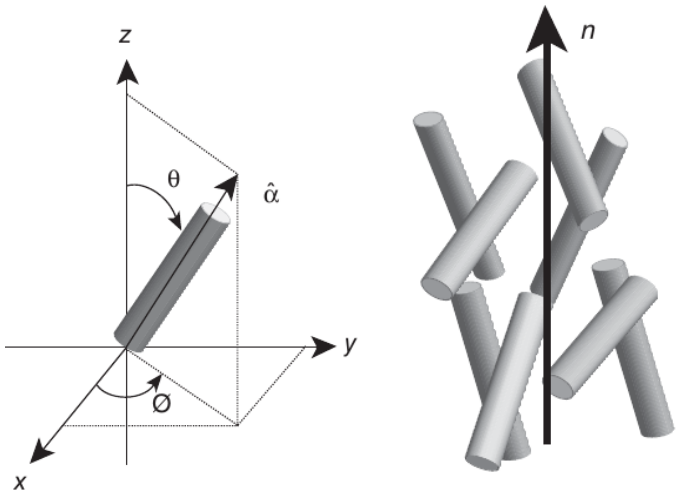

(a) (b)

Figure 2.3: Molecular order in a nematic liquid crystal. (a) Orientation of a single mesogen. (b) A local group of mesogens represented by the director **n**. From ref. [10].

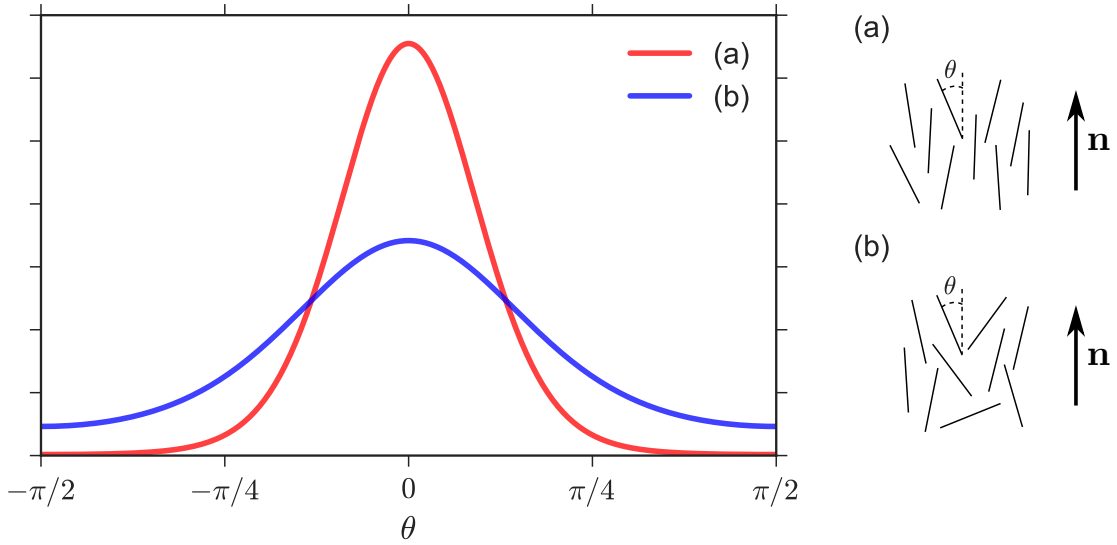

Figure 2.4: Comparison of two different orientational distribution functions $f(\theta)$ with the same director **n**. The distribution in (b) is more diffuse (lower S) than the one in (a). Based on ref. [12].

which is known as a second-order Legendre polynomial. The angled brackets indicate an ensemble average over the rods. S is called the *uniaxial* or *scalar order parameter* and is a scalar value which represents the degree of alignment. Most liquid crystals have bulk values of $S = 0.3$–0.8 [1].

If we omit the assumption of a uniaxial distribution of molecules, then the orientational distribution function also permits *biaxiality*. For a biaxial system, no single axis of rotational symmetry about $\mathbf{n}$ is assumed. Instead, two perpendicular axes of rotational symmetry can exist: this is analogous to a rotation which traces an elliptical orbit about a central axis instead of a circular one. This occurs despite each rod still maintaining its own individual cylindrical symmetry (rods which are biaxially symmetric comprise a separate class of liquid crystals called biaxial nematics, which are still an emerging area of research [13]).

Across longer length scales in an NLC domain, short-range interactions are no longer dominant and therefore the director and degree of orientational order may vary in space. If time is also included, then a full NLC system can be roughly approximated by a vector field $\mathbf{n}(\mathbf{x}, t)$ and scalar field $S(\mathbf{x}, t)$, where $\mathbf{x}$ represents a position vector within the entire domain. This description of liquid crystals is the basis for a *continuum model*, in which a liquid crystal domain is modelled as a continuous medium (instead of by its discrete molecules). Because the individual molecular orientations are "averaged" out, these theories are unable to simulate physics near the molecular scale compared to atomistic or molecular methods (e.g. molecular dynamics). However, they are very useful for studying device-relevant phenomena, which occur across much larger length and time scales.

The majority of modelling approaches for NLCs use two types of continuum theories distinguished by the order parameters they are based on: Frank-Oseen theory and Landau–de Gennes theory. Frank-Oseen theory is a solely *elasticity*-based approach. Just as the elastic energy of a spring depends on its relative position to equilibrium, the theory describes the free energy of an NLC system based on spatial and temporal variations in the director $\mathbf{n}$. In contrast, Landau–de Gennes theory accounts for phase transition phenomena and biaxiality in addition to nematic elasticity, through the use of a more descriptive tensor order parameter, the alignment tensor $\mathbf{Q}$. These models will be described further in Chapter 3.

2.3 Properties

Following from their microscopic behaviour, NLCs exhibit several unique macroscale properties which make them especially useful for engineering applications. The major properties of NLCs arise from their anisotropic rod-like shape, resulting in various orientation-dependent behaviour. For example, mesogens undergo different polarizations in an electric

field depending on whether the field is applied parallel to the director (along the axis of symmetry of the molecules) or perpendicular to it [1]. Since light is an electromagnetic wave, this anisotropy in electric susceptibility means liquid crystals are *birefringent*: there are two transmission axes which each possess a different index of refraction [1]. This allows liquid crystal domains to change the polarization state of light, acting as optical waveguides.

Birefringence also forms the basis for *polarized optical microscopy* (POM), an analytical technique used to analyze orientation in liquid crystal samples. In POM, liquid crystal samples are placed in between two linear polarizers oriented perpendicular to each other. The sample is then illuminated and images are taken. Normally, unpolarized light shining through these crossed polarizers is completely absorbed; however, because the samples act as waveguides, only areas where the mesogens are oriented parallel or perpendicular to the crossed polarizers appear dark. This concept is illustrated in Figure 2.5, and Figure 2.6 shows an image of a typical NLC sample. Researchers have traditionally relied on POM as the sole way of probing the orientation of liquid crystals; however, more sophistocated imaging technologies such as confocal fluorescence microscopy [14] and deuterium magnetic resonance imaging [15] have recently been developed. Ultimately, the ability to probe the orientation of a NLC domain is important in the context of the simulation results that will be discussed later in this work.

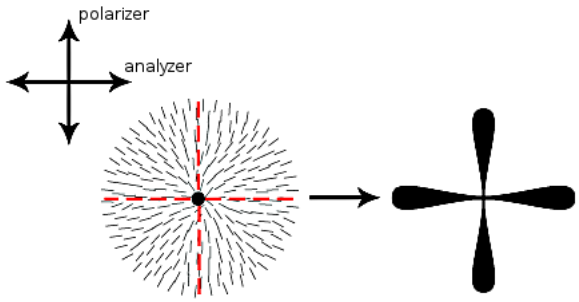

Figure 2.5: Schematic of a director field (left) and corresponding bright and dark regions (right) when viewed between crossed polarizers. From ref. [16].

Another unique property of liquid crystals that arises from their anisotropic electric susceptibility is that their orientation can be controlled using an external field [1]. The application of an electric field creates an induced polarization in the molecules and can result in a torque. The *Freedericksz transition* refers to a phenomenon where, above a critical electric field strength, an applied electric field will cause a significant distortion in the orientation of an NLC domain. The director can either align parallel or perpendicular to the applied field depending on the dielectric anisotropy of the liquid crystal. Most common

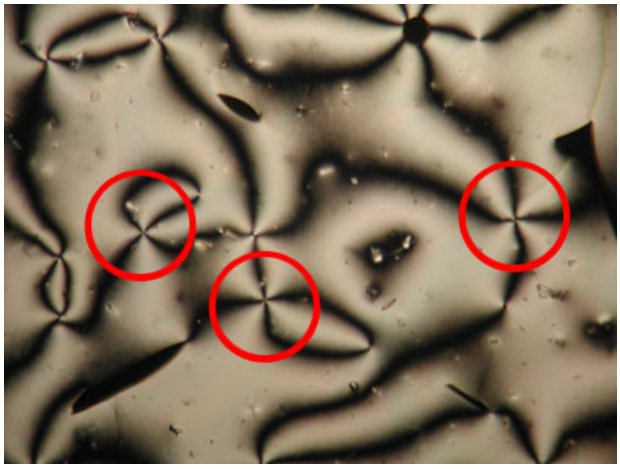

Figure 2.6: A nematic liquid crystal cell viewed under polarized optical microscope. Circled regions indicate areas where there exists a singularity in orientation. From ref. [16].

liquid crystals, including 5CB, have positive dielectric anisotropy and will align in the direction of an applied field.

In addition to applying an electric field, the director can also be controlled or *anchored* through surface interactions. The two major types of liquid crystal alignment with respect to a surface are *homeotropic* in which the director is parallel to the surface normal and *planar* in which the director is perpendicular to the surface normal [1]. Planar anchoring can also be classified as *degenerate*, which describes when the director is free to align in any direction along the surface (as opposed to favouring a single in-plane direction) [17]. The strength and type of surface anchoring depends on the exact interfacial interactions between the chosen surface material and liquid crystal [18], although common "recipes" exist for aligning NLCs in specific ways. A simple but popular technique involves applying a thin polyimide coating to the surface and rubbing it, which creates microgrooves in the polymer that encourage planar anchoring in the rubbing direction [1]. The surface can also be coated with surfactant molecules such as lecithin, which can encourage homeotropic anchoring [19]. These two methods are illustrated in Figure 2.7.

Both electric field and surface effects are significant because they may result in the formation of nematic defects, commonly referred to as *disclinations*. Analogously to dislocations in crystals, which are imperfections in lattice geometry, disclinations in liquid crystals can be considered imperfections in orientation [1]. Disclinations are singularities or discontinuities in the director field where there is an abrupt change in molecular orientation and can take the form of points, lines, or surfaces. Microscopically, they correspond to a

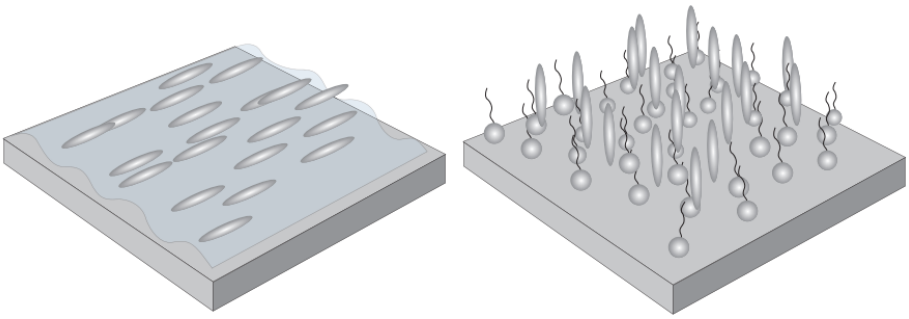

Figure 2.7: Schematic of planar anchoring along a single direction induced by rubbing a polyimide layer (left), and homeotropic anchoring induced by surfactant molecules (right). From ref. [20].

decreased degree of alignment S and increased biaxiality P in the region of the defect [21].

Figure 2.8 shows the four main types of disclinations that are observed in nematics. Disclinations are classified by their strength or charge s, which is defined by the angle that the director rotates when looping around it, divided by 2π (a full rotation), with the sign being dictated by whether the angle is changing along the direction of the loop [22]. For example, when traversing a loop around the defect clockwise, for $s = +1$, the director rotates also 2π clockwise. In contrast, for $s = -1$, the director rotates 2π counter-clockwise, and only π counter-clockwise for $s = -\frac{1}{2}$. Topology theory dictates that when two disclinations of the same strength and opposite charge meet, they can cancel each other out [14]; therefore, for small systems in an equilibrium configuration, it is often rare to observe multiple defects.

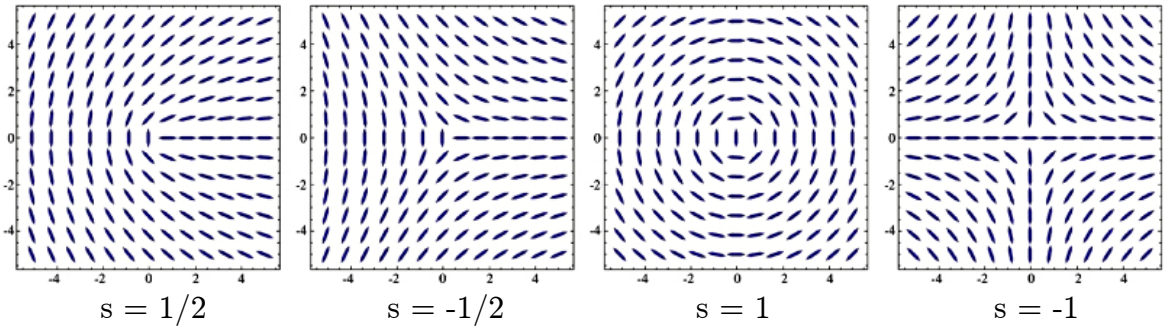

Figure 2.8: Director fields for the different defect types observed in nematic liquid crystals. From ref. [23].

One category of physical structures which are able to form stable disclinations, however,

is NLCs confined to curved droplet geometries. For these cases, the combination of the curvature of the domain and the imposed anchoring at the surface constrain the director and can prevent it from relaxing to a uniform state. Depending on various conditions, including the size and shape of the droplet, the anchoring imposed by the outer surface, and the properties of the mesogen [24], the NLC can take on different structural configurations within the droplet. A wide array of these director configurations (called nematic *textures*) have been observed, such as those shown in Figure 2.9 for spherical droplets. Of these, the most well-known are the *bipolar* configuration for planar anchoring (Figure 2.9a), which has a defect at each pole of the droplet, and the *radial* configuration for homeotropic anchoring (Figure 2.9e), which has a single defect in the center of the droplet. These textures are known through both experiment (using POM, for example) [25, 26] and computer simulation [27].

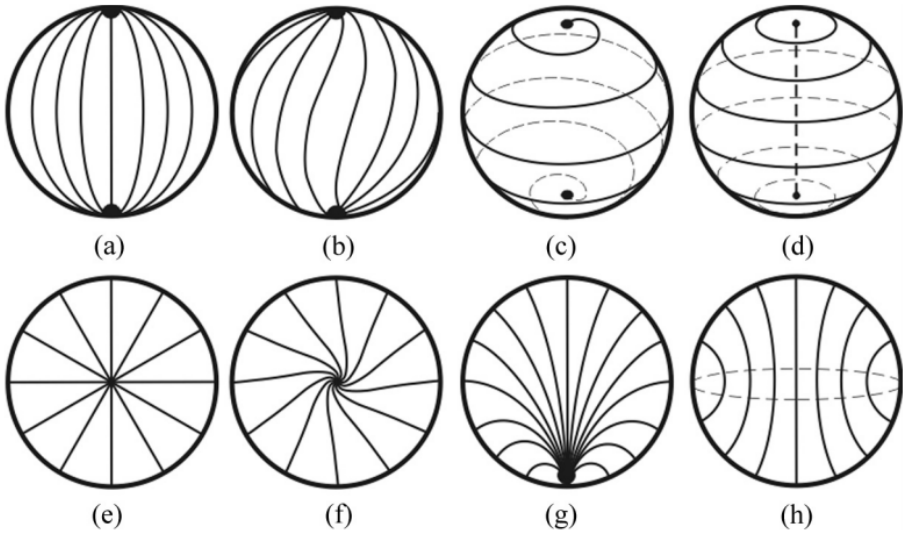

Figure 2.9: Various possible nematic textures for spherically confined nematic droplets with lines indicating the director field. From ref. [28].

2.4 Applications

Traditional liquid crystal display (LCD) technology relies on uniform defect-free domains, which constitute the individual pixels that make up the screen used in computer monitors or television sets. For these applications, defects are undesirable since they contribute to a loss of display resolution and can create undesirable optical effects [29]. However,

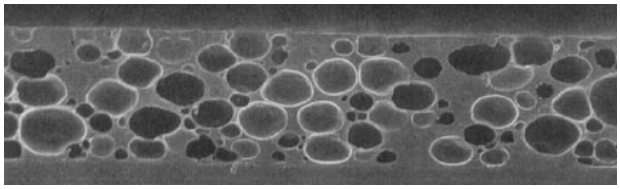

Figure 2.10: Scanning electron microscope image of a cross-section of a PDLC film formed by emulsion polymerization. From ref. [6].

more recent applications have been able to leverage domains which contain disclinations. *Polymer-dispersed liquid crystals* (PDLCs) are composites consisting of dispersed liquid crystal droplets in a polymer matrix [6]. Since their discovery, the term PDLC has expanded to several different types of materials ranging from the simplest case of dispersed NLC droplets within polymer to a complex layered polymer and liquid crystal structure called a holographic PDLC or H-PDLC, which can be used as a diffraction grating for optoelectronic applications such as holograms [7]. Recently, PDLC films containing handlebody-shaped nematic structures have also been proposed, resulting in complex but defect-free textures [30]. More intricate soft lithography or photopolymerization approaches may be exploited to obtain drops with more geometrically complex structures [30].

A significant benefit of PDLC films over regular displays is that they are easy to manufacture at large scales: a common "bottom-up" method is to create a homogeneous mixture of LC and melted polymer and then quench it (thermally-induced phase separation) leading to the formation of micron-sized LC droplets in solid polymer matrix [31]. These confined LC domains stretch upon phase separation, causing them to have a slightly anisometric spheroidal shape [32], as shown in Figure 2.10; however, this can depend widely on the method used to manufacture the film. Phase separation processes, for example, tend to produce mostly spherical droplets [33].

Due to their liquid crystalline nature, PDLC films possess unique electro-optical properties which allow them to be used as light shutters. In the absence of an electric field, the micron-sized nematic LC droplets are all oriented in random directions, causing the film to scatter light and appear translucent. However, when an electric field is applied through the film, the LC molecules in the droplets to align in the same direction. If the device is engineered such that the index of refraction of the LC droplets and the polymer matrix match, then light can pass through the film unscattered and the film appears transparent [7]. This operation is illustrated in Figure 2.11.

Using this phenomenon, PDLCs were commercialized to create switchable windows for rooms and buildings, as demonstrated in Figure 2.12. Their main advantages over other

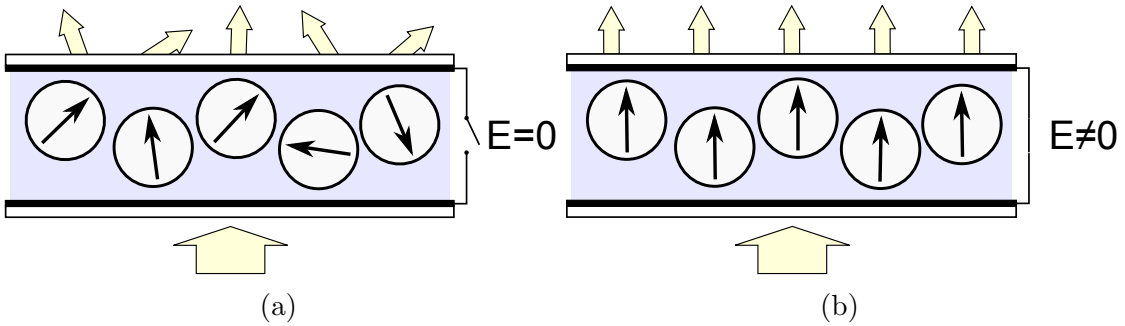

Figure 2.11: Schematic of the operation of a PDLC-based "smart" window where circles represent droplets, black arrows represent the average nematic director, and yellow arrows represent light. (a) Light is scattered by randomly oriented nematic droplets in the absence of an electric field (translucent mode), which when exposed to an external field, (b), become aligned in the direction normal to film (transparent mode). From ref. [34].

technologies are that they can be manufactured easily at large scales and do not require polarizers or backlighting to operate (unlike other LC display technology). Unfortunately, PDLCs are limited by their slow electro-optical switching times and imperfect transparency, which prevent them from being applied to traditional video display technology [7]. These parameters are governed by the speed and degree of switching within the individual droplets in the device [35].

The large-scale adoption of PDLC devices is still limited by the high cost of nematic liquid crystal and indium tin oxide (used as transparent electrodes), preventing them from being marketed at high volumes [37]. They are also being outpaced by electrochromic

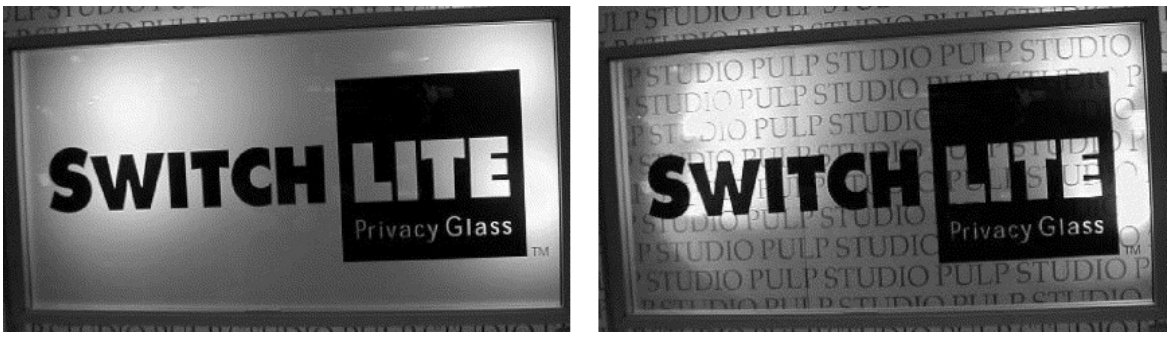

Figure 2.12: Switchable privacy glass: translucent (left) and transparent (right). From ref. [36].

materials due to their relatively high energy requirements [38]. As a result, significant optimization and a more fundamental understanding of PDLC devices are necessary.

2.5 Related Work

In order to identify promising areas of research and improve upon the existing body of literature, past approaches to simulation of NLC droplets, in the context of experimental work, must be discussed. In this section, a comprehensive literature review of relevant work is presented.

The first numerical analyses of liquid crystal droplets were performed using the Frank-Oseen model in 1969 by Dubois-Violette and Parodi [39] to predict the two previously-mentioned bipolar and radial textures, depending on the surface anchoring (planar and homeotropic) of the droplet and the presence of an external field. Since then, many more textures have been discovered, but this work will restrict itself to study of homeotropically-anchored droplets. Firstly, homeotropic anchoring is simpler to consider from a technical perspective since it directly imposes a fixed director at the surface. In contrast, degenerate planar anchoring allows for the director at the surface to be oriented in an infinite number of directions perpendicular to the surface normal vector. Secondly, studies of field-switching dynamics in bipolar droplets have been more common in the literature [40, 41], despite the fact that homeotropically-anchored droplets are still experimentally relevant.

The prediction for the radial texture, which has a +1 point disclination in the centre of the droplet, appears to be easily confirmed by POM images [42], which show the expected brush pattern for a +1 defect (Figure 2.8). However, numerical study by several groups using the Landau–de Gennes model indicated that this +1 disclination is energetically unstable compared to a small $+\frac{1}{2}$ disclination loop [43–47] shown in Figure 2.13. Kralj and Virga [47] determined that the size of this nanoscopic loop defect remains constant (on the order of 10 nm) as droplet radius R increases above a threshold ($R \gtrsim 100\,\text{nm}$). Furthermore, outside of the region of the defect, the overall droplet texture does not significantly change. This explains why these loop defects are unobservable by optical methods. Mkaddem and Gartland [48] found that changing the temperature and elastic parameters can affect the size of the loop, e.g. causing it to increase as T_{ni} is approached. Further study of the defect ring size dependence by Kanke and Sasaki [49] provided additional agreement with these earlier findings.

Depending on the strength of the surface anchoring and size of the droplet, droplets may also be uniformly aligned and have no defect at all: in this way, the droplet minimizes its

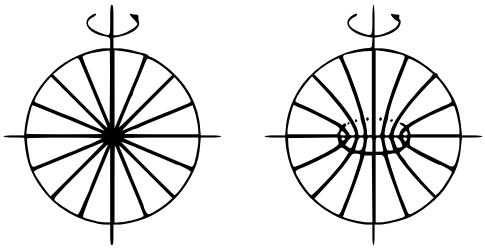

Figure 2.13: Schematic of predicted director fields for homeotropically-anchored droplets. The texture on the right containing a disclination loop (enlarged for clarity) is more stable than the one on the left which contains a point defect. From ref. [48].

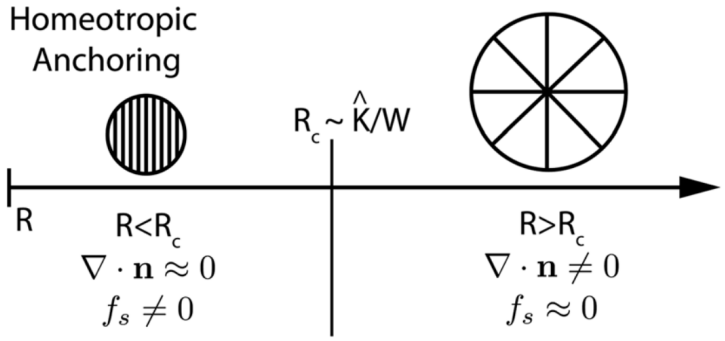

Figure 2.14: Schematic of the size-dependent radial-to-uniform transition in homeotropically-anchored droplets as size decreases. Large droplets above a critical radius R_c exhibit nonzero deformation and satisfy the boundary conditions (as indicated by $\boldsymbol{\nabla \cdot \mathbf{n}}$ and surface penalty f_s), and vice-versa for droplets below R_c. From ref. [52].

elastic energy at the expense of surface anchoring. This is common in submicron droplets, which have smaller surface-to-volume ratio [50]. Lavrentovich [51] explained this using dimensional analysis: in liquid crystals, elasticity scales *linearly* with droplet radius R, instead of proportionally to the volume R^3. Surface energy scales proportionally to the surface area of the droplet as R^2, however. Figure 2.14 illustrates this. As a result, larger droplets are more likely to orient according to the defined surface anchoring, leading to the formation of defects, while smaller droplets attempt to minimize their elastic deformation. This observation has been confirmed experimentally [50]. Some simulation studies which assume *fixed* homeotropic anchoring (forcing the nematic director at the droplet surface to be perfectly aligned with the surface normal—essentially simulating "infinitely" strong anchoring) were naturally unable to observe these defect-free textures [27, 48], despite

the use of the Landau–de Gennes model. This interplay between surface anchoring and elasticity demonstrates the complexity of studying nematic textures in droplets.

As PDLCs first started being developed, more focus was placed on studying electric field-switching of NLC droplets in order to improve PDLC technology (particularly light shutters). Early numerical simulations found that applying an electric field to a radial droplet with positive dielectric anisotropy above a critical field (i.e. a Freedericksz-like transition) results in a so-called *axial* texture with an equatorial defect loop (a defect loop along the equator of the droplet) (see Figure 2.9h) [53]. In this case, the electric field causes alignment of the droplet in the direction of the field at the expense of surface anchoring. If surface anchoring is weak enough, it has been predicted that an axial texture without defects (in which the defects escape through the surface) can form [54]. Bodnar et al. [55, 56] studied nematic texture switching experimentally under AC electric field, confirming the expected axial structure with equatorial defect loop above a critical field strength E_c. Ding et al. [57] also studied nematic texture with increasing electric field, observing very similar textures. They confirmed that reorientation of droplet texture due to a field is approximately a first-order transition (i.e. the texture only reoriented above a critical field strength). Furthermore, they observed a hysteresis effect where intermediate textures were different with increasing electric field strength versus decreasing electric field strength. A twisted radial texture also appeared as the field strength was increased but not as it was decreased.

De Groot and Fuller [58] measured the time evolution of electro-optical properties of a droplet suspension under electric field. The time of relaxation was found to be much shorter for radial droplets compared to bipolar ones (by a factor of 10), consistent with findings by Doane [59]. In contrast, Xie and Higgins [60] studied reorientation dynamics of single droplets in PDLC film using fluorescence microscopy and were able to observe droplet texture dynamically. They were able to measure the structural reorientation dynamics upon applying and releasing a constant electric field $E = 8.5\,\mathrm{V\,\mu m^{-1}}$ and measured a switching time of 4.8 ms and a relaxation time of 30 ms, which was slower than their observations for bipolar droplets. They attributed this result to differences in the strengths of the polymer-LC surface anchoring.

Komura et al. [61] used the Frank-Oseen model to investigate the radial-to-axial transition associated with the presence of a field, and varied elastic parameters and droplet size. Both Kilian [62] and Li and Chen [63] simulated switching with a simplified uniaxial Landau–de Gennes model (varying S but without biaxiality) and strong anchoring conditions, both observing an increase in alignment and defect ring size with increasing electric field. Kilian's results are shown in Figure 2.15. Li and Chen observed that release of the field returned the texture back to its original equilibrium state, while Kilian observed that the droplet

axis (aligned with the electric field) kept its orientation after the field was switched off. Li and Chen were able to observe hysteresis in the degree of orientational order within the droplet with respect to increasing and decreasing electric field strength, however. They observed that the droplet retains additional order as the field decreases, which qualitatively matches the experimental results.

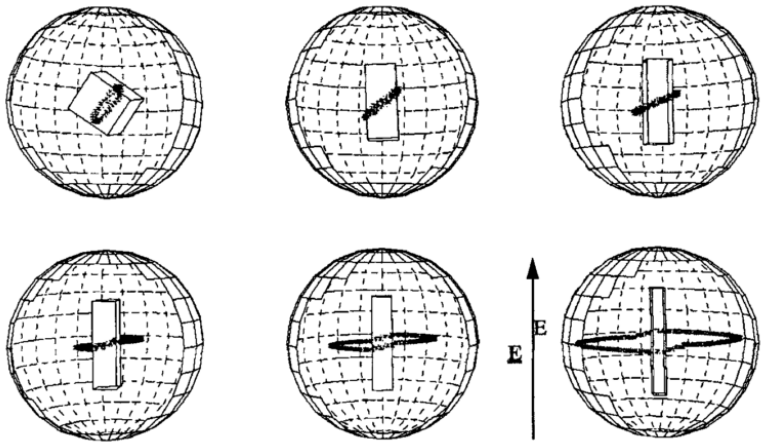

Figure 2.15: Simulation of electric-field switching for a radial droplet. The director field is not visualized; instead, a rectangular prism indicates the overall direction of alignment. The disclination loop is also shown (black). From ref. [62].

Most work in the field of liquid crystal droplets and PDLC films assumes that droplets are perfectly spherical. However, droplets in PDLC films can become deformed for various reasons. Small droplets can naturally form into elongated shapes called *tactoids* [64] in order to reduce their elastic deformation. The manufacturing technique can also affect droplet behaviour (as shown previously in Figure 2.10): in H-PDLCs for example, the polymerization process is biased in a single direction and ellipsoidal droplets are formed [5]. In addition, droplet shape anisometry can be directly controlled using various techniques [65,66], many of which are described in more detail in ref. [66]. The simplest of these methods is unidirectional mechanical stretching of the PDLC film to produce highly prolate spheroidal domains from PDLC films containing initially spherical droplets (Figure 2.16) [67, 68]. Once fully-formed, the shape of these spheroidal domains is non-deformable. This ability to control droplet shape size is significant, since it allows droplet shape to be incorporated as a parameter for engineering applications.

Experimental studies have indicated that non-spherical droplet shape, specifically anisometric shape, is a key factor in PDLC film relaxation time following release of the

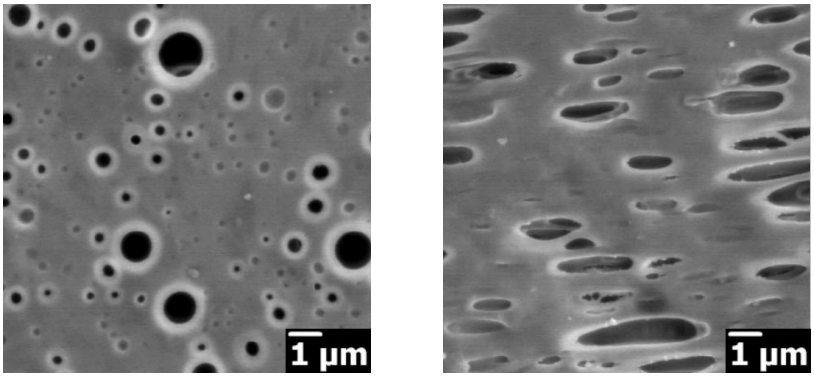

Figure 2.16: Scanning electron microscope images of (left) unstretched and (right) unidirectionally stretched PDLC film where the resulting droplet shape is anisometric. From ref. [67].

external field and can also help improve the optical properties of PDLC films [6, 66, 69]. However, the mechanism for this is still unclear. As discussed above, past simulation studies have typically focused on circular and spherical domains. While elliptic or ellipsoidal domains of homeotropically-anchored droplets have been studied before [32, 70], these works have relied on director-based models which poorly capture orientational defects and phase transition. Bharadwaj et al. [32] studied geometries corresponding to spheres, prolate and oblate spheroids, and ellipsoids and observe equilibrium textures under different electric field strengths assuming strong homeotropic anchoring. They conclude that ellipsoidal droplets switch more efficiently than spherical ones. Rudyak et al. [70] perform a study of solely oblate droplets and also include the effect of different anchoring strengths and suggest that the geometry reduces the electric field necessary for switching.

It is notable that despite the fact that dynamic quantities, such as switching times, are frequently studied in experiment for PDLCs, this aspect is typically neglected in simulation studies. Unlike molecular-scale simulation techniques such as molecular dynamics, which inherently involves time, most mesoscale simulation has focused on analyzing stable *equilibrium* textures [71]. This only requires minimization of the free energy, which can be accomplished without needing to introduce time as a parameter. For example, both Bharadwaj et al. and Rudyak et al. [32, 70] employ Monte Carlo-based techniques, which involve a non-physical traversal of parameter space until a free energy minimum is reached. Simulation studies can also use symmetry assumptions to reduce the computational complexity of a spherical droplet domain to a smaller (quadrant) domain with implied axial and mirror symmetry [48, 54, 72]. These symmetry assumptions prevent the simulation of electric field-switching dynamics, since the unidirectionality of the electric field can break

assumptions of rotational symmetry within the droplet texture. Of the work that does exist for dynamics, time scales of relaxation have been estimated for planar-anchored bipolar droplets [73] but not homeotropically-anchored radial droplets.

Finally, it is common in continuum simulations of liquid crystals to make simplifications for the elastic energy. The most common of these is the single elastic constant approximation, which assumes that the different elastic moduli used to model NLC elasticity are equal (e.g. [63, 74]), despite the fact that experimental data for liquid crystal materials indicates this is not valid [75]. While in many cases, it can be argued that this approximation is not harmful given the number of other approximations present when using simulation methods, correcting for this approximation does impact the quantitative interpretation of simulation results [76]. In some more extreme cases, textures can change significantly if this assumption is not made. For droplets, this can result in the "twisted" textures shown in Figures 2.9b and 2.9h [77, 78].

Overall, the following conclusions can be made, forming the basis for the work described in this thesis:

- There are advantages to using simulation in the study of the equilibrium and electric field-switching textures of droplets. Not only can simulations explore a wider range of parameter space, but they have also been shown to predict and explain NLC droplet-based phenomena.

- Prior simulation-based work make use of model simplifications and assumptions, including homogeneous orientational order and uniaxiality (Frank-Oseen model), fixed surface anchoring, the single elastic constant approximation, and assumptions of spherical symmetry. While these assumptions have resulted in significant progress in the field, they limit the ability of simulation-based methods to be applied to the rational, quantitative design of real PDLC-based devices.

- Promising avenues of research for NLC droplets still exist. Aspects such as shape anisotropy of droplets and *dynamic* simulations of droplet formation and switching (rather than just examining equililbrium textures) have yet to be studied thoroughly.

Chapter 3

Theory

For a model to be relevant to the simulation of PDLC droplets, it must be able to capture micrometre length scales and microsecond time scales. This precludes the use of atomistic or coarse-grained molecular methods (e.g molecular dynamics), which, despite recent increases in computing performance, are only capable of simulating nanoscale domains. As a result, *continuum theories* are the focus of this work. As mentioned in Chapter 2, these theories treat a liquid crystal domain as a continuous medium, instead of as discrete atoms or molecules. Continuum theories for NLCs are classified into two categories: *hydrostatic* and *hydrodynamic*. In a *hydrostatic* theory, the assumption is made that the NLC does not flow (velocity $\mathbf{v} = \mathbf{0}$), focusing on internal changes in orientation or *reorientation* dynamics. In contrast, a *hydrodynamic* theory captures both flow and reorientation dynamics [10]. In both types of theories, it is frequently assumed that the domain is isothermal. In this chapter, the two main hydrostatic continuum theories, Frank-Oseen theory and Landau–de Gennes theory, are presented and their differences with respect to modelling the free energy density of an NLC domain are discussed. Additionally, the numerical approach used to solve these models and perform simulations is presented.

3.1 Frank-Oseen Theory

In Chapter 2, the concept of the nematic director field $\mathbf{n}(\mathbf{x}, t)$ was introduced, which represents the average direction of LC molecules at each point in space. The model can be slightly simplified by constraining $\mathbf{n}$ to be equivalent to $-\mathbf{n}$ (the director is a "headless" vector). Note that this simplification is justified not only for non-polar mesogens but also

polar ones. Polar molecules will tend to align antiparallel and thus, when considered as a localized group, their polarity will effectively cancel out [10].

A phenomonological continuum theory was developed by Frank in 1958 [79] based on the director model for an NLC. This continuum theory, known as Frank-Oseen theory, is based on the concept of *elasticity*. Similar to compressing a spring from its equilibrium state, the Frank-Oseen model assigns energetic penalties to distorting an NLC from a fully-aligned equilibrium state (Figure 3.1a. As such, in the Frank-Oseen model, the Helmholtz free energy density of a uniaxial NLC is constructed by expanding gradients (spatial derivatives) in the director, which, when limited to first order derivatives, can eventually be simplified to a sum of independent elastic deformation modes. Typically, these modes are *splay*, *twist*, and *bend* and are illustrated in Figure 3.1b–3.1d [1, 79].

There is also an additional mode of distortion called *saddle-splay*, which can be described as similar to splay but along a saddle-like surface with negative Gaussian curvature [80]. This mode is unique in that its presence *reduces* the elastic energy of the system [51]. Mathematically, this term is represented by a divergence; as such, it can be converted from a bulk integral to a surface integral when considering the minimization of the total free energy. As a result, it is usually omitted when considering bulk phenomena or strongly anchored domains [81]; however, its significance in weakly-anchored confined systems with complex anchoring has been demonstrated in certain situations [52, 82, 83]. The final form of the free energy density is commonly given by (see ref. [81]) for derivation) [84]:

$$f_f = \underbrace{\frac{1}{2}k_{11}(\boldsymbol{\nabla}\cdot\mathbf{n})^2}_{\text{splay}} + \underbrace{\frac{1}{2}k_{22}(\mathbf{n}\cdot\boldsymbol{\nabla}\times\mathbf{n})^2}_{\text{twist}} + \underbrace{\frac{1}{2}k_{33}(\mathbf{n}\times\boldsymbol{\nabla}\times\mathbf{n})^2}_{\text{bend}} - \underbrace{\frac{1}{2}(k_{22}+k_{24})\boldsymbol{\nabla}\cdot(\mathbf{n}(\boldsymbol{\nabla}\cdot\mathbf{n})+\mathbf{n}\times\boldsymbol{\nabla}\times\mathbf{n}))}_{\text{saddle-splay}} \quad (3.1)$$

where k_{11}, k_{22}, k_{33} and k_{24} are elastic moduli corresponding to splay, twist, bend and saddle-splay (although note that saddle-splay is also dependent on k_{22}). These constants represent the degree to which their respective deformations are penalized (i.e. resistance to their respective deformation mode), which can vary depending on the type of liquid crystal being modelled.

Experimental measurements of the individual elastic constants can be obtained by imposing conditions on a sample of NLC such that the resulting texture involves only a single isolated deformation mode. It is common to experimentally determine these elastic constants by taking advantage of the Freedericksz transition, in which reorientation of

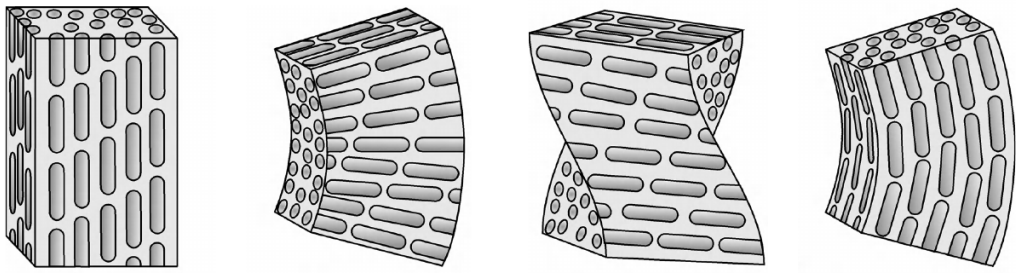

(a) Equilibrium (b) Splay, k_{11} (c) Twist, k_{22} (d) Bend, k_{33}

Figure 3.1: The three major modes of elastic deformation. From ref. [85].

the deformed domain to a uniform one occurs above a critical external field value. The experimentally-observed critical field value is then related to the elastic constant via the Frank-Oseen model [75]. From these measurements, it is known that the elastic constants are temperature-dependent, decreasing rapidly with increasing temperature. However, their *ratio* with respect to each other can be considered independent of temperature [81].

On the premises that (i) the free energy density f should be non-negative and (ii) when $\boldsymbol{\nabla}\mathbf{n} = 0$, f should be minimized, one can further derive a set of inequalities which govern the permissible values of the elastic constants. These are called the Ericksen inequalities [86], and can be summarized as the following:

$$k_{11} \geq 0, \quad k_{22} \geq 0, \quad k_{33} \geq 0 \tag{3.2}$$

$$-k_{22} \leq k_{24} \leq \min(2k_{11} - k_{22}, k_{22}) \tag{3.3}$$

These inequalities are an important theoretical consideration when modelling liquid crystals using experimental estimates of the elastic constants.

By minimizing the total free energy $F = \int_V f_f \, dV$ with respect to $\mathbf{n}$, Frank-Oseen theory can be used to study the behaviour of various nematic systems both analytically and using numerical approaches [43]. Overall, while Frank-Oseen theory is relatively simple, it does have some key shortcomings which limit its usefulness to certain idealized NLC systems [87]:

1. The director is unable to represent changes in the degree of orientational order, i.e. the model assumes orientational order is constant within the domain.

2. Since the director is a vector, it is only capable of describing uniaxial ordering.

Since defects correspond to regions where the director is undefined and orientational order vanishes, this theory is limited to defect-free domains [88]. While early studies have used the Frank-Oseen model in cases with disclinations, its usage can result in inaccurate predictions [27]. The requirement for the orientational order to be constant also means that the model cannot describe phase transition between isotropic and nematic states. Therefore confined domains such as NLC droplets are inadequately described by this model. As a result, another approach is needed.

3.2 Landau–de Gennes Theory

3.2.1 Tensor Order Parameter

The phenomenological Landau–de Gennes theory is another continuum theory which models the first-order nematic-isotropic phase transition observed in NLCs [81]. It was derived by Pierre-Gilles de Gennes, and is an extension of Lev Landau's dynamic theory of second-order phase transitions. The theory begins by defining a symmetric traceless second-rank tensor order parameter $\mathbf{Q}$ called the *alignment tensor* which represents both orientational order and direction [81]:

$$\mathbf{Q} = S(\mathbf{nn} - \frac{1}{3}\boldsymbol{\delta}) + P(\mathbf{mm} - \mathbf{ll}) \tag{3.4}$$

where $\boldsymbol{n}$ is the nematic director, S quantifies the degree of uniaxial alignment, and P quantifies the degree of biaxial alignment associated with the two minor eigenvectors $\boldsymbol{m}$ and $\boldsymbol{l}$. $\boldsymbol{\delta}$ is the identity tensor. In this case, the major eigenvector of $\mathbf{Q}$ is equivalent to the director $\mathbf{n}$. In this way, various degrees of ordering can be described, unlike in Frank-Oseen theory, in which S is assumed uniform.

As shown in Chapter 2, these order parameters characterize a *uniaxial* orientational distribution function of a local region of mesogens by a second-order Legendre polynomial [81]. We can formalize this "localized region" by defining a length scale λ_n called the nematic coherence length, which gives a characteristic length scale over which variations in S decay above the phase transition temperature T_{ni} (i.e. the macroscopic cut-off for using this continuum model) [81]. Figure 3.2 visualizes the permissible values of S, which can range between $S = -0.5$ and $S = 1$. However, it should be noted that $S < 0$, while theoretically plausible, is generally considered non-physical. This non-physicality in the order parameter is addressed by the free energy, in which $S < 0$ is not permitted as a solution (as shown later).

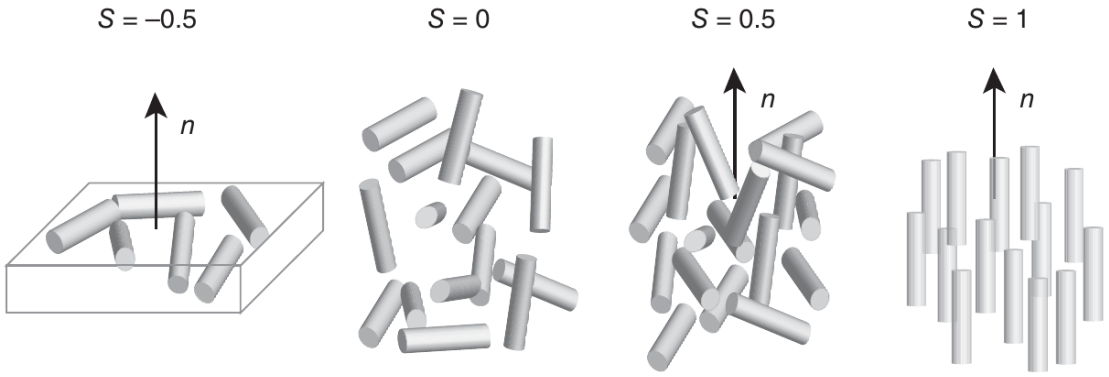

Figure 3.2: Possible values of uniaxial nematic order parameter S. From ref. [10].

Nonzero P means that the orientational distribution is favoured in one of the two axes orthogonal to n (thus giving the orientational distribution function a biaxial nature). Thus $S = 0$ and $P = 0$ correspond to the isotropic (liquid) case, where ordering in all directions is equally favoured. $0 < S < 1$ and $P = 0$ correspond to the uniaxial nematic phase, and biaxial orientational ordering occurs when both S and P are non-zero. Different configurations of S and P are visualized in Figure 3.3. More needle-like shapes represent higher uniaxial order, while shapes which have non-uniform cross-section (e.g. flatter) represent biaxial order.

3.2.2 Free Energy Density

We now define an energy density as a function of $\mathbf{Q}$. In addition to describing the bulk elastic energy density, this model also includes terms associated with the nematic-isotropic phase transition which models the system's orientational order as a function of temperature. These terms represent a Landau expansion of the order parameter in the vicinity of the transition (written here in index notation) [81]:

$$f_b = f_i + \frac{1}{2}a_0(T - T^*_{ni})(Q_{ij}Q_{ji}) - \frac{1}{3}b(Q_{ij}Q_{jk})Q_{ki} + \frac{1}{4}c(Q_{ij}Q_{ji})^2 \tag{3.5}$$

Here, a_0, b and c are temperature-independent constants which characterize the phase transition of the LC material, T is the temperature of the system, and T^*_{ni} is the so-called supercooling temperature, the limit of metastability of the isotropic phase (slightly below the experimental T_{ni}). f_i is the free energy contribution from the isotropic phase.

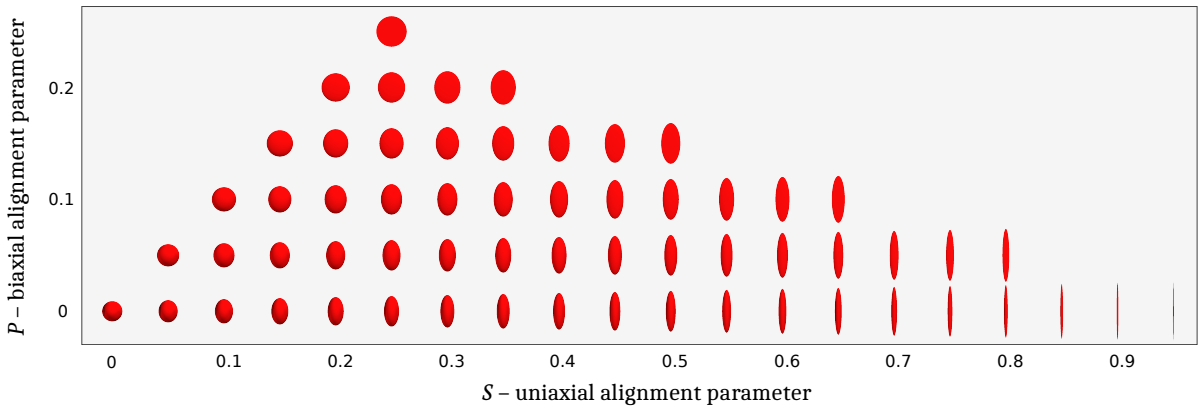

Figure 3.3: Visualization of $\mathbf{Q}$ as a function of S and P with the director referenced to point upwards. The relative lengths of the ellipsoid axes describe the orientational distribution (e.g. $S = 0$ and $P = 0$ correspond to isotropic liquid).

While minimization of Equation 3.5 with respect to $\mathbf{Q}$ is non-trivial, the equation can be simplified such that an equilibrium value for S can be determined. This is useful in order to have an idea about the expected orientational order at a given temperature. If a uniaxial domain is assumed, then the uniaxial form of $\mathbf{Q}$ (i.e., with $P = 0$) can be substituted into Equation 3.5, arriving at a free energy density in terms of S only (see ref. [89]):

$$f_b(S) = f_i + \frac{1}{3}a_0(T - T^*_{ni})S^2 - \frac{2}{27}bS^3 + \frac{1}{9}cS^4 \tag{3.6}$$

Minimizing this equation using standard optimization (solving $\frac{\mathrm{d}f_b}{\mathrm{d}S} = 0$) results in the following physical equilibrium solutions S_{eq} [89]:

$$S_{eq} = \begin{cases} 0 & \text{isotropic phase stable} \\ \frac{b}{4c}[1 + \sqrt{1 - 24(a_0c(T - T^*_{ni})/b^2)}] & \text{nematic phase stable} \end{cases}$$

The bulk energy represents the energy associated with the thermodynamics of the system (temperature). It is a Landau power series expansion taken to fourth order in the scalar invariants of $\mathbf{Q}$ [81]. This is the simplest form of the bulk energy density which allows for multiple local minima and produces a first-order nematic-isotropic phase transition [90]. This model is valid for T close to the nematic-isotropic transition temperature [81], requiring $T < T_{ni}$ for nematic phase formation.

In addition to the free energy associated with the phase transition, there is also a free energy associated with the elasticity, which is derived similarly to Frank-Oseen elasticity, except expanding gradients in $\mathbf{Q}$ (note $\partial_i Q_{jk} \equiv \frac{\partial Q_{jk}}{\partial x_i}$ in the notation below) [80]:

$$f_{el} = \frac{1}{2}L_1 \left(\partial_i Q_{jk} \partial_i Q_{kj}\right) + \frac{1}{2}L_2 \left(\partial_i Q_{ij} \partial_k Q_{kj}\right) + \frac{1}{2}L_3 \left(\partial_k Q_{ij} \partial_j Q_{ik}\right) + \frac{1}{2}L_{24} (\partial_k Q_{ij} \partial_j Q_{ik}) \quad (3.7)$$

where L_1, L_2, L_3, and L_{24} are elastic constants. This approach uses the minimal set of elastic terms that are necessary to independently capture the different modes of deformation modelled by the Frank-Oseen elastic energy density (Equation 3.1) [84].

Similarly to f_f in Frank-Oseen theory, which penalizes gradients in $\mathbf{n}$, the elastic energy density f_{el} penalizes gradients in $\mathbf{Q}$. However, unlike Frank-Oseen theory, the different modes of deformation are not embedded within the individual coefficients L_i, which have no physical connotation. However, it is possible to evaluate these terms with respect to the Frank-Oseen elastic constants k_i under the assumption of uniaxial $\mathbf{Q}$ and uniform S, which are necessary in order to properly relate the two theories [84]:

$$L_1 = \frac{1}{6S^2}(k_{33} - k_{11} + 3k_{22}) \quad (3.8)$$

$$L_2 = \frac{1}{S^2}(k_{11} - k_{22} - k_{24}) \quad (3.9)$$

$$L_3 = \frac{1}{2S^3}(k_{33} - k_{11}) \quad (3.10)$$

$$L_{24} = \frac{1}{S^2}k_{24} \quad (3.11)$$

Such relations are used to arrive at realistic constants for the coefficients L_i from experimental measurements of k_i under the assumption $S = S_{eq}$. It is common to utilize the single elastic constant approximation and set L_1 to be the only nonzero term in Equation 3.7. In terms of the Frank-Oseen elastic constants, this results in $k_{11} = k_{22} = k_{33}$ and $k_{24} = 0$ or equal elastic moduli for splay, bend, twist, and saddle-splay.

In order to model external field-switching, an electric energy density is introduced, representing the change in energy when an electric field is applied:

$$f_e = -\frac{\epsilon_0}{8\pi}\left[\left(\frac{\epsilon_\parallel + 2\epsilon_\perp}{3}\delta_{ij} + (\epsilon_\parallel - \epsilon_\perp)Q_{ij}\right)\right] E_j E_i \quad (3.12)$$

where $\mathbf{E}$ is the electric field vector, ϵ_0 is the permittivity of free space, and $\varepsilon_\parallel$ and $\varepsilon_\perp$ are the dielectric constants parallel and perpendicular to the director $\mathbf{n}$, respectively. The anisotropy in the permittivity values ($\Delta\epsilon = \epsilon_\parallel - \epsilon_\perp$), dictates whether the electric field tends to orient molecules along its direction (positive anisotropy) or away from its direction (negative anisotropy) [1].

3.3 Surface Anchoring

For confined liquid crystal domains (e.g. in PDLC devices), the anchoring of the liquid crystal at the polymer-liquid crystal interface must also be accounted for. The impact of surfaces is modeled using a phenomenological approach in which the effect of the surface adds a contribution to the alignment (instead of trying to directly model the surface as another material).

Many early studies employ *fixed* or *strong* anchoring, in which the director at the surface is fixed throughout the simulation to be either homeotropic or planar using a Dirichlet boundary condition. This assumption is only good for large domains where the bulk texture is sufficiently isolated from the surface [91], which is not applicable to the study of droplets. Instead, *weak* anchoring, which is more generalizable [92], uses a finite anchoring strength to dictate the behaviour of the NLC at the boundary. Several surface free energy density models of weak anchoring exist: the three most common ones in the literature which are compatible with the LdG model are presented here. The simplest and most common approach, called Rapini-Papoular theory [93], imposes a penalty to the free energy. It was originally described with respect to the Frank-Oseen model, but can be easily adapted to the alignment tensor as [94]:

$$f_{rp} = \frac{1}{2}\alpha(Q_{ij} - Q_{ij}^{(0)})^2 \tag{3.13}$$

where α is the strength associated with the anchoring (in the limit as α approaches infinity, the anchoring becomes strong) and $Q_{ij}^{(0)}$ is the assumed equilibrium alignment tensor at the boundary (essentially Equation 3.4 where $S = S_0$ and $\mathbf{n} = \mathbf{k}$ where $\mathbf{k}$ is the direction of the anchoring, i.e. normal to the surface in the case of homeotropic anchoring).

The Rapini-Papoular model is only capable of describing homeotropic and "directional" (non-degenerate) planar anchoring, since it relies on defining the easy axis in a specific direction. Degenerate planar anchoring is instead implemented using a similar-looking model by Fournier and Galatola [17].

$$f_{fg} = \alpha_1(\tilde{Q}_{ij} - \tilde{Q}_{ij}^{\perp})^2 + \alpha_2(\tilde{Q}_{ij}\tilde{Q}_{ij} - S_0^2)^2 \tag{3.14}$$

where $\tilde{Q}_{ij} = Q_{ij} + 1/3 S_0 \delta_{ij}$ and $\tilde{Q}_{ij}^{\perp} = P_{ik}\tilde{Q}_{kl}P_{lj}$ where $P_{ij} = \delta_{ij} - k_i k_j$. Again, S_0 defines an equilibrium orientational order at the surface. This surface potential is fourth order in $\mathbf{Q}$, which is necessary to possess a minimum for degenerate planar anchoring [17].

The most generalized anchoring model for describing anchoring on isotropic substrates is based on a power series expansion of $\mathbf{Q}$ at the surface [95, 96]:

$$f_s = \alpha_{11} k_i Q_{ij} k_j + \alpha_{21} Q_{ij} Q_{ij} + \alpha_{22}(k_i Q_{ij} k_j)^2 + \alpha_{23} k_i Q_{ij} Q_{jk} k_k \tag{3.15}$$

This model is often truncated to the first (most significant) term to reduce its computational complexity. An advantage of this model over the previous models is that this does not require the specification of the degree of alignment at the surface S_0, which is difficult to measure (although has been done [97]). Often, simulation studies will make the assumption $S_0 = S_{eq}$. To avoid introducing another parameter into the system, the surface anchoring model used in this work, unless otherwise noted, is:

$$f_s = -\alpha k_i Q_{ij} k_j \tag{3.16}$$

where a negative sign is introduced so that the expression favours homeotropic anchoring conditions. The disadvantage of this model compared to Equations 3.13 and 3.14 is that $\mathbf{Q}$ is not inherently bounded (there is no minimum). However, this does not present a major problem since the *total* free energy F will still have a minimum due to competition of the surface anchoring energy with the energy contributions from the volume.

3.4 Numerical Methods

Given the energy contributions from the previous sections, the total free energy can be written now as an integral of the free energy density (including from the surface A) over the domain volume V:

$$F = \int_V (\underbrace{f_b + f_{el} + f_e}_{f})\, dV + \int_A f_s\, dA \tag{3.17}$$

The dynamics of a nematic liquid crystal system can then be simulated by minimizing F, which is a functional, using the calculus of variations. The full process for this is given in Appendix A. This results in a partial differential equation (PDE) called the Euler–Lagrange equation:

$$\frac{\partial f}{\partial \mathbf{Q}} - \boldsymbol{\nabla} \cdot \left(\frac{\partial f}{\partial \boldsymbol{\nabla} \mathbf{Q}} \right) = 0 \tag{3.18}$$

which is associated with the following boundary condition:

$$\frac{\partial f_s}{\partial \mathbf{Q}} + \mathbf{k} \cdot \left(\frac{\partial f}{\partial \boldsymbol{\nabla} \mathbf{Q}} \right) = 0 \tag{3.19}$$

where $\mathbf{k}$ is the unit surface normal vector. Solving the steady-state Equation 3.18 numerically is difficult to do directly: convergence is only likely if the initial guess for the system is

close enough to the equilibrium configuration [98]. Therefore, it is customary to introduce a time derivative into the model, which also allows us to probe the physical evolution of the system [99]. This scheme is commonly called the *time-dependent Ginzburg-Landau equation* or *Model A dynamics* and is the most basic model for representing the dissipation of a nonconserved order parameter in time [99]:

$$\mu_r \frac{\partial \mathbf{Q}}{\partial t} = -\left[\frac{\partial f}{\partial \mathbf{Q}} - \boldsymbol{\nabla} \cdot \left(\frac{\partial f}{\partial \boldsymbol{\nabla}\mathbf{Q}}\right)\right]^{ST} \tag{3.20}$$

where μ_r is the rotational viscosity of the nematic phase (assumed to be the same for all components of $\mathbf{Q}$), and $[\,]^{ST}$ refers to taking the symmetric-traceless component of the expression (necessary in order to make sure $\mathbf{Q}$ remains invariant when stepping in time). Alternatively, it is possible to also project $\mathbf{Q}$ onto a symmetric-traceless tensor basis (e.g. see refs. [27, 100, 101]), which similarly maintains symmetry and tracelessness.

The resulting system of PDEs representing a boundary value problem which can be solved using several different approaches. In the literature, the most commonly used methods are the finite difference method and the finite element method. For the objectives in this work, the finite element method is more suited: unlike the finite difference method, in which the domain must be discretized uniformly in space in a regular lattice, the finite element method, which is capable of using arbitrarily-sized elements, is better able to capture the curvature at the boundary associated with droplet-like geometries.

The finite element method (FEM) involves first discretizing the domain into a mesh of finite elements connected by nodes: in this work, triangular elements (in two dimensions) and tetrahedral elements (in three dimensions) are used, as shown in Figure 3.4. The approximate solution is represented by a linear combination of parameters and basis functions which are mapped onto the elements of this mesh. Depending on the chosen basis functions, the solution resulting from FEM can differ in its accuracy. First-order (linear) Lagrange polynomials are used in this work.

Using the method of weighted residuals, the system of PDEs (Equation 3.20) is reformulated as a weighted integral statement (called "weak" form). This yields the following

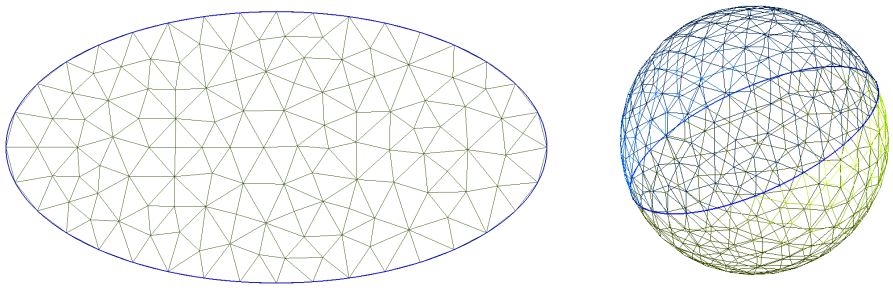

Figure 3.4: Examples of two and three-dimensional meshes used in finite element method.

integral equation (see Appendix B for full derivation):

$$
\begin{aligned}
0 = \iiint_V \mu_r \frac{\partial Q_{ij}}{\partial t} v_{ji}\, dV + \iiint_V \Bigg[\Bigg(& a_0(T - T^*_{ni})(Q_{ij}) - b(Q_{ik}Q_{kj} - \frac{1}{3}Q_{kl}Q_{lk}\delta_{ij}) \\
& + c(Q_{kl}Q_{lk}Q_{ij}) - \frac{\varepsilon_0}{8\pi}(\varepsilon_\parallel - \varepsilon_\perp)(E_iE_j - \frac{1}{3}E_kE_k\delta_{ij}) \Bigg) v_{ji} + L_1(\partial_k Q_{ij}\partial_k v_{ji}) \\
& + (L_2 + L_{24}) \left(\frac{1}{2}(\partial_i Q_{kj}\partial_k v_{ji} + \partial_j Q_{ki}\partial_k v_{ji}) - \frac{1}{3}\partial_l Q_{lk}\partial_k v_{ji}\delta_{ij} \right) \\
& + L_3 \left(Q_{kl}\partial_l Q_{ij}\partial_k v_{ji} + \frac{1}{2}\partial_i Q_{kl}\partial_j Q_{kl} v_{ji} - \frac{1}{6}\partial_k Q_{lm}\partial_k Q_{lm}\delta_{ij} v_{ji} \right) \Bigg] \, dV \\
& + \oiint_A \alpha k_i k_j v_{ji}\, dA
\end{aligned}
\tag{3.21}
$$

where $\mathbf{v}$ is the weighting function. In the Galerkin finite element method, the weighting functions are the same as the basis functions. The approximate solution is then substituted into this formulation and rearranged into a system of nonlinear equations. These equations are simultaneously solved over the mesh using Newton's method to arrive at the approximate solution which minimizes the residual.

In practice, an extra step is taken where Equation 3.21 is nondimensionalized, meaning that the magnitude of each (dimensional) variable is scaled to a nondimensional value between 0 and 1. This step is documented in Appendix B and allows for the solution to scale (to a certain extent). It also reduces round-off error in the numerical calculations.

In addition to discretizing space, the time domain must also be discretized. The discretization of time is performed independently of the finite element method using the method of lines approach. Essentially, the time derivative is discretized by following the

approach of the trapezoidal method (related, but not to be confused with the trapezoidal method for approximating integrals) [102]. Rewriting Equation 3.20 as $\frac{\partial \mathbf{Q}}{\partial t} = g(\mathbf{Q}, t)$, then the method states:

$$\mathbf{Q}_{t+\Delta t} = \mathbf{Q}_t + \frac{\Delta t}{2} \left(g(\mathbf{Q}_{t+\Delta t}, t + \Delta t) + g(\mathbf{Q}_t, t) \right) \tag{3.22}$$

where Δt is the time step and the solution $\mathbf{Q}_{t+\Delta t}$ at the new time is solved for using the known solution $\mathbf{Q}_t$ at the current time. The time evolution begins from an assumed initial condition until the system reaches an equilibrium state.

An adaptive time stepping method is also implemented based on Richardson extrapolation, allowing the time step Δt to fluctuate depending on the local error for each step [102]. For each new time, the local error is computed by solving for $\mathbf{Q}_{t+\Delta t}$ *twice*: the first solution $\mathbf{Q}^{(1)}_{t+\Delta t}$ is found using a single solve with a step size Δt, and the second (more accurate) solution $\mathbf{Q}^{(2)}_{t+\Delta t}$ is found using two consecutive solves with halved steps $\Delta t/2$. The local error is then computed as $l = \left\| \mathbf{Q}^{(2)}_{t+\Delta t} - \mathbf{Q}^{(1)}_{t+\Delta t} \right\|$. If l is above a fixed tolerance for any given time step, then the time step is decreased proportionally and the solution is recomputed: this proceeds until l is below the desired tolerance. While this is a computationally intensive process, it allows for much larger time steps to be taken and ensures that the local error is stable.

The numerical methods described above are implemented and solved in the Python programming language using the open-source numerical package FEniCS [103], which provides a framework for solving partial differential equations using the finite element method on high-performance computing systems. For discretizing the desired geometries, the software package gmsh is used.

3.5 Visualization

Visualization of solution data resulting from the LdG approach is nontrivial due to the additional degrees of freedom encoded in a tensor representation. Unlike visualization of a vector or scalar field, tensor-based visualization methods are rarely used or discussed, even as the LdG method has become more widely-used. Approaches to visualization of nematic alignment tensor fields have typically resorted to simplifications such as extracting the major eigenvector (director $\mathbf{n}$) of the tensor and visualizing it as a vector field [104–106]. While these approximations enable visualization using standard approaches (streamlines or quiver plots), they are unable to reflect the degree of ordering S or the biaxiality P.

The majority of tensor visualization approaches have been invented for the field of magnetic resonance imaging, where tensor fields can arise in diffusion-based imaging [107]. The simplest tensor imaging method is using *tensor glyphs*. This approach is similar to a quiver plot, but instead of plotting small arrow-like glyphs, a three-dimensional shape such as a rectangular prism or ellipsoid is used [107]. Variations in the dimensions of these shapes (which are based on the eigenvalues and eigenvectors of a tensor) are used to reflect changes in the tensor field: this approach can be seen in Figure 3.3.

In ref. [108], we present a rationale for a less common higher-order visualization approach called a *hyperstreamline* [109], which can be used to visualize symmetric tensor fields such as the alignment tensor. Analogous to ordinary streamline visualization of vector fields, hyperstreamlines are enhanced such that, in addition to direction, they have volume, as depicted in Figure 3.5. This enables them to visualize not only the general orientation of the director $\mathbf{n}$, but also the biaxiality. The colour of the hyperstreamline is used to indicate the uniaxial order parameter S.

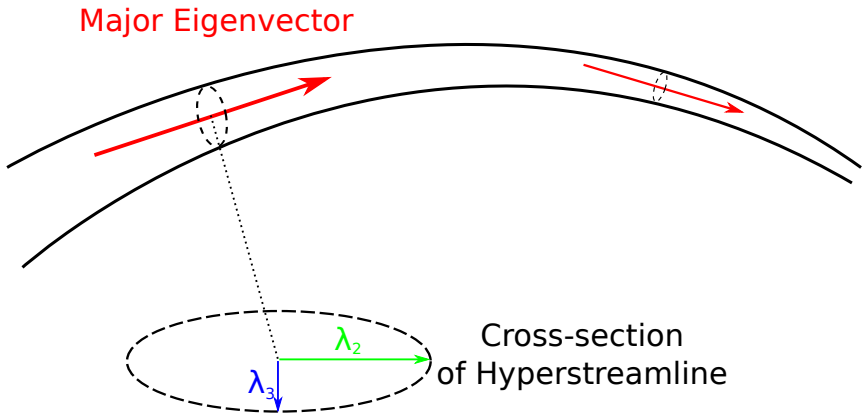

Figure 3.5: Schematic of a hyperstreamline demonstrating its direction and cross-section. From ref. [108].

Unlike tensor glyphs, hyperstreamlines are less susceptible to visibility issues such as overlapping, due to their continuous tube-like shape. As a result, hyperstreamlines are widely used throughout this thesis for the purposes of visualizing results.

Chapter 4

Field-driven Dynamics of Nematic Microcapillaries[1]

4.1 Overview

As an initial study of the complex formation and electric field-driven switching dynamics of PDLC domains, simulations of nematic liquid crystal in simplified two-dimensional elliptic cylinder (microcapillary) geometries of these domains were performed. Using these approximations, the effects of geometry (aspect ratio), surface anchoring, and external field strength were studied through the use of the Landau–de Gennes model.

While this geometry is a poor approximation of the spherical and ellipsoidal domains actually observed in PDLCs [6], it has direct relevance to other applications, including the study of nematic-filled capillaries which are of interest for fibre optics-based devices [110]. Furthermore, even though two-dimensional elliptic domains are not topologically equivalent to three-dimensional ellipsoidal domains, this "coarse" geometric simplification has been used in previous studies [15]. The results described here also act as a starting point for understanding more complex simulations.

The specific objectives of this work were to study the effects of the geometry of these domains (specifically aspect ratio) on the following:

[1]This chapter is derived from work originally published in: P. Khayyatzadeh, F. Fu, and N. M. Abukhdeir. *Physical Review E* 92(6):062509, 2015.

- the formation dynamics and equilibrium textures of nematic elliptic cylinder domains. This is similar to the state of the PDLC after quenching the phase-separated film.
- the external field-driven dynamics of nematic elliptic cylinder domains. This is similar to the state of the PDLC after application of an electric field to induce the transparent state.
- the relaxation or "restoration" dynamics of nematic elliptic cylinder domains following release of the external field. This is similar to state of the PDLC after release of the electric field to return to the translucent state.

4.2 Methodology

The theoretical model is based upon the Landau–de Gennes theory for the nematic phase, which was discussed in Section 3.2. This model uses the alignment tensor $\mathbf{Q}$ which enables simulation of phase transition and disclinations, and it also contains the electric free energy contribution which simulates electric field switching.

For the elasticity part of the model (Equation 3.7), the single elastic constant approximation was employed [74], in which only L_1 is set to be nonzero and the L_2, L_3 and L_{24} terms in the model vanish, leading to the following elastic free energy density:

$$f_{el} = \frac{1}{2} L_1 \left(\partial_i Q_{jk} \partial_i Q_{kj} \right) \tag{4.1}$$

This simplifies the analytical work necessary to minimize the total free energy and reduces the number of parameters in the model.

As noted in Section 3.3, homeotropic anchoring is assumed and modelled using an expansion for the surface free energy retaining only terms up to first order:

$$f_s = -\alpha k_i Q_{ij} k_j \tag{4.2}$$

Note that the governing equations for the model were nondimensionalized and time is reported as a dimensionless quantity $\tilde{t}$:

$$\tilde{t} = \frac{t}{\tau} \quad , \quad \tau = \frac{\mu_r}{a_0 T^*_{ni}} \tag{4.3}$$

However, to simplify notation, dimensionless quantities should be assumed in cases where units are not given (which is the case for all time labels in this chapter).

Table 4.1: Simulation parameters. Material-based parameters were based on estimates of pentyl-cyanobiphenyl.

Parameter	Value	Units	Ref.
T^*_{ni}	307.2	K	111
a_0	1.4×10^5	$\mathrm{J\,m^{-3}\,K^{-1}}$	111
b	1.8×10^6	$\mathrm{J/m^3}$	112
c	3.6×10^6	$\mathrm{J/m^3}$	112
L_1	3.0×10^{-12}	J/m	112
$\epsilon_\parallel$	17	(relative)	112
$\epsilon_\perp$	7	(relative)	112
μ_r	0.055	$\mathrm{kg\,m^{-1}\,s^{-1}}$	113
α	5×10^{-5}	$\mathrm{J/m^2}$	35

In the model, material parameters were chosen which approximately correspond to 5CB [111, 112] and the anchoring strength was based on estimates for polymer surfaces (on the order of 10^{-5}–$10^{-4}\,\mathrm{J/m^2}$) [35]. These simulation parameters are shown in Table 4.1.

Characteristic length scales of the free energy were also analyzed in order to determine simulation parameters. For a nematic, the most fundamental length scale is the nematic coherence length, which is estimated through the competition between bulk thermodynamic and elastic contributions to the LdG free energy [81]:

$$\lambda_n = \sqrt{\left| \frac{L_1}{a_0 \left(T - T^*_{ni}\right)} \right|} \tag{4.4}$$

This length scale approximates the thickness of the nematic/isotropic interface and is typically $\lambda_n \approx 4\,\mathrm{nm}$. Therefore the nematic domain size was chosen to be on the order of $1\,\mu\mathrm{m}$, much larger than λ_n. Instead of simulating fully three-dimensional elliptic capillary domains, two-dimensional ellipses were used with textures being assumed to be homogenous in the third dimension (along the axis of the cylinder), which is a commonly used approach [27,114,115] that is justified in most cases [98]. These geometries were categorized according to their aspect ratio $R = \frac{r_a}{r_b}$ where r_a is the length of the semi-major ellipse axis and r_b is the length of the semi-minor ellipse axis. Based on a circular reference domain with diameter of $1\,\mu\mathrm{m}$, all simulation geometries were also constrained to a constant area of $0.8\,\mu\mathrm{m}^2$, i.e. $\pi r_a r_b = 0.8\,\mu\mathrm{m}^2$. The µm-scale for LC domains is relevant to PDLCs used for privacy glass and other scattering applications [35].

Two types of simulations were performed: formation dynamics and field-switching dynamics. Formation dynamics simulations correspond to cooling of the PDLC domains from isotropic to nematic in the absence of an electric field. This models a thermal quenching method which can be used to manufacture PDLC films [35]. Heterogeneous nucleation of the nematic phase (nucleation from a nematic domain boundary) was assumed to be the dominant nucleation mechanism based on experimental observations [116]. Therefore the initial conditions for all simulations assumed a uniaxial boundary layer well-aligned with the surface normal $\mathbf{k}$, coinciding with homeotropic surface anchoring. Based on a polar coordinate system (r, θ) along the surface, a linear decay was used for the uniaxial nematic order parameter S:

$$S_{init}(r,\theta) = S_{eq}\left(\frac{r - r_s(\theta) + \lambda_n}{\lambda_n}\right) \qquad \text{for} \qquad r_s(\theta) - \lambda_n < r < r_s(\theta) \tag{4.5}$$

$$S = 0 \qquad \text{for} \qquad 0 \leq r \leq r_s(\theta) - \lambda_n \tag{4.6}$$

where λ_n is the nematic coherence length (Equation 4.4), and $r_s(\theta)$ is the radial coordinate of the ellipse surface. The expression for $r_s(\theta)$ is:

$$r_s(\theta) = \frac{r_a r_b}{\sqrt{r_b^2 \cos^2\theta + r_a^2 \sin^2\theta}} \tag{4.7}$$

The nematic director field $\mathbf{n}$ is assumed to be well-aligned with the ellipse surface normal, which can be approximated by:

$$\mathbf{n}_{init} = \frac{r_a \cos(\theta)\mathbf{e}_1 + r_b \sin(\theta)\mathbf{e}_2}{\sqrt{r_a^2 \cos^2\theta + r_b^2 \sin^2\theta}} \tag{4.8}$$

resulting in the initial alignment tensor field:

$$\mathbf{Q}_{init} = S_{init}\left(\mathbf{n}_{init}\mathbf{n}_{init} - \frac{1}{3}\boldsymbol{\delta}\right) \tag{4.9}$$

This initial condition represents the expected (mostly isotropic) texture above T_{ni}. By setting the actual simulation temperature to $T = 307\,\mathrm{K}$, the thermal quench described above is modelled.

Switching dynamics simulations correspond to application of an electric field to a fully-formed nematic domain and observing the resulting reorientation. The fully-formed nematic domains from the formation simulations were used as initial conditions with the electric field $\mathbf{E}$ oriented along the major axis of the ellipse. To assess an appropriate range of

field strengths, another characteristic length which quantifies the competition between the electric field and the nematic elastic forces was computed:

$$\lambda_e = \sqrt{\frac{L_1}{\epsilon_0(\epsilon_\parallel - \epsilon_\perp)E^2}} \tag{4.10}$$

which is the *dielectric coherence length* [117]. For the range of electric field strengths $E \in [0\,\mathrm{V\,\mu m^{-1}}, 5\,\mathrm{V\,\mu m^{-1}}]$, which are typical field strengths for PDLC devices [118], $\lambda_e \approx 10\,\mathrm{nm}$. This corresponds to a moderately strong electric field, but not to the extent that it could induce melting of the nematic phase.

A similar characteristic length can be determined for the competition between surface anchoring and elastic forces:

$$\lambda_s = \frac{L_1}{\alpha} \tag{4.11}$$

which is the *surface extrapolation length* [117]. As $\lambda_s \to 0$ the surface anchoring effects dominate and the nematic alignment at the boundary governs the bulk texture; this is so-called "strong" anchoring. As $\lambda_s \to \infty$ the bulk nematic elasticity effects dominate and the nematic alignment at the surface is governed by the bulk texture. The surface anchoring strength of $\alpha = 5 \times 10^{-5}\,\mathrm{J/m^2}$ results in $\lambda_s \approx 100\,\mathrm{nm}$ which corresponds to "weak" surface anchoring.

4.3 Nematic Domain Formation and Equilibrium Texture

Figure 4.1 shows visualizations of the alignment tensor field for nematic elliptic cylinder domains with aspect ratios $R = \{1.05, 1.6, 2\}$. A sequence of three distinct growth regimes was observed: free growth, interface impingement/defect formation, and bulk relaxation. The *free growth regime* involves the stable nematic phase growing into the unstable isotropic phase such that the texture is approximately commensurate with the anchoring conditions. The *interface impingement/defect formation regime* follows, where the nematic/isotropic interface impinges on itself resulting in the simultaneous formation of a pair of orientational defects along the major axis. For all simulations, the type of orientational defects, or disclinations, observed were wedge-type with strength $+\frac{1}{2}$ [119]. These disclinations are formed in order to resolve the topological constraints imposed by the confinement geometry and anchoring conditions. Finally, the *bulk relaxation regime* follows impingement where

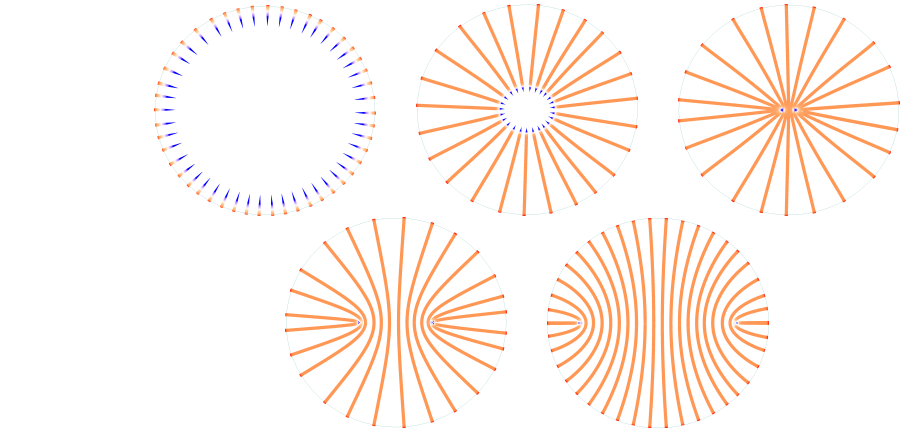

(a) $R = 1.05$, $t = \{50,\ 1.82 \times 10^4,\ 2.43 \times 10^4,\ 4.63 \times 10^5,\ 6.40 \times 10^6\}$

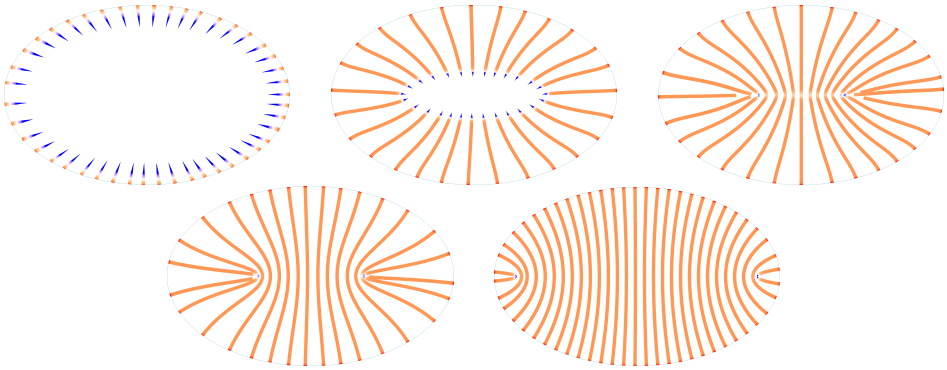

(b) $R = 1.6$, $t = \{50,\ 1.35 \times 10^4,\ 1.93 \times 10^4,\ 4.02 \times 10^5,\ 4.56 \times 10^6\}$

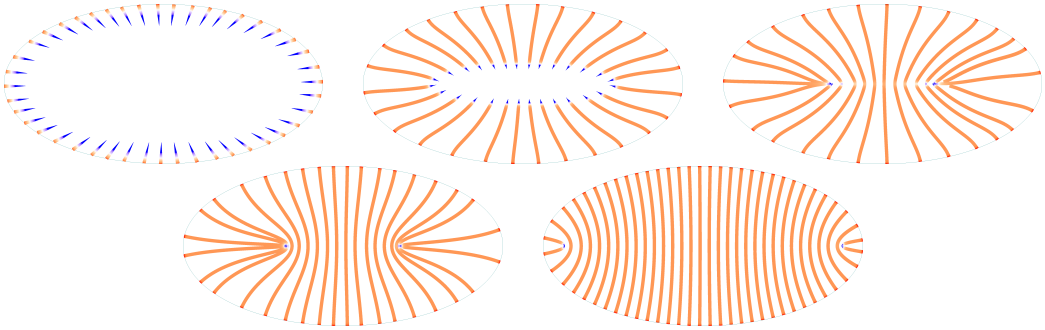

(c) $R = 2$, $t = \{50,\ 1.19 \times 10^4,\ 1.71 \times 10^4,\ 3.09 \times 10^5,\ 3.35 \times 10^6\}$

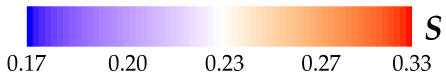

Figure 4.1: Hyperstreamline visualizations of the alignment fields during the formation process for different aspect ratios. Times are labelled going from top-to-bottom and left-to-right.

the fully formed nematic texture relaxes to its equilibrium state through simultaneous disclination motion towards the ellipse focal regions and bulk reorientation.

The growth and formation mechanism for the $R \approx 1$ case has been studied in past work for two-dimensional domains [27, 115, 120, 121]. Rey and Sharma developed a texture phase diagram using the Landau–de Gennes model for the circular geometry [121]. They predict the splitting of a +1 disclination into a pair of $+\frac{1}{2}$ disclinations located at the centre of the domain for domain sizes on the order of λ_n. Given that the simulated domains are micron-scale, the defect splitting observed in the $R \approx 1$ case is in agreement with these past results. The resulting domain texture is uniformly oriented in a region parallel to an axis and with the pair of disclinations located along the axis orthogonal to it. Additionally, simulation results are found to also be consistent with past work [115] predicting a transition from textures with disclinations to an "escape" texture, absent of defects, under certain conditions (anchoring strength, domain size, etc). The growth and formation mechanism for the elliptic case $R > 1$ is observed to be significantly different and does not exhibit disclination splitting, even though the topologies of the elliptic and circular domains are equivalent.

The underlying formation mechanism for elliptic domains is well-explained by the approximation of Wincure and Rey [76] of the velocity of a uniaxial isotropic/nematic interface. They have shown that its velocity v is proportional to the difference in energy between the nematic and isotropic phases ΔF and capillary force $\mathcal{C}$ [76]:

$$\beta v = \mathcal{C} - \Delta F \tag{4.12}$$

where β is an effective viscosity term. During the free growth regime, in every case (Figure 4.1), as the isotropic/nematic interface approaches the center of the domain, the capillary force grows inversely proportional to the radius of the central isotropic region. For a circular domain, $v(\theta)$ is essentially constant but for the elliptic domain it varies from a maximum at the interface regions closest to the minor axis (high curvature) to a minimum at those regions closest to the major axis (low curvature).

As the radius of curvature of the interfaces closest to the major axis approaches a critical value proportional to the nematic coherence length λ_n, the capillary force approaches the difference in free energy driving force ($\mathcal{C} \to \Delta F$). This results in a critical slowing down of the interface and the transition from the free growth regime to the impingement/defect formation regime. The conditions under which this occurs for the elliptic case cannot result in the formation of a +1 disclination which later splits, as is observed for circular domains [121]. Instead, a pair of $+\frac{1}{2}$ disclinations form directly along the major axis of the elliptic domain near the two (ellipse) focal points. Simultaneously, the isotropic/nematic

interfaces in the central region impinge, forming a well-aligned central region along the minor-axis of the elliptic domain. This defect formation mechanism is the confinement-driven analogue to the defect "shedding" mechanism discovered by Wincure and Rey for free growth of nematic droplets in an isotropic matrix phase [112]. In both cases, defects are formed at the isotropic/nematic interface due to frustration between bulk droplet texture and interfacial anchoring.

Finally, the fully nematic domain relaxes towards the equilibrium state, shown in the final sets of images in Figure 4.1 for the domains with aspect ratios $R = \{1.05, 1.6, 2\}$. This relaxation involves simultaneous motion of the disclinations along the major axis and bulk reorientation. The relaxation mechanism for circular domains has been shown to be governed by the competition of bulk elasticity and surface anchoring strength [121]. Elliptic domains introduce an additional contribution: the variation of the curvature of the boundary. Figure 4.2 shows the evolution of the distance between defect cores for the formation process of each of the domains simulated. At equilibrium, the defect separation distance is found to increase with increasing aspect ratio which occurs without any changes in bulk elasticity or surface anchoring strength. This behaviour can be explained by quantifying the mean curvature imposed by the elliptic boundary conditions. Figure 4.3a shows the schematic of an ellipse in polar coordinates and the mean curvature κ as a function of θ for ellipses of increasing aspect ratio. As aspect ratio increases, there is stronger deviation in curvature with θ, leading to two distinct regions: (i) a high-curvature region outward by the ellipse focal points and (ii) low-curvature regions elsewhere. Thus as aspect ratio increases, the combination of geometry and anchoring effects increasingly impose highly localized deformation of the nematic in the focal regions of the ellipse, which results in equilibrium textures with defects located in these regions.

4.4 Electric Field Switching

Field-switching dynamics simulations were performed for the range of aspect ratios $R = (1, 2]$ using the fully-formed equilibrium textures from Section 4.3 as initial conditions. Electric field orientation was chosen to be parallel to the major axis because this results in the most significant field-driven effect on the texture. If the field were instead aligned parallel to the minor axis, the field would predictably increase the degree of existing alignment. In the following discussion, the equilibrium field-driven textures are first presented. The reorientation dynamics are then discussed afterwards.

However, before moving to the results, it is useful to define a metric for analyzing the external field-switching and relaxation dynamics quantitatively. A volume-averaged

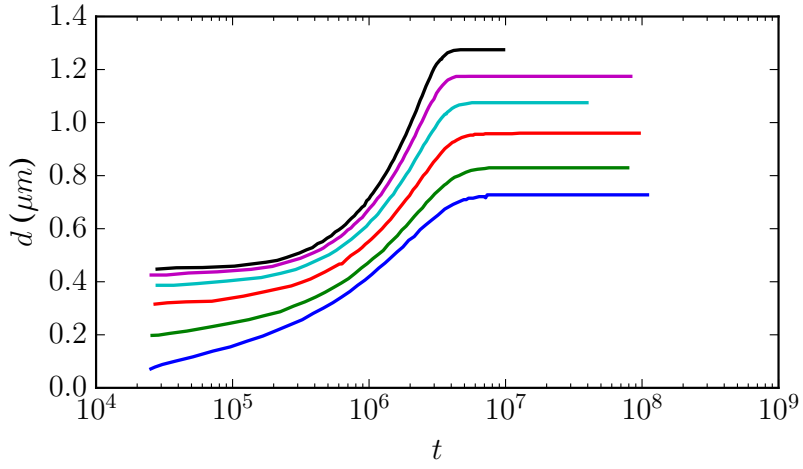

Figure 4.2: Evolution of the distance d between defects for different aspect ratio equilibrium elliptic domains. In order from bottom curve to top, the aspect ratio is $R = \{1.05, 1.2, 1.4, 1.6, 1.8, 2.0\}$.

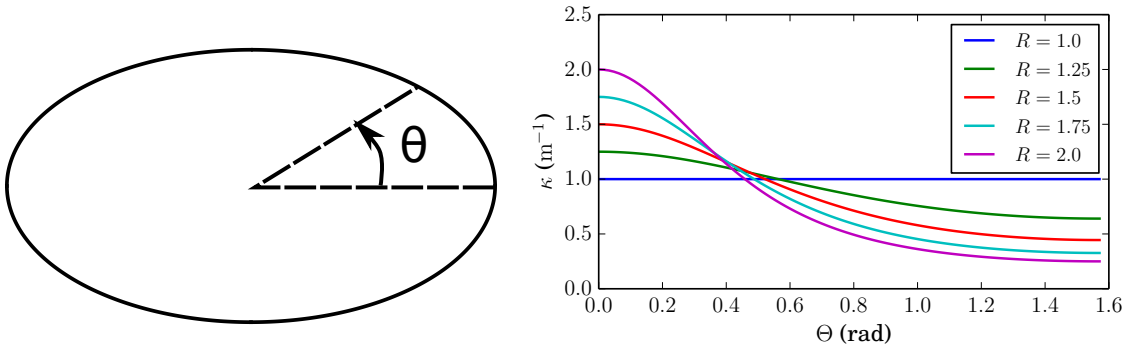

(a) (b)

Figure 4.3: (a) Schematic of an ellipse in polar coordinates; (b) plot of the mean curvature κ of the ellipse boundary versus polar angle θ.

nematic uniaxial order parameter S_d and director $\mathbf{n}_d$ can be determined [33] through

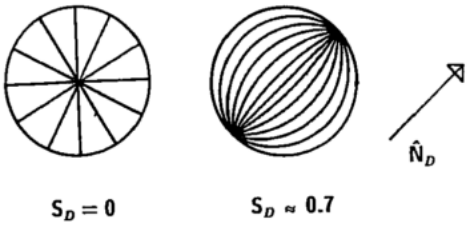

Figure 4.4: Schematic of relative droplet order parameter for two different textures. In the radial texture (left), the radial symmetry results in zero preferred alignment and thus $S_d \to 0$. From ref. [33].

eigendecomposition of the volume-averaged alignment tensor $\mathbf{Q}_d$:

$$\mathbf{Q}_d = V^{-1} \int_V \mathbf{Q}\, dV \tag{4.13}$$

where V is the volume of the domain. The droplet scalar order parameter S_d is analogous to nematic scalar order parameter S in Equation 3.4, where $S_d \to 0$ corresponds to a texture with no preferred alignment and $S_d \to 1$ corresponds to uniform aligned along $\mathbf{n}_d$. This interpretation is illustrated in Figure 4.4 [33]. From a general optical applications perspective, assuming a fixed $\mathbf{n}_d$, lower values of S_d then correspond to textures which scatter light, while higher values of S_d correspond to aligned textures with better optical transparency [122].

4.4.1 Field-driven Equilibrium Textures

Simulations of application and release of an electric field, with strengths in the range $E \in (0\,\mathrm{V\,\mu m^{-1}}, 5\,\mathrm{V\,\mu m^{-1}}]$ were performed. Two different field-switching regimes were observed where the droplet director $\mathbf{n}_d$ either remained constant (at low field strength) or reoriented (at high field strength). Visualizations of the equilibrium alignment tensor fields for both regimes are shown in Figure 4.5 and Figure 4.6, respectively. These results demonstrate that a critical field strength E_c exists depending on the domain aspect ratio, anchoring strength and LC material properties.

For the $E < E_c$ regime, there is a small response in the domain texture resulting in a change in the droplet scalar order parameter S_d, but not the droplet director. Defects are driven inwards along the major axis which results in larger field-aligned focal regions. Upon release of the field, the domain is restored to the initial equilibrium texture resulting from the formation process.

For the $E \geq E_c$ regime, there is a large response of the domain where the disclinations have migrated to be along the minor axis. The reorientation of $\mathbf{n}_d$ has resulted in a strongly field-aligned domain. This is achieved through the domination of electric field forces over surface anchoring forces. In the range of studied field strengths, defect "escape" is not observed. However, it is expected for very strong electric field or very weak surface anchoring conditions [15]. Upon release of the field the domain is restored to the initial equilibrium texture resulting from the formation process.

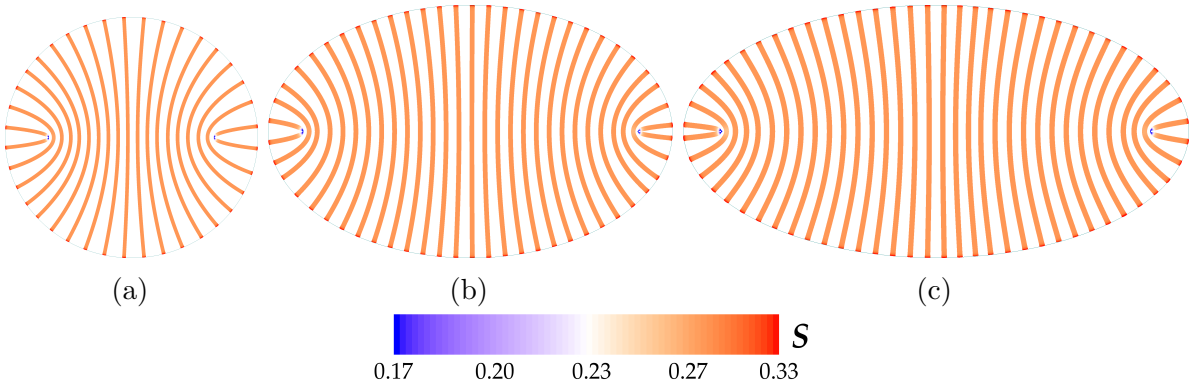

Figure 4.5: Hyperstreamline visualizations of field-driven textures with $E < E_c$ for domains with aspect ratio (a) $R = 1.05$, (b) $R = 1.6$, and (c) $R = 2.0$.

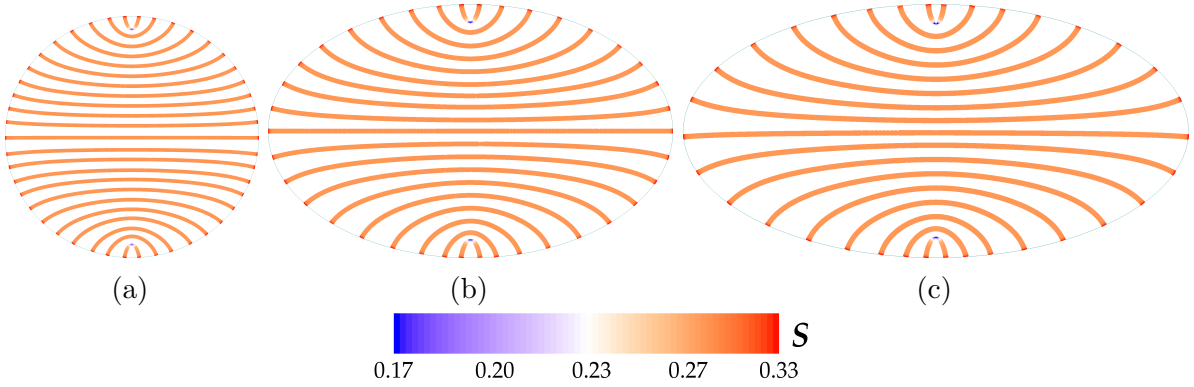

Figure 4.6: Hyperstreamline visualizations of field-driven textures with $E > E_c$ for domains with aspect ratio (a) $R = 1.05$, (b) $R = 1.6$, and (c) $R = 2.0$.

Figure 4.7 shows droplet scalar order parameters S_d for simulated equilibrium domains at different field strengths both below and above E_c. As electric field strength is increased (but

still held below E_c) the effect is minimal on S_d. This can be explained through observation of the field-driven domain textures in Figure 4.5; while the area aligned with the field (focal regions) increases in size and uniformity, this is achieved through a simultaneous reduction in the central region that is aligned orthogonal to the field. Thus the net increase in nematic order in the focal regions is almost completely offset by decreased order in the central region.

As electric field strength is increased above E_c there is a significant deformation of the domain texture, both with respect to S_d and $\mathbf{n}_d$. This response is similar to the Freedericksz transition observed in planar LC domains exposed to an external field [81]. In all simulations the droplet director $\mathbf{n}_d$ is observed to reorient parallel to the applied field vector (major axis). The observed response of S_d after application of the field is more complex. For low aspect ratios $R < 1.5$ the electric field is found to result in a field-aligned nematic domain with droplet scalar order parameter greater than in the absence of the field. This is the traditional mechanism associated with PDLC films used for privacy glass, where in the "off" state they scatter substantially more than in the "on" state. For higher aspect ratios $R > 1.5$ the *opposite* behaviour is observed; even though the domain texture is field-aligned, the droplet scalar order parameter is substantially lower in the field-driven state compared to without the field. This corresponds to an increase in light scattering, regardless of the orientation of the droplet director $\mathbf{n}_d$. This "reverse-mode"-like mechanism is typically associated with PDLC films formed using a nematic LC with negative dielectric anisotropy [123].

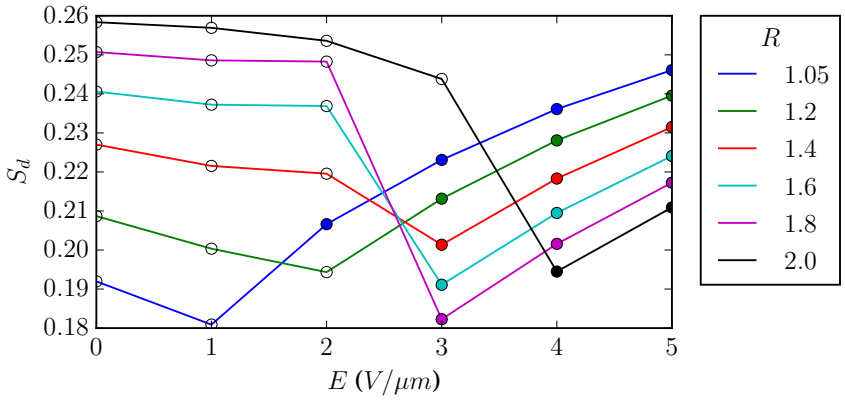

Figure 4.7: Plot of droplet scalar order parameter S_d versus electric field strength E for $R = (1, 2]$ where $\circ$ and $\bullet$ glyphs correspond to $\mathbf{n}_d \perp \mathbf{E}$ and $\mathbf{n}_d \parallel \mathbf{E}$, respectively.

4.4.2 Field-driven Dynamics Textures

Figure 4.8 shows simulation results of the field-driven dynamics for the $R = 2$ case for $E = 5\,\mathrm{V}\,\mu\mathrm{m}^{-1} > E_c$. These results are representative of simulation results for all domains $R = (1, 2]$. A sequence of three distinct dynamic regimes were observed: bulk growth/recession, disclination/bulk rotation, and bulk relaxation.

The *bulk growth/recession regime* involves the simultaneous growth of the field-aligned focal regions and recession of the field-orthogonal central region which involves the motion of the disclinations inwards along the major axis. This regime was observed for both the $E < E_c$ and $E > E_c$ cases, where in the former the net change in the domain texture was minimal (see Figure 4.7). In the latter case ($E > E_c$) as shown in Figure 4.10c, this regime involves a monotonic decrease in the droplet scalar order parameter $S_d \to 0$, corresponding to a radial texture (maximal light scattering).

The *disclination/bulk rotation* regime follows the bulk growth/recession regime; as the distance between the disclinations decreases (along the major axis) the repulsive nematic elastic forces approach that of the applied field. At that point, the defect separation distance becomes constant and rotation occurs. The initiation of this regime is found to involve a sharp transition of the droplet director from being orthogonal to parallel to the field direction (Figure 4.10c). This discontinuous transition of $\mathbf{n}_d$ is enabled by the radial texture of the droplet, where $S_d = 0$ making $\mathbf{n}_d$ a degenerate quantity. Disclinations and bulk nematic texture simultaneously rotate about the center of the domain, increasing domain field alignment rapidly (Figure 4.10c).

The *bulk relaxation* regime involves simultaneous rotation and expulsion of the disclinations from the central region along the minor axis. The rotation process ceases as disclinations approach the boundaries and surface anchoring forces balance out bulk elastic forces. Higher electric field strengths likely exist which would overcome surface anchoring and result in an "escape" texture [15], but they exceed the field strengths typically used in PDLC applications [118], the focus of this study.

The observed mechanism predicted by simulations provides a more refined understanding of the mechanism predicted by Drzaic [6]. As opposed to short timescale bulk reorientation followed by long timescale defect motion, simulations predict that the mechanism is instead through the *simultaneous* motion of disclinations, growth of field-aligned regions, and recession of nonaligned regions. As originally predicted by Drzaic, the long timescale component of the mechanism is through the motion of defects transitioning from one axis of the domain to the other, but the short timescale mechanism also involves linear defect motion and reorientation dynamics in the outer regions of the domain.

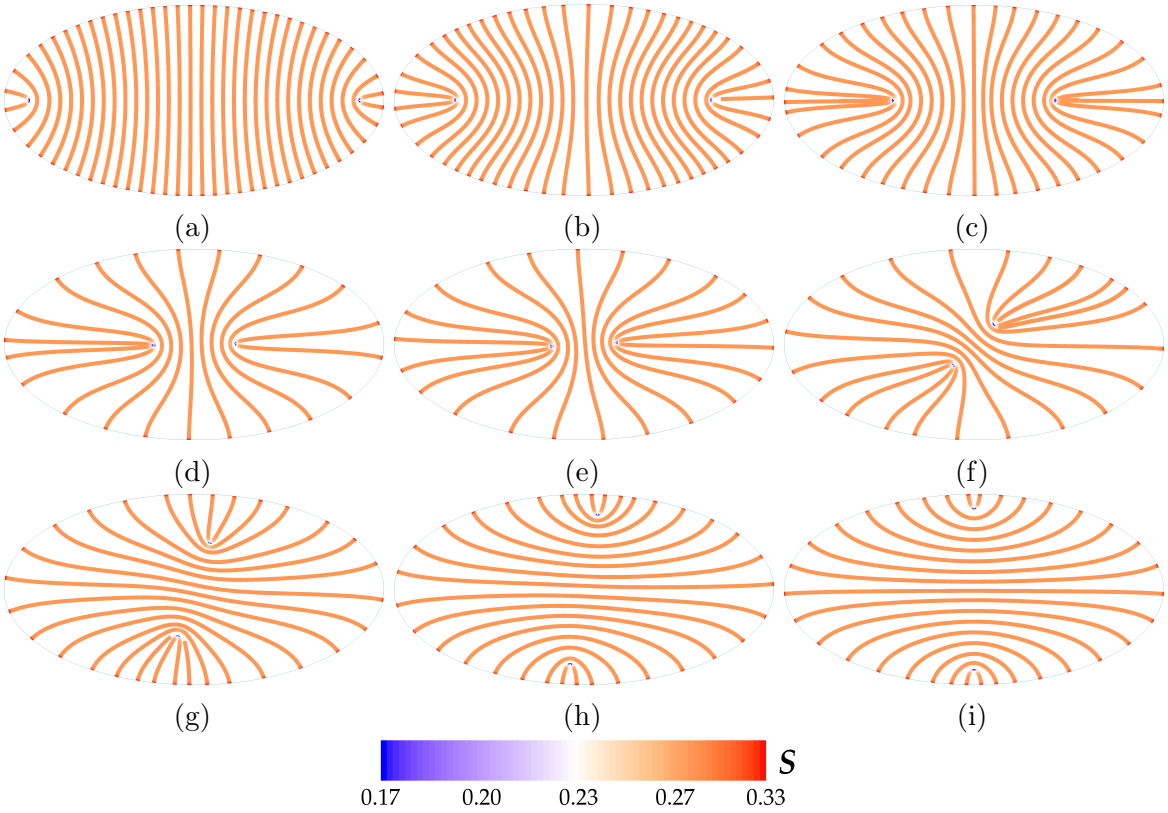

Figure 4.8: Hyperstreamline visualizations of the field-on texture dynamics for the $R = 2$ domain with $E = 5\,\mathrm{V/\mu m}$ and $t = \{0,\ 5.25 \times 10^5,\ 1.05 \times 10^6,\ 1.55 \times 10^6,\ 1.89 \times 10^6,\ 2.11 \times 10^6,\ 2.33 \times 10^6,\ 2.71 \times 10^6,\ \geq 5.00 \times 10^6\}$.

Figure 4.9 shows simulation results of the domain dynamics upon release of the field. This release regime is similar to the driven mechanism but in reverse. There are two significant differences in time scale and evolution of the droplet director, however. The time scales associated with release are an order of magnitude larger compared to their electric field-driven analogues, which is expected due to the different in magnitudes of the surface anchoring and electric field strengths. The ratio of their characteristic lengths, $\frac{\lambda_s}{\lambda_e} \approx 10$, demonstrates this. The other difference is that during the disclination/bulk rotation regime, the droplet director $\mathbf{n}_d$ continuously rotates instead of exhibiting a sharp transition. S_d also does not decrease to zero. The final field-off equilibrium textures in all restoration simulations were found to be the same as those from the formation simulations, indicating these electric field-induced deformations of the nematic domain are viscoelastic. That is,

while the field-on and field-off dynamics are different, the start and end textures are the same.

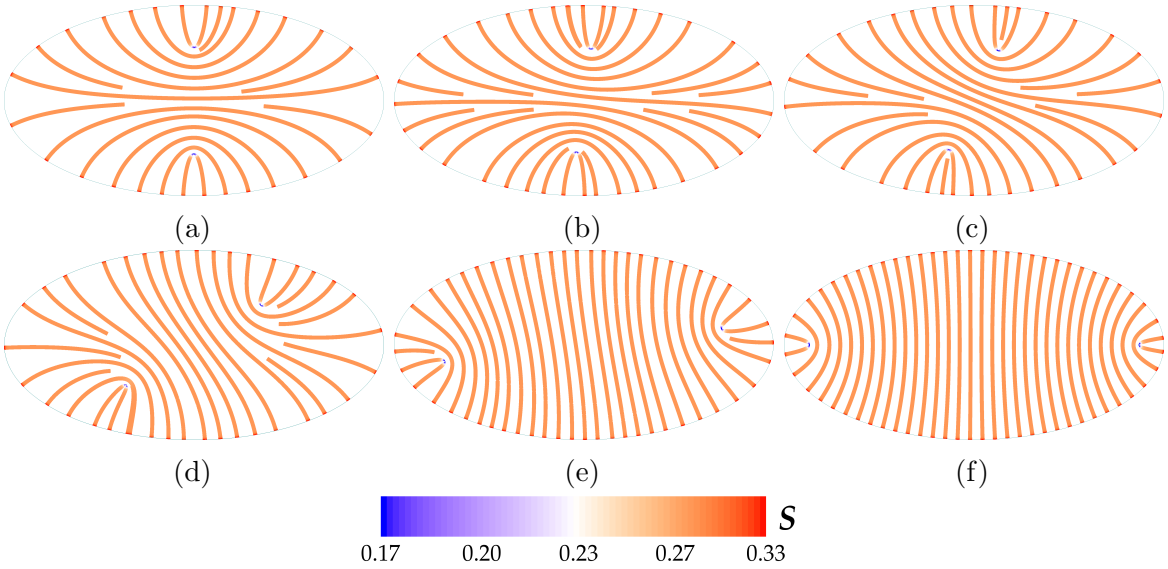

Figure 4.9: Hyperstreamline visualizations of the release texture dynamics for the $R = 2$ domain, continued from Figure 4.8i (referenced to $t = 0$), with $t = \{1.79 \times 10^6, 6.75 \times 10^6, 8.55 \times 10^6, 1.03 \times 10^7, 1.26 \times 10^7, \geq 1.60 \times 10^7\}$.

4.5 Conclusions

In this work, a simulation-based study was performed on the formation and electric field switching dynamics of elliptic cylinder nematic domains. The observed nematic reorientation dynamics were found to have a complex dependence on geometry (aspect ratio) and external field strength. Both formation and reorientation dynamics were found to be governed by the presence and motion of defects within the domain. Geometry of the domain, specifically aspect ratio, was found to strongly affect domain texture by providing regions of high curvature to which nematic defects are attracted. Simulations also predict the presence of a geometry-controlled transition from nematic order enhanced by an external field (low aspect ratio) to nematic order frustrated by an external field (high aspect ratio).

Equilibrium and dynamic behaviour of elliptic nematic domains are found to significantly differ from circular ones, which opens up new possibilities for electro-optical mechanisms for

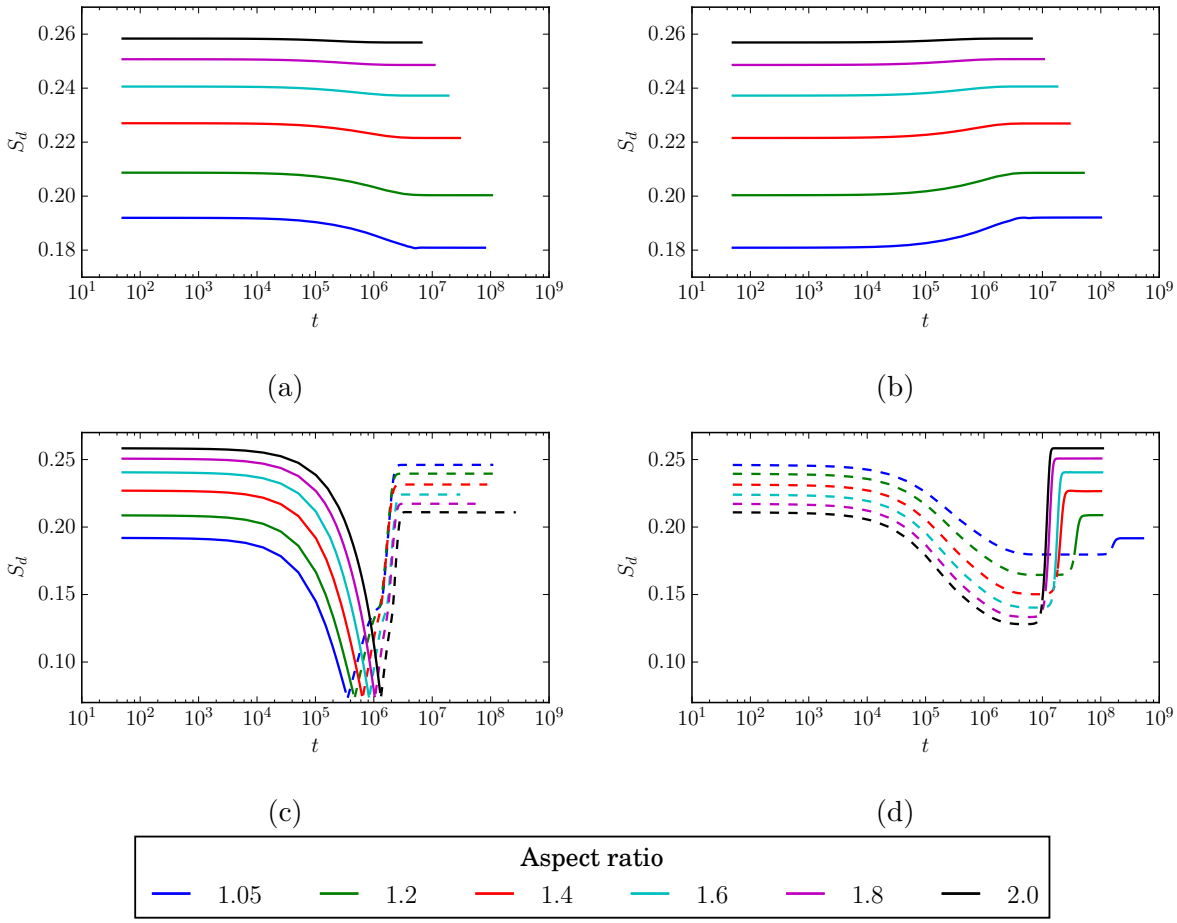

Figure 4.10: Droplet scalar order parameter evolution versus time for domains with a range of aspect ratios $R = (1, 2]$ with electric field applied (a,c) and following release (b,d): (a) $E = 1\,\mathrm{V/\mu m} < E_c$ (driven); (b) $E = 1\,\mathrm{V/\mu m} < E_c$ (release); (c) $E = 5\,\mathrm{V/\mu m} > E_c$ (driven); and (d) $E = 5\,\mathrm{V/\mu m} > E_c$ (release). Droplet director orientation $\mathbf{n}_d$ is indicated by line type: solid and dashed correspond to $\mathbf{n}_d \perp \mathbf{E}$ and $\mathbf{n}_d \parallel \mathbf{E}$, respectively.

applications of nematic-filled capillaries. Experimental validation of the presented results is needed, which can be achieved through comparison with future electro-optical dynamics measurements of nematic-filled capillaries as has been done for PDLC films [6]. Finally, the results presented support the use of simulation-based methods for design of PDLC optical functional materials, although further improvements to the methodology are still needed to realistically capture droplet behaviour.

Chapter 5

Formation and Field-driven Dynamics of Nematic Spheroids[1]

5.1 Overview

Following up on the previous study, fully three-dimensional continuum simulations were performed to study the dynamics of micron-scale spheroidal NLC droplets of varying shape. Nematic droplets are one of the simplest inherently defect-containing LC structures and are relevant to PDLC-based "smart" window technology and as discussed in Section 2.5, the geometry of droplets in PDLC films can be controlled using a variety of methods [66]. Simulation results include nematic phase formation and external field-switching dynamics of nematic spheroids ranging in shape from oblate to prolate. Results include both qualitative and quantitative insight into the complex coupling of nanoscale defect dynamics and structure transitions to micron-scale reorientation. Dynamic mechanisms are presented and related to structural transitions in LC defects present in the nematic domain. Domain-averaged metrics including order parameters and response times are determined for a range of experimentally-accessible electric field strengths.

[1]This chapter is derived from work originally published in: F. Fu and N. M. Abukhdeir. *Soft Matter*, 13:4890–4902, 2017.

Table 5.1: Simulation parameters for spheroid study. Material-based parameters were based on estimates of pentyl-cyanobiphenyl.

Parameter	Value	Units	Ref.
T^*_{ni}	307.35	K	111
a_0	1.4×10^5	$\mathrm{J\,m^{-3}\,K^{-1}}$	111
b	1.8×10^6	$\mathrm{J/m^3}$	112
c	3.6×10^6	$\mathrm{J/m^3}$	112
k_{11}	2.5×10^{-12}	J/m	125
k_{22}	1.7×10^{-12}	J/m	126
k_{33}	3.0×10^{-12}	J/m	125
k_{24}	4.1×10^{-13}	J/m	see text
$\epsilon_\parallel$	16.5	(relative)	125
$\epsilon_\perp$	8.2	(relative)	125
μ_r	0.055	$\mathrm{kg\,m^{-1}\,s^{-1}}$	113
α	10^{-4}	$\mathrm{J/m^2}$	35

5.2 Methodology

The model parameters used approximate 5CB and are given in Table 5.1. Values of parameters were chosen according to empirical models corresponding to a temperature of $T = 307\,\mathrm{K}$ (below T_{ni}) [112, 124, 125], which is why some parameters such as the relative dielectric permittivities are different compared to the simulations from Chapter 4 (Table 4.1).

Unlike the previous study of elliptic capillaries, the single elastic constant approximation is not used, and so the elastic free energy is represented by the full expression in Equation 3.7. The relations between the Frank-Oseen and Landau–de Gennes elastic constants (Equations 3.8–3.11) were used to to arrive at LdG elastic constants which are consistent with experimental measurements for 5CB. Note that the saddle-splay constant k_{24}, which has proven difficult for researchers to measure consistently [25, 126, 127], was chosen such that the elastic energy penalty term L_{24} remained positive ($k_{24} = 0.25k_{22}$). However, this is not a strict condition of the model and negative L_{24} is possible so long as the Frank-Oseen elastic constants satisfy the Ericksen inequalities (Equations 3.2 and 3.3).

In order to study the formation and field-driven dynamics of spheroidal nematic domains relevant to electro-optical applications such as PDLCs, simulations were performed of nematic spheroids with fixed volume corresponding to an initial "unstretched" sphere of diameter 500 nm. The initial sphere was consistently elongated or contracted along

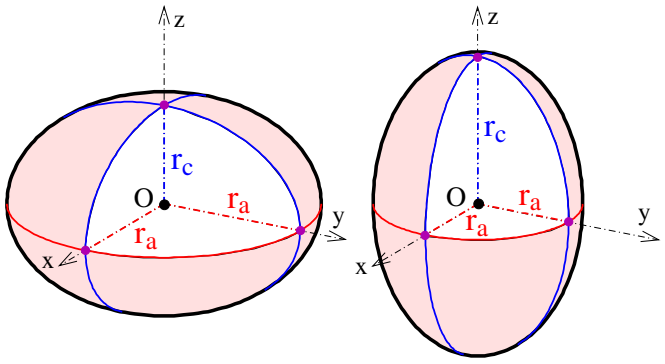

Figure 5.1: Oblate (left, $r_c < r_a$) and prolate (right, $r_c > r_a$) spheroids. From ref. [129].

a single direction with spheroid volume being maintained constant. The aspect ratio $R = \frac{r_c}{r_a}$ of the resulting spheroids was then defined as the length ratio between the axis of elongation/contraction ($2r_c$) and the remaining (equivalent) axes of the spheroid ($2r_a$) as shown in Figure 5.1. Thus, oblate spheroids are denoted by $R < 1$ and prolate spheroids by $R > 1$. Domains with varying aspect ratio $R \in [0.5, 2]$ were simulated based upon experimental evidence regarding the expected variation in PDLC domain shape [6,65,69,128].

These simulations were performed in three stages: (i) formation of the nematic phase from an initially disordered (high temperature) phase, (ii) application of an electric field corresponding to the "on" (transparent) state of a PDLC film, and (iii) relaxation resulting from release of the electric field, corresponding to the "off" (translucent) state of a PDLC film.

For the formation dynamics simulations, heterogeneous nucleation of the nematic phase at the solid/LC interface was once again assumed. The initial nematic boundary layer was therefore modelled similarly to the method given in Chapter 4 for the two-dimensional case, in which the nematic at the boundary is aligned perpendicular to the surface in accordance with the homeotropic surface anchoring. However, instead of analogously describing the initial alignment tensor field using an analytical equation in terms of a spherical coordinate system, the surface normal vector was simply extracted numerically based on the physical geometry of the mesh elements at the surface.

For the field dynamics simulations, a range of experimentally accessible electric field strengths up to $14\,\mathrm{V\,\mu m^{-1}}$ were applied. Simulations of electric field switching were conducted using the equilibrium textures as initial conditions from formation for each field strength studied.

5.3 Nematic Formation Dynamics

Formation dynamics simulations were initially performed for oblate spheroids of aspect ratio $R \in [0.5, 1)$. This geometry can be considered a rotational extrusion of a two-dimensional ellipse about its minor axis. It is therefore comparable to the previous simulations of nematic elliptic capillaries [130] in which a sequence of three different growth regimes were identified during nematic formation: (i) free growth, (ii) defect formation, and (iii) bulk relaxation. The free growth regime consists of the stable nematic "shell" growing into an unstable isotropic phase, with the bulk nematic orientation being commensurate with the homeotropic surface anchoring conditions. Next, the defect formation regime involves the impingement of the nematic-isotropic interface on itself. This results in the simultaneous formation of a pair of $+\frac{1}{2}$ disclination lines along the major axis of the elliptic cross-section of the capillary. Finally, during bulk relaxation, the domain as a whole relaxes to its equilibrium state through simultaneous disclination motion and bulk reorientation.

The simulation results of the formation process for a $R = 0.5$ oblate spheroid are shown in Figure 5.2. The process begins with the initial free growth of the stable nematic boundary layer into the central unstable isotropic region (Figures 5.2a–b). As free growth proceeds, the curvature of the isotropic/nematic interface increases in the focal regions of the spheroid and simultaneously the interface velocity decreases. This critical slowing down of the nematic/isotropic interface [130] may again be explained by Equation 4.12 [76], in which the interface velocity approaches zero as the capillary force increases due to curvature. Eventually, the free growth regime transitions to the defect formation regime.

Figures 5.2c–d show the defect formation regime dynamics. A $+\frac{1}{2}$ disclination loop forms in the focal region through a interface-driven defect "shedding" mechanism [112]. Simultaneously, the isotropic/nematic fronts in the equatorial region impinge. This is followed by the bulk relaxation regime where the nematic texture relaxes through bulk reorientation and the disclination loop expands towards the focal boundaries. As expected, the formation process for oblate nematic spheroids is analogous to that of elliptic capillaries [130] due to their geometric similarities.

In contrast, prolate nematic spheroids experience different dynamics. Figure 5.3 shows the formation dynamics of a prolate nematic spheroid in the free growth (Figure 5.3a), defect formation (Figures 5.3b–d), and bulk relaxation (Figures 5.3e–f) regimes. Despite being topologically equivalent to the oblate spheroid, the defect formation mechanism for a prolate spheroid is substantially more complex. First, a pair of +1 point defect-like structures form as the high-curvature interfaces in the focal regions impinge (Figure 5.3b). These structures are not true point defects in that the nematic phase within the spheroid

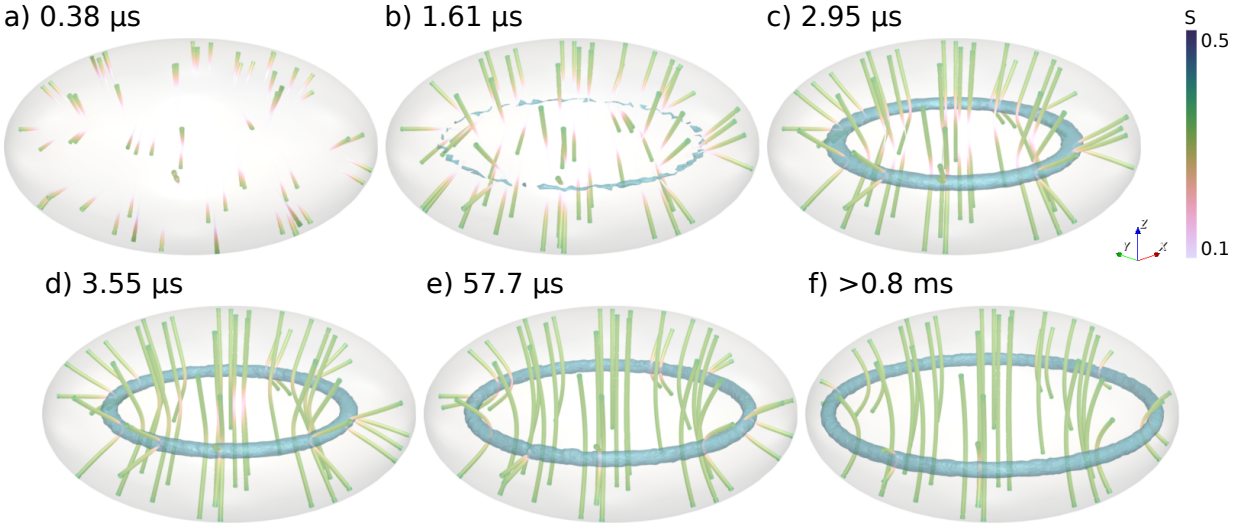

Figure 5.2: Hyperstreamline visualizations of the formation process of an oblate ($R = 0.5$) nematic spheroid from an initially isotropic state. The defect region is indicated by the isosurface (blue, $P \approx 0.03$).

is not fully-formed. The defect formation mechanism proceeds through the continued impingement of the isotropic/nematic interface along the equator. This results in the point-like defects growing into the center of the spheroids where they impinge to form a high-energy +1 disclination line. As expected based on past two-dimensional simulation results [27, 120] and defect energy scaling analysis [119], this defect line then splits into a lower energy $+\frac{1}{2}$ disclination loop. Notably, the simulations predict the dynamic mechanism through which this transition occurs. Figures 5.3c,d show that there is a degeneracy in the direction in which the +1 disclination line splits, which results in this splitting direction varying along its length. The resulting $+\frac{1}{2}$ disclination loop then undergoes an elastic relaxation process driven by defect line tension, bending, and torsion.

Figure 5.4 shows the uniaxial S and biaxial P nematic order parameters in the vicinity of the central region of the prolate spheroid during the disclination splitting process. This process is similar to disclination line-loop dynamics observed by Shams and Rey [131, 132], for which they developed a so-called "*nematic elastica*" model for defect dynamics which captures line tension and bending of disclinations.

Figures 5.4a–b show further detail of the formation of an unstable +1 disclination line originating from the joining of a pair of disclination lines growing into the unstable isotropic center of the prolate spheroid. Figure 5.4b shows that the central region of the fully-formed

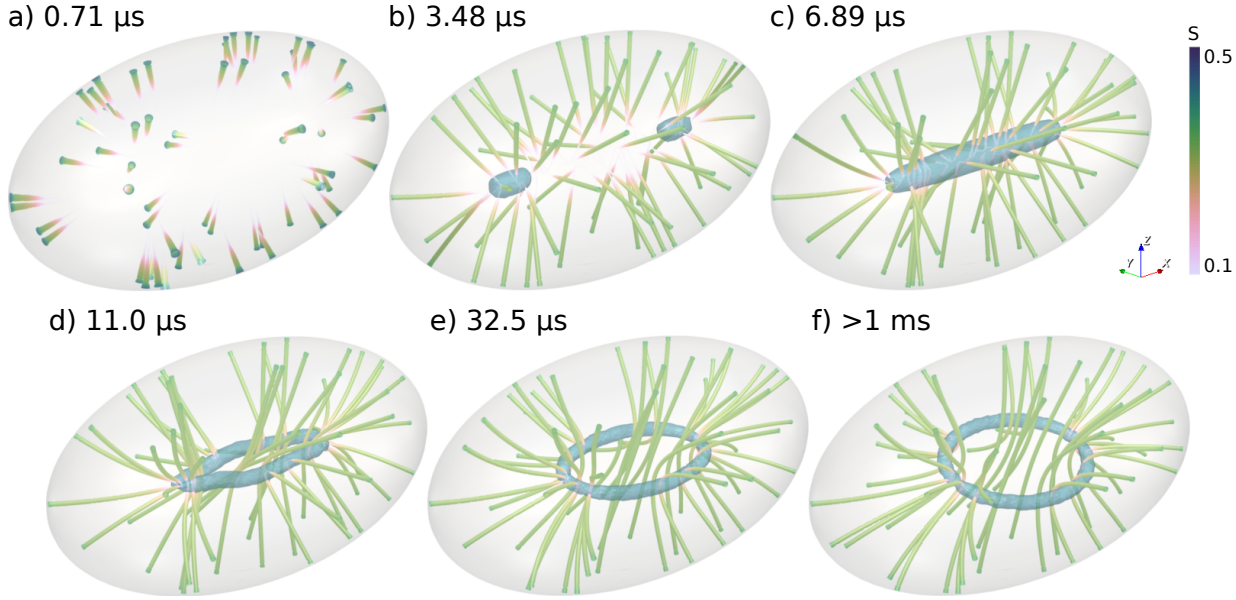

Figure 5.3: Hyperstreamline visualizations of the formation process of a prolate ($R = 2$) nematic spheroid from an initially isotropic state. The defect region is indicated by the isosurface (blue, $P \approx 0.03$). Note the loop orientation in (d-f) is aligned along the major axis, and the transition from (e) to (f) involves a rotation about that axis.

+1 disclination line is uniaxial, in agreement with past theoretical predictions [133]. Figure 5.4c shows the initial distorted $+\frac{1}{2}$ disclination loop immediately following the splitting process. The loop has significant bending and torsion resulting from the degeneracy in the splitting process. It eventually relaxes into a loop with no torsion (Figure 5.4d) where the central region of the spheroid is well-aligned with little distortion of the nematic director. The final defect loop is described by a local decrease in S and an increase in P.

Finally, following the complex defect formation regime, the bulk relaxation regime is observed where the fully-formed nematic texture of the spheroid relaxes through bulk reorientation and expansion of the disclination loop. Comparing the equilibrium nematic textures of the oblate (Figure 5.2f) and prolate spheroids (Figure 5.3f), the oblate spheroid exhibits a relatively uniform nematic texture due to the surface exhibiting commensurate anchoring conditions with the bulk elasticity. The prolate spheroid exhibits a more non-uniform texture, and is more similar to the radial-like textures often observed in spherical droplets. The differences are hypothesized to occur due to the fact that the prolate spheroid, unlike the oblate one, has two short axes of equal length. Combined with the homeotropic anchoring conditions, this results in a highly frustrated domain with a less uniform texture.

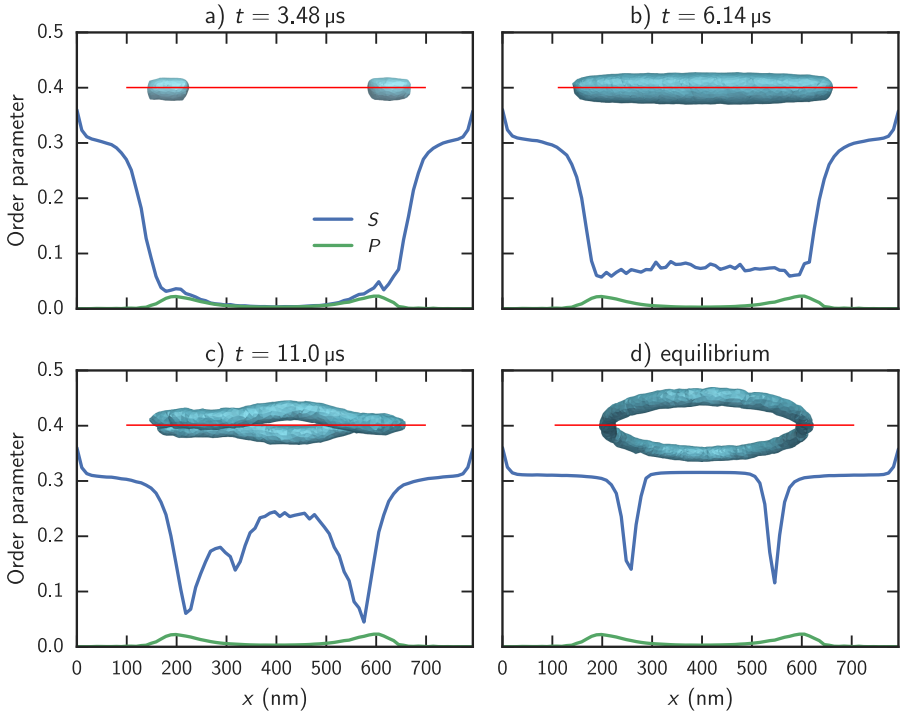

Figure 5.4: Plots of uniaxial S and biaxial P nematic order parameters versus position along the major axis of the prolate ($R = 2$) spheroid (illustrated in red) showing the progression of $+1$ disclination formation and splitting process.

5.4 Electric Field Switching

Electric-field driven reorientation of nematic droplets is a key process in the operation of PDLC-based technology. Past experimental research has shown that domain shape has a significant effect on the electro-optical switching process and can result in shorter switching times [66, 91]. These simulations were performed for both oblate and prolate spheroids using the equilibrium states resulting from the formation process. Electric fields were again applied in the direction parallel to the major axis of the droplets (x-axis) which corresponds to the direction orthogonal to the optical axis of the spheroid at equilibrium for the case of PDLC film stretching. Since 5CB is a positive dielectric anisotropy LC, nematic orientation parallel to the electric field is energetically favoured. Thus, imposition of the electric field orthogonal to the optical axis results in the maximum amount of field-induced reorientation. While this is not the most typical setup for a PDLC (compare

with Figure 2.11, in which the voltage is applied across the top and bottom of the film, i.e., in the z-axis), it does correspond to an *in-plane* switching mode that has been explored experimentally for PDLC-based devices [4, 134].

The field-switching transition is governed by the competition between domain shape, surface anchoring conditions, electric field strength, and nematic elasticity. The competition between surface anchoring and electric field effects on the nematic domain may be approximated by the ratio of their relevant characteristic lengths λ_e and λ_s (see Equations 4.10 and 4.11). The electric field-induced transition is expected to occur when $\lambda_s/\lambda_e \approx 1$, which results in an electric field strength of $\approx 1\,\mathrm{V\,\mu m^{-1}}$, given $\lambda_s \approx 100\,\mathrm{nm}$. Subsequently, electric fields with strengths ranging from 2–14 $\mathrm{V\,\mu m^{-1}}$ were applied in increments of $2\,\mathrm{V\,\mu m^{-1}}$.

Two different field-switching regimes were observed depending on the magnitude of the electric field, corresponding to a Freedericksz-like transition. For electric fields strengths $E < E_c$, the nematic texture changes only slightly without undergoing bulk reorientation in the field direction. In contrast, for $E > E_c$, the texture undergoes reorientation to a field-aligned state. Overall, a general sequence of three dynamic regimes, consistent with the previous observations of nematic capillaries (Chapter 4) [130], can be identified:

Regime I. *Bulk growth and recession*, involving growth of the field-aligned focal regions and recession of the misaligned central region;

Regime II-A. *Disclination and bulk rotation*, involving rotation of the disclination loop orthogonal to the field direction; and

Regime II-B. *Bulk relaxation*, involving expansion of the disclination loop until the force from the applied field equilibrates with the elastic and anchoring forces in the system.

In all cases it was observed that upon release of the electric field, the nematic texture was restored to the equilibrium texture from the earlier formation process. Additionally, simulations were performed starting with the field-aligned nematic textures decreasing the electric field strength in increments of $2\,\mathrm{V\,\mu m^{-1}}$. Hysteresis in the critical field strength was not observed for the $2\,\mathrm{V\,\mu m^{-1}}$ increment used in this study, i.e. E_c was not observed to be different for the driven process versus the release process.

Figure 5.5 shows simulation results of the field-driven switching dynamics of a $R = 0.5$ oblate nematic spheroid where $E > E_c$. Initially, the disclination loop contracts along the x-axis (Figures 5.5b–c, dynamic regime I) as the field-aligned regions grow. This process ends once the defect loop is "compressed" sufficiently into an elliptic shape, indicating the elastic energy penalty approaches that of the applied field. For oblate spheroid simulations where $E < E_c$ (not shown), dynamic regime I was the only dynamic regime observed.

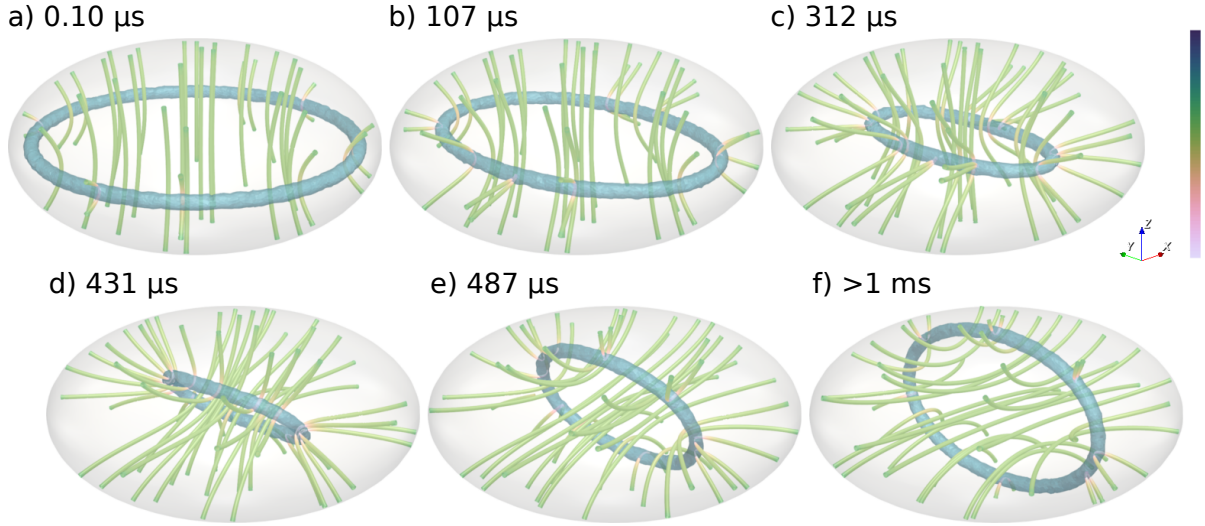

Figure 5.5: (a-f) Hyperstreamline visualizations of the electric field-switching process for $E = 14\,\mathrm{V\,\mu m^{-1}} > E_c$ applied along the x-axis of an oblate ($R = 0.5$) spheroid starting from (a) the equilibrium texture (following formation) and proceeding to (f) the field-driven equilibrium texture. The defect region is indicated by the isosurface (blue, $P \approx 0.03$).

Figures 5.5d–e show the disclination/bulk rotation regime that follows. Unlike the dynamic mechanism for field-switching of nematic capillaries [130], the rotation of the loop is accompanied by both expansion of the loop and bulk rotation of the nematic director throughout the spheroid. This corresponds to a combination of dynamic regimes II-A and II-B.

Figure 5.6 shows the field-driven switching dynamics of a $R = 2$ prolate spheroid where $E > E_c$. The dynamic regimes observed here are more similar to those for nematic capillaries than for oblate spheroids. In particular, the transition between dynamic regime II-A and II-B is more distinct. This result can be attributed to the difference in disclination loop structure between the two cases, which is imposed by their geometries. For the prolate spheroid, as the size of the disclination loop decreases following application of the electric field, the loop becomes a very small circle with diameter on the order of the nematic coherence length. In contrast, the oblate spheroid disclination loop transitions from circular to elliptic after application of the field and the major axis of the elliptic loop maintains the micron-scale size of the spheroid. Next, dynamic regime II-A proceeds (Figures 5.6c–d) with a minimal increase in the defect loop diameter, unlike in the oblate case. Dynamic regime II-B follows, where the disclination loop diameter transitions from nanoscale to micron-scale, corresponding to the length scale imposed by the spheroid geometry.

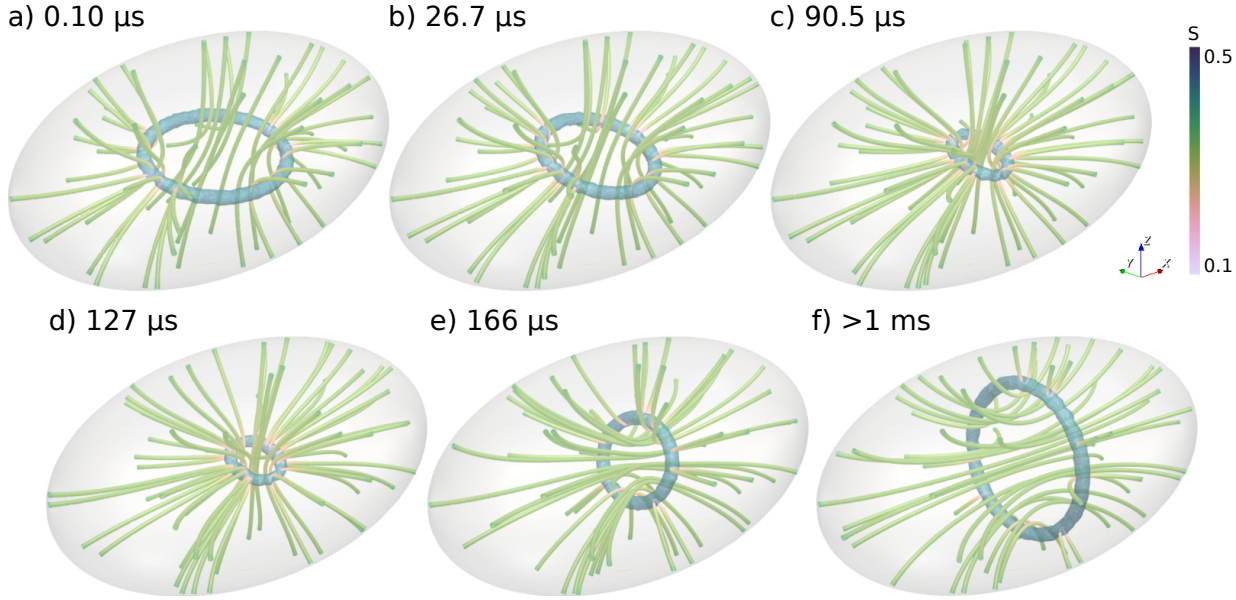

Figure 5.6: (a-f) Hyperstreamline visualizations of the electric field-switching process for $E = 14\,\mathrm{V\,\mu m^{-1}} > E_c$ applied along the x-axis of a prolate ($R = 2$) spheroid starting from (a) the equilibrium texture (following formation) and proceeding to (f) the field-driven equilibrium texture. The defect region is indicated by the isosurface (blue, $P \approx 0.03$).

Upon release of the external field, the nematic texture at equilibrium while the field was applied is now a high-energy state. Relaxation of the texture back to the original equilibrium state is due to a so-called "restoring" force [6] which arises from a combination of confinement geometry and surface anchoring conditions. Figures 5.7–5.8 show simulation results of these dynamic mechanisms for $R = 0.5$ oblate and $R = 2$ prolate spheroids, respectively. Here, the relaxation process is, qualitatively, the reverse of the field-on process. One significant difference was observed for the oblate spheroid, in which the shape of the disclination loop during the relaxation process is different than that for the field-on case.

Focusing on the oblate spheroid, the disclination loop shape during field-on conditions (Figure 5.5c) is elliptic while during release conditions (Figure 5.7b) it is circular. For the field-on case, the elliptic disclination loop has a minor axis parallel to the field direction. This elliptic shape is initially driven by the growth of the field-aligned regions and recession of the unaligned central region within the spheroid. As dynamic regime II-A proceeds, the elliptic character of the disclination loop is enhanced due to its proximity to the spheroid's elliptic cross-section. For the release case, the disclination loop is circular at the beginning of the rotation regime, and continues to maintain this shape throughout the rotation

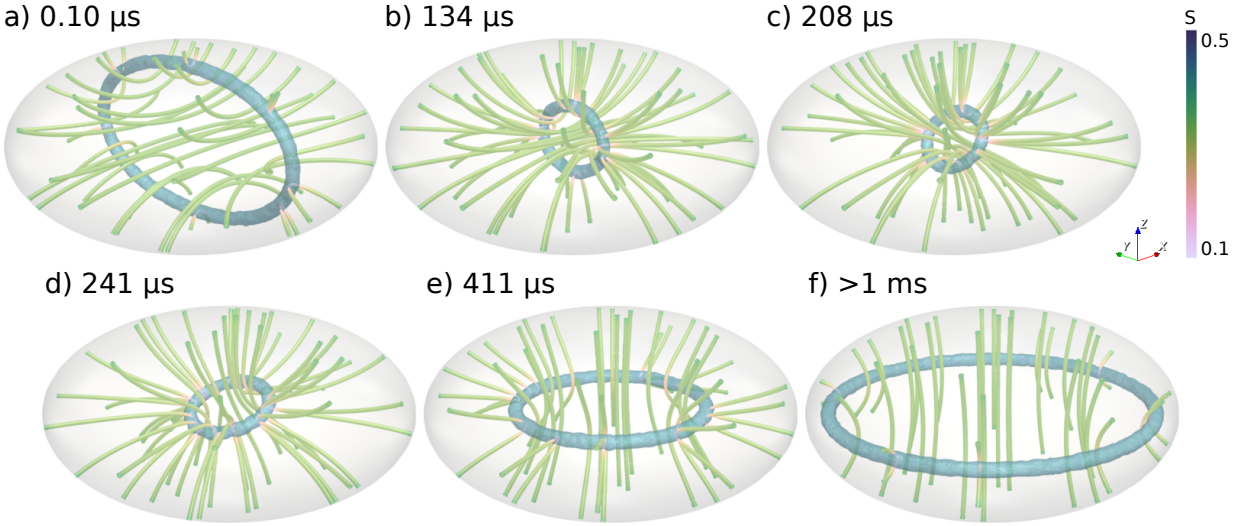

Figure 5.7: (a-f) Hyperstreamline visualizations of the field-off relaxation process after applying a field $E = 14\,\mathrm{V\,\mu m^{-1}} > E_c$ along the x-axis of an oblate ($R = 0.5$) spheroid starting from (a) the field-on equilibrium texture and proceeding to (f) the field-off equilibrium texture. The defect region is indicated by the isosurface (blue, $P \approx 0.03$).

process. As the disclination loop recedes from the elliptic part of the nematic/solid interface, it continuously transitions toward a state of minimum mean curvature which results in a circular shape. As the loop rotates, this circular character of the disclination loop is enhanced due to its proximity to a circular cross-section of the nematic/solid interface. Additionally, unlike in the field-driven case there is a distinct transition from dynamic regime II-A (Figures 5.7b–d) to the dynamic regime II-B (Figures 5.7e–f).

Figure 5.8 shows simulation results of the relaxation of a $R = 2$ prolate spheroid. For this case, the difference in the disclination loop shape between the field-on (Figure 5.6d) and release (Figure 5.8c) is more subtle, but similar to the oblate case. For the field-on case, shown in Figure 5.6d, the disclination loop is slightly elliptic with minor axis parallel to the field direction. As it rotates, the disclination loop transitions to a circular shape resulting from its proximity to a circular cross-section of the nematic/solid interface, as shown in Figure 5.6f. Upon relaxation of the field (Figure 5.8c), the disclination loop adopts a circular shape throughout the rotation process which is followed by transition to an elliptic shape due to its proximity to the elliptic cross-section of the spheroid.

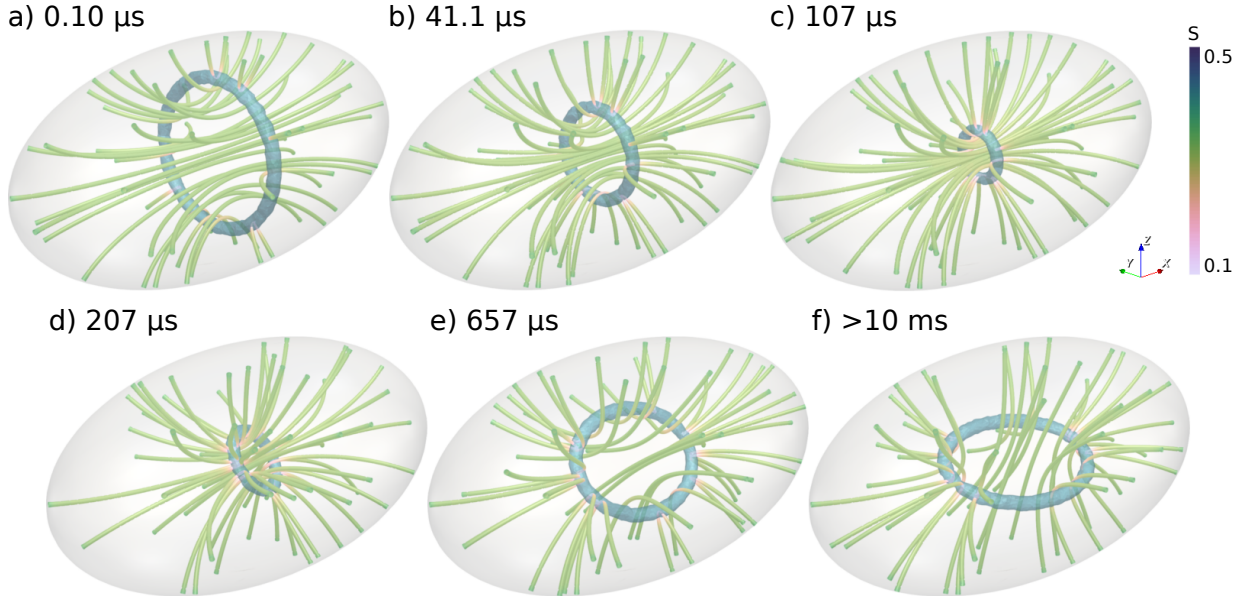

Figure 5.8: (a-f) Hyperstreamline visualizations of the field-off relaxation process after applying a field $E = 14\,\mathrm{V\,\mu m^{-1}} > E_c$ along the x-axis of a prolate ($R = 2$) spheroid starting from (a) the field-on equilibrium texture and proceeding to the (f) field-off equilibrium texture. The defect region is indicated by the isosurface (blue, $P \approx 0.03$).

5.5 Droplet-scale Dynamics

Figure 5.9 shows the evolution of S_d and $\mathbf{n}_d$ for the field-switching and relaxation simulations of oblate (Figures 5.5 and 5.7), prolate (Figures 5.6 and 5.8) and spherical nematic domains ($R \approx 1$, see Appendix C for visualizations) which were presented in the previous section. The droplet order parameter $\mathbf{Q}_d$ was again used to concisely analyze overall texture. For the field-on dynamics where $E < E_c$, evolution of S_d corresponds to only bulk growth/recession. For the $E > E_c$ cases, however, the evolution of S_d for prolate spheroids and spheres involves three dynamic regimes while the oblate spheroid involves two. These quantitative findings support the qualitative observations from the previous section, where for oblate spheroids dynamic regimes II-A and II-B occur simultaneously, whereas for the prolate spheroids they are distinct. Furthermore, the sphere field-switching dynamics are found to be comparable to that of the prolate spheroid, except that the field-alignment of the volume-averaged droplet director $\mathbf{n}_d$ occurs very early in the field-on process for the spherical case.

These trends also indicate that dynamic regime I for spherical and prolate spheroids

occurs in two stages, unlike for the oblate spheroid case. In Figures 5.9a and 5.9c (spherical and prolate spheroids), S_d initially decreases during regime I, followed by a rotation of the spheroid director $\mathbf{n}_d$ and a simultaneous increase in S_d. This is more pronounced for the prolate spheroid than the sphere. However, in Figure 5.9b, S_d does not exhibit this nonmonotonic evolution during dynamic regime I.

The difference in field-on dynamics between prolate/spherical and oblate spheroids may be explained through qualitative comparison of the disclination dynamics of the prolate and oblate spheroids during the initial bulk growth/recession regime. Focusing on the prolate spheroid case, during the first stage of this dynamic regime, the field-aligned regions of the spheroid grow while simultaneously the disclination loop diameter decreases. The decrease in disclination loop diameter does not initially result in interaction of adjacent regions of the loop, which would result in a high-energy elastic interaction of the nanoscale defect "core" regions [119]. During the second stage of this regime, the volume-averaged scalar order parameter evolution decreases. This results from an overall slowing of the reorientation dynamics. This is itself due to a slowing down of the macroscale field-alignment in the bulk domain as the disclination loop diameter approaches a critical value where adjacent defect core regions interact [130]. Following this, the domain rapidly transitions to dynamic regime II-A which occurs rapidly followed by a long time scale regime II-B. For the oblate spheroid case, the dynamic regime I is not observed to have two stages, implying different dynamics of the disclination loop during this regime. Referring back to Figure 5.5, as the disclination loop reduces in size, it forms an elliptic shape which results in the focal segments of the loop having high curvature. These high-energy regions preclude the possibility of adjacent disclination cores approaching each other, and thus dynamic regime I for the oblate spheroid does not involve interaction of adjacent defect core regions of the loop, unlike in the prolate case.

As mentioned in the previous section, the field-off/release dynamics, also shown in Figure 5.9, are inherently different from the field-on dynamics due to the absence of an external field. In particular, the restoring force resulting from the frustration of the field-on nematic texture with respect to the combination of the geometry, surface anchoring conditions, and nematic elasticity is substantially different for the sphere case compared to both the oblate and prolate spheroids in that there is only a very weakly imposed preferred domain director due to the geometry being essentially isometric. Thus the release dynamics for the spheroid involve only a bulk relaxation of the nematic texture. Oblate and prolate spheroids exhibit dynamics qualitatively similar to the field-on case, except in reverse. Analysis of the evolution of the volume-averaged scalar order parameter S_d for the field-off case shown in Figure 5.9 indicates that the dynamics are qualitatively similar, but both prolate and oblate spheroids exhibit only two dynamic regimes where dynamic regimes II-A and II-B

are combined.

Equilibrium values of S_d and the response times for a range of electric field strengths were also determined from simulations, which are of interest for PDLC-based devices and other technological applications. Figure 5.10 shows simulation results of S_d at equilibrium, field-on response times τ_{on}, and field-off response times τ_{off} for oblate, spherical, and prolate spheroids for a range of electric field strengths. Measurements for τ_{on} and τ_{off} were estimated based on the time for S_d to reach steady-state in order to be more comparable to experimental measurements, which are based on changes in optical film transmission [69].

As shown in Figure 5.10, equilibrium S_d values varied significantly depending on both aspect ratio and field strength. Spherical domains, which exhibit the lowest E_c, lack a strongly preferred volume-averaged director, meaning that even relatively weak electric fields are effective for field-aligning the nematic texture. Furthermore, the order parameter S_d increases monotonically with increasing field strength. In contrast, for both oblate and prolate spheroids, S_d is nonmonotonic with respect to electric field strength, initially decreasing for $E < E_c$ and then increasing for $E > E_c$. For the cases where $E < E_c$, oblate and prolate spheroid responses do not involve reorientation of the volume-averaged director. Instead, S_d decreases, corresponding to decreased nematic alignment resulting from geometry and anchoring conditions. For the cases where $E > E_c$, full director reorientation occurs in both prolate and oblate spheroids, but to differing degrees. The critical field strength for the oblate spheroid reorientation is relatively high (10–12 $\text{V}\,\mu\text{m}^{-1}$), due to the large portion of the nematic/solid interface promoting alignment along the intrinsic spheroid director. In contrast, the critical field strength for the prolate spheroid reorientation is relatively low (6–8 $\text{V}\,\mu\text{m}^{-1}$) for the opposite reason. Once reorientation occurs, S_d increases linearly with E as the electric field influence overcomes surface anchoring forces.

The results for field-on response times for both prolate and oblate spheroids are comparable to experimental results for a sphere under similar conditions ($\approx 1\,\text{ms}$) [60]. Both field-on and field-off response times for oblate spheroids are significantly lower, on the order of 0.1 ms, which is due to their negligible change in texture in response to an applied field, as indicated by very little change in S_d between field-on and field-off states. However, simulation results for field-off response times for both prolate spheroids and spheres are somewhat lower than experimental results [60], $\approx 10\,\text{ms}$ versus $\approx 30\,\text{ms}$, respectively. This can be attributed to the significantly larger length scale of nematic spheroids studied experimentally which results in a decreased ratio of restoring to viscous forces, slowing down dynamics.

5.6 Conclusions

In this work continuum simulations were performed in order to predict the dynamic mechanisms involved in the formation, field switching, and relaxation of nematic LC domains with varying spheroidal geometry. The presented simulation results have both fundamental and technological relevance in that formation and field-switching dynamic mechanisms were previously poorly understood and of significant relevance to the performance of PDLC-based optical functional materials. The key feature of these nematic domains is the presence of nanoscale defect structures which contribute to the overall dynamics in complex ways.

Simulations of formation dynamics from an initially unstable isotropic phase predict intrinsically different defect formation mechanisms in anisometric spheroids (oblate and prolate) compared to spherical ones. Defect loop structures, which are topologically imposed by domain geometry and anchoring conditions, are observed to form through the combination of defect shedding and splitting mechanisms. A degeneracy in the splitting of a $+1$ disclination line structure into a $+\frac{1}{2}$ disclination loop is predicted to result in an "unraveling" of the nanoscale loop structure, similar to the nematic elastica behaviour observed in nematic capillaries.

Simulations of electric field-driven reorientation and relaxation dynamics reveal the mechanisms of the reorientation process, which are highly dependent on domain shape and external field strength. Both oblate and prolate spheroids are found to have qualitatively similar dynamic reorientation mechanisms, with the critical (reorientation) electric field strength E_c being significantly higher than for a sphere. For electric fields $E < E_c$, the nematic texture of oblate and prolate spheroids becomes increasingly frustrated between the orientation imposed by the external field and that preferred by the geometry and anchoring conditions. This corresponds to an optical state that is increasingly light scattering. For electric fields $E > E_c$, the nematic texture transitions to a field-aligned state through a series of complex and distinct dynamic mechanisms involving both micron-scale reorientation and nanoscale defect dynamics.

In summary, the presented results provide both qualitative and quantitative insight into the dynamics of nematic spheroids and resolve the nanoscale length and time scales inherent to LC domains which include defects. These simulations include the dynamic regimes relevant to PDLC-based devices and thus could be used to guide the design and optimization of their performance as optical functional materials. Additionally, these results provide fundamental insight into the effects of nanoscale defect dynamics in confined LC domains.

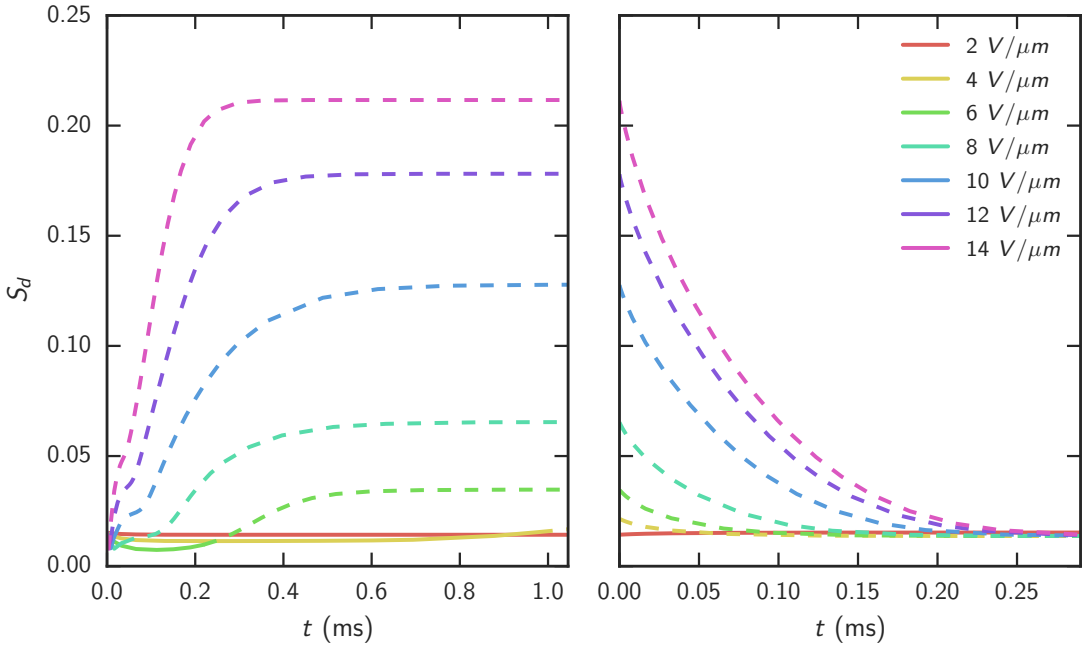
0.25
0.20
0.15
0.10
0.05
0.00
S_d
0.0
0.2
0.4
0.6
0.8
1.0
t (ms)
0.00
0.05
0.10
0.15
0.20
0.25
t (ms)
2 $V/\mu m$
4 $V/\mu m$
6 $V/\mu m$
8 $V/\mu m$
10 $V/\mu m$
12 $V/\mu m$
14 $V/\mu m$

(a)

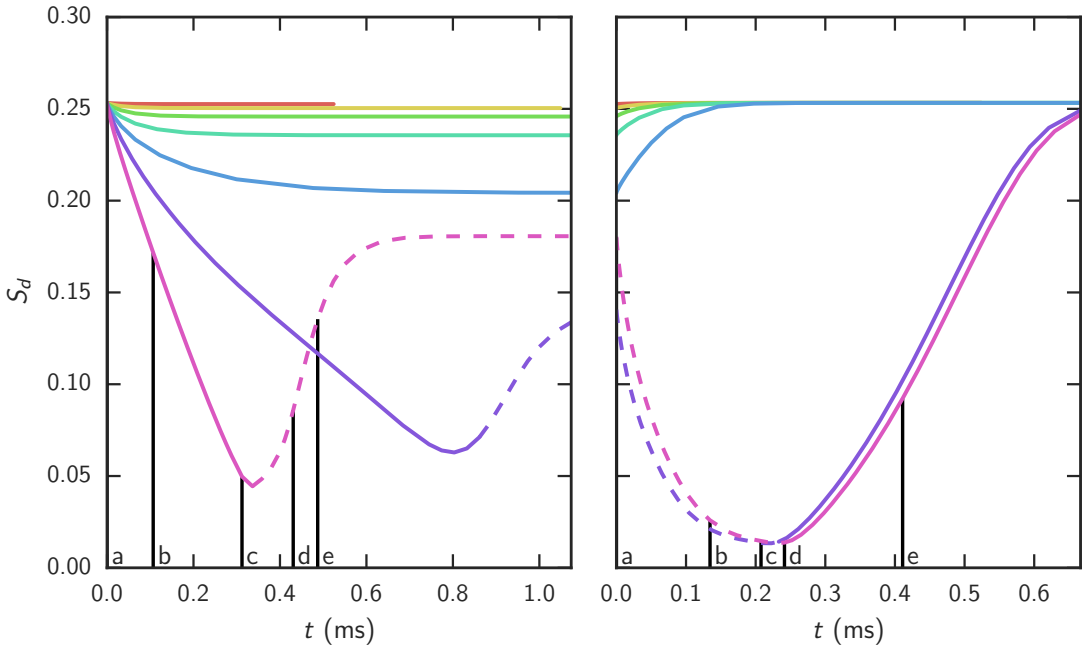
0.30
0.25
0.20
0.15
0.10
0.05
0.00
S_d
a
b
c
d
e
0.0
0.2
0.4
0.6
0.8
1.0
t (ms)
0.0
0.1
0.2
0.3
0.4
0.5
0.6
t (ms)

(b)

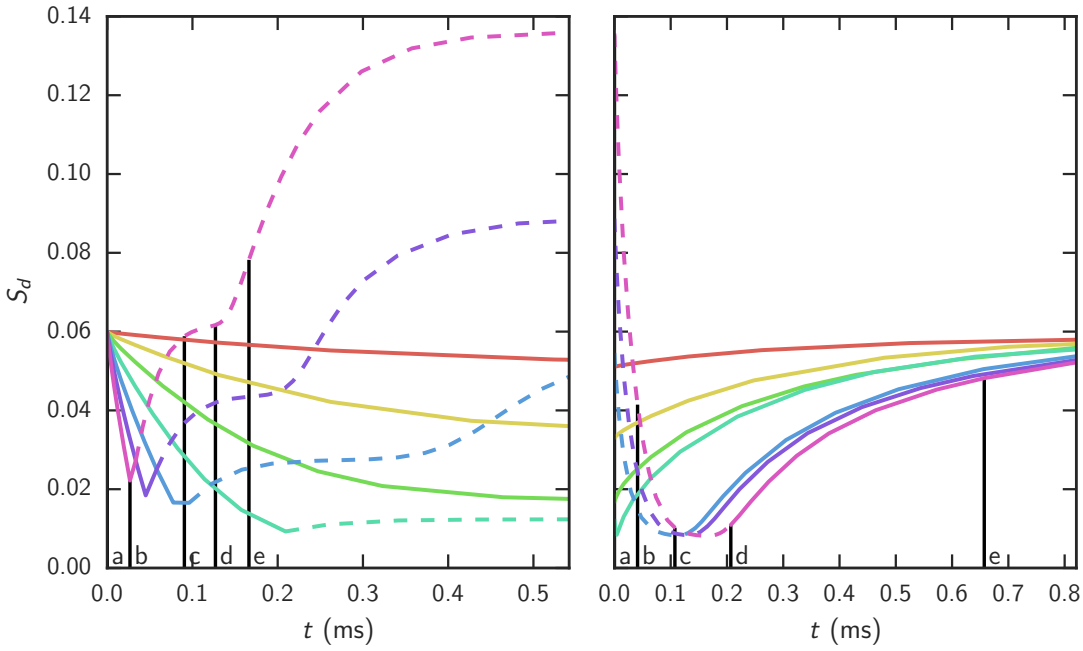

(c)

Figure 5.9: Evolution of droplet scalar order parameter S_d for (a) $R \approx 1$ spherical, (b) $R = 0.5$ oblate (Figures 5.5 and 5.7), and (c) $R = 2$ prolate (Figures 5.6 and 5.8) droplets resulting from application (left column) and release (right column) of electric fields with strengths ranging from $E = 2$–$14\,\mathrm{V\,\mu m^{-1}}$. Curves represent the volume-averaged scalar order parameter S_d with solid/dotted lines corresponding to the volume-averaged director $\mathbf{n}_d$ orthogonal/parallel to the electric field direction. Vertical bars with labels indicate the simulation time at which the corresponding simulation snapshots were taken for the oblate (Figures 5.5 and 5.7) and prolate (Figures 5.6 and 5.8) switching dynamics.

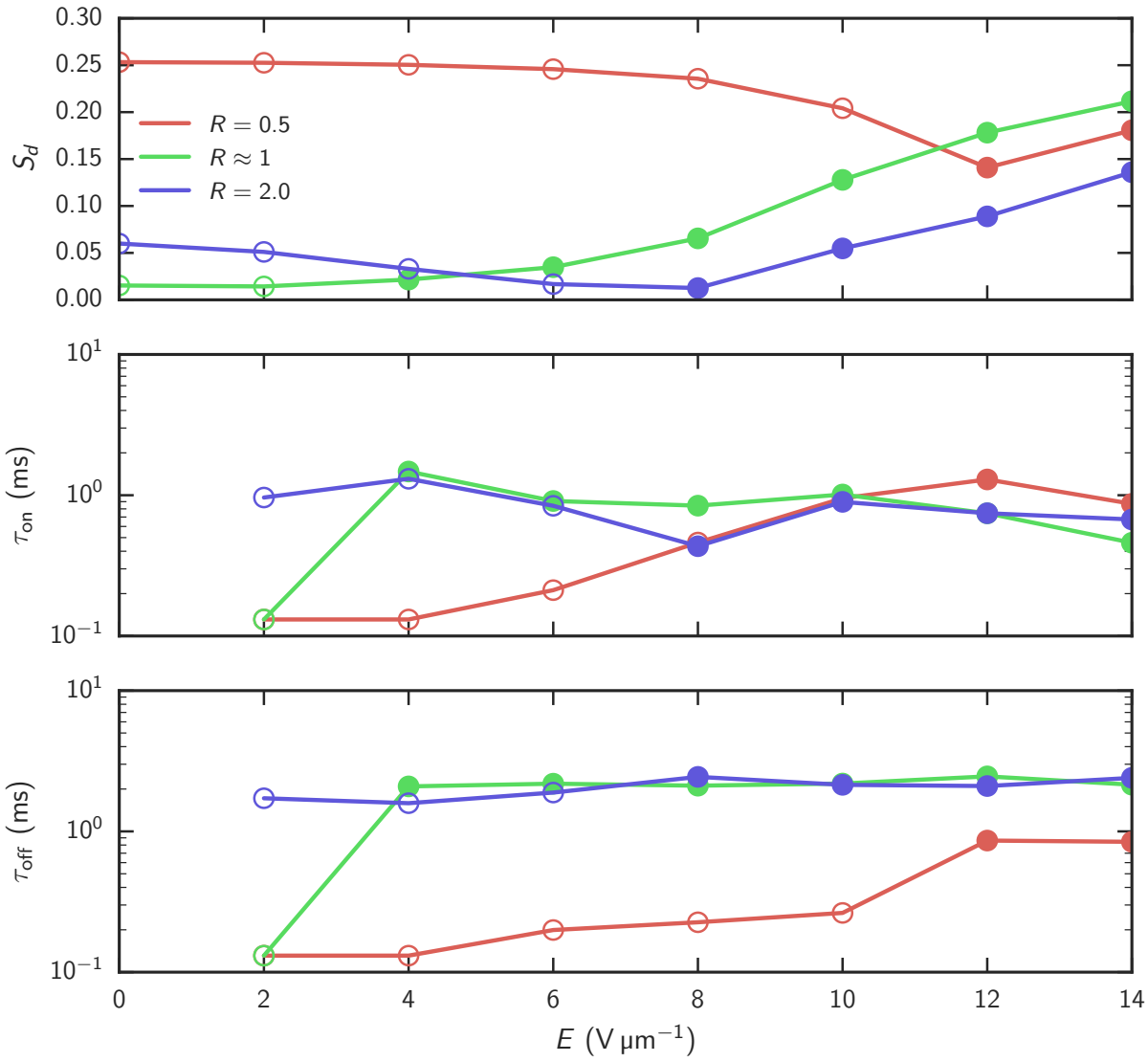

Figure 5.10: (top) Equilibrium droplet scalar order parameter S_d versus electric field strength. (middle) Response times to reach field-driven equilibrium τ_{on} versus electric field strength. (bottom) Response times to reach field-release equilibrium τ_{off} versus electric field strength. Filled points indicate the texture is field-aligned ($\mathbf{n}_d \parallel \mathbf{E}$).

Chapter 6

Chiral Symmetry-breaking Dynamics in the Phase Transformation of Nematic Droplets

6.1 Overview

Chiral symmetry-breaking equilibrium textures in droplets of achiral nematic liquid crystals have long been observed for a broad range of LC compounds and conditions [78, 135–138]. Press and Arrott [77] first predicted equilibrium twisted radial textures in nematic droplets and found them stable for nematic LCs with twist deformations preferred over splay and bend. Since then, the existence of a wide variety of twisted equilibrium textures have been observed both experimentally [135–137] and via simulation [78, 138] for nematic domains with length scales ranging from nanoscale to macroscale. Recently, chiral symmetry breaking in nematics has taken on even more importance due to the discovery of chromonic and bent-core nematic compounds which exhibit previously unobserved nematic elasticity properties [139].

Most of the observed chiral symmetry-breaking phenomena in achiral nematic LCs have involved spherical nematic droplets, which serve as ideal geometries for studying the interplay between surface and bulk elastic effects on nematic texture. Furthermore, the study of nematic droplets is technologically relevant to applications such as biological sensing [140] and polymer-dispersed liquid crystal film-based smart glass [35].

Experimental research on nematic LC domains has been limited to relatively large

length (µm) and time (ms) scales compared to the characteristic scales of nematic LCs (nm, µs). Nematic textures are typically analyzed using polarized optical microscopy or fluorescence confocal polarizing microscopy [14], which has adequate resolution for LC domains of at least a few micrometers in diameter. While deuterium nuclear magnetic resonance [15] and other more advanced imaging methods [141] are able to access dynamics at µm and µs resolutions, it still remains highly nontrivial to study texture dynamics for nanoscopic droplets at relevant time scales. Simulations, which are able to capture complex LC physics [71], can be employed to address these issues.

In this work, continuum simulations are performed of the formation of an initially isotropic phase nematic LC confined within a nanoscale droplet with weak homeotropic surface anchoring conditions. Past research has shown that as the size of a nematic droplet decreases, the equilibrium nematic texture transitions from a radial configuration with a $+\frac{1}{2}$ disclination loop to a defect-free uniform texture [9]. This transition results from the competition between the bulk elasticity and surface anchoring effects. The simulations presented here are performed within the droplet size and surface anchoring strength regime where the uniform texture is stable. Beginning at the initial quench, nematic formation occurs, initially forming an unstable radial-like texture. Subsequently, a spontaneous symmetry-breaking twist-mediated defect escape mechanism is observed for material parameters corresponding to pentyl-cyanobiphenyl (5CB) prior to the droplet evolving to the equilibrium uniform texture. Notably, this dynamic mechanism does not occur under the single-constant approximation frequently used in LC simulations. In such an approximation, physically realistic differences between the modes of elastic deformation are neglected and the elastic free energy is parameterized by a single elastic constant.

6.2 Methodology

The overall model for this study is very similar to the one used in Chapter 5. The Landau–de Gennes model was used, although electric field-switching was not considered in this work ($\mathbf{E} = \mathbf{0}$), and its model parameters were derived from experimental estimates corresponding to 5CB. The two exceptions to this were that (i) the value for k_{24} was revised to be more consistent with recent experimental results which show $k_{24} = k_{22}$ [126, 142], and (ii) the surface anchoring energy strength was decreased to $\alpha = 10^{-5}\,\mathrm{J/m^2}$ to promote escape of the expected defect loop. Using the relations between the Frank-Oseen and Landau–de Gennes elastic constants from Equations 3.8–3.11 and assuming $S = S_{eq} \approx 0.31$, the newly computed constants were: $L_1 = 9.1\,\mathrm{pN}$, $L_2 = -8.1\,\mathrm{pN}$, $L_3 = 7.1\,\mathrm{pN}$, and $L_{24} = 16.6\,\mathrm{pN}$.

Homeotropic surface anchoring was modelled using a quadratic surface free energy density:

$$f_s = \frac{1}{2}\alpha(Q_{ij} - Q_0)^2 \tag{6.1}$$

where $Q_0 = S_{eq}(k_i k_j - \frac{1}{3}\delta_{ij})$. This model was chosen because it allows for the anchoring strength α to deviate more as f_s has a minimum at $S = S_{eq}$ regardless of the value of α. In contrast, in the previous linear model, as α increases, the minimization can result in $S > 1$ at the surface, which is unphysical. Given that the value of the surface anchoring strength is critical for observing the symmetry-breaking phenomenon, the model was changed in order to allow for broader study of the impact of α in future work. However, it should be emphasized that the observed phenomenon was observed regardless of the choice of the surface anchoring model for the parameters used in this work.

The droplet geometry used was a slightly oblate spheroid, equivalent to a sphere being compressed by 2% of its diameter along the z-axis. This oblateness results in a small preference for alignment along the z direction which eliminates a possible degeneracy in overall droplet alignment that arises from a perfectly spherical shape. This degeneracy could result in a saddle point in the free energy leading to anomalous dynamics [89].

Simulations were performed using both 5CB elasticity parameters and the single elastic constant approximation in which $L_1 > 0$ and $L_2 = L_3 = L_{24} = 0$.

6.3 Results and Discussion

Figure 6.1 shows visualizations of the time evolution of the alignment tensor field $\boldsymbol{Q}$ for both elasticity cases, showing nematic phase formation into a radial nematic texture followed by relaxation to a uniform texture via disclination motion and escape.

For both cases, the initial formation dynamics (Figure 6.1a–d) observed are consistent with past dynamic simulation results (Chapter 5), in which the stable nematic phase initially grows freely into the centre of the domain but eventually slows due to capillary effects and forms a $+\frac{1}{2}$ disclination loop. The resulting fully-formed nematic domain has a radial nematic texture (Figure 6.1d) due to topological constraints imposed through the combination of homeotropic anchoring and spherical confinement. However, the competition between surface anchoring and bulk elasticity results in this radial texture being unstable, causing relaxation of the nematic domain to continue toward a uniform defect-free texture (Figure 6.1m), which is expected for cases of small nanoscale droplets [9].

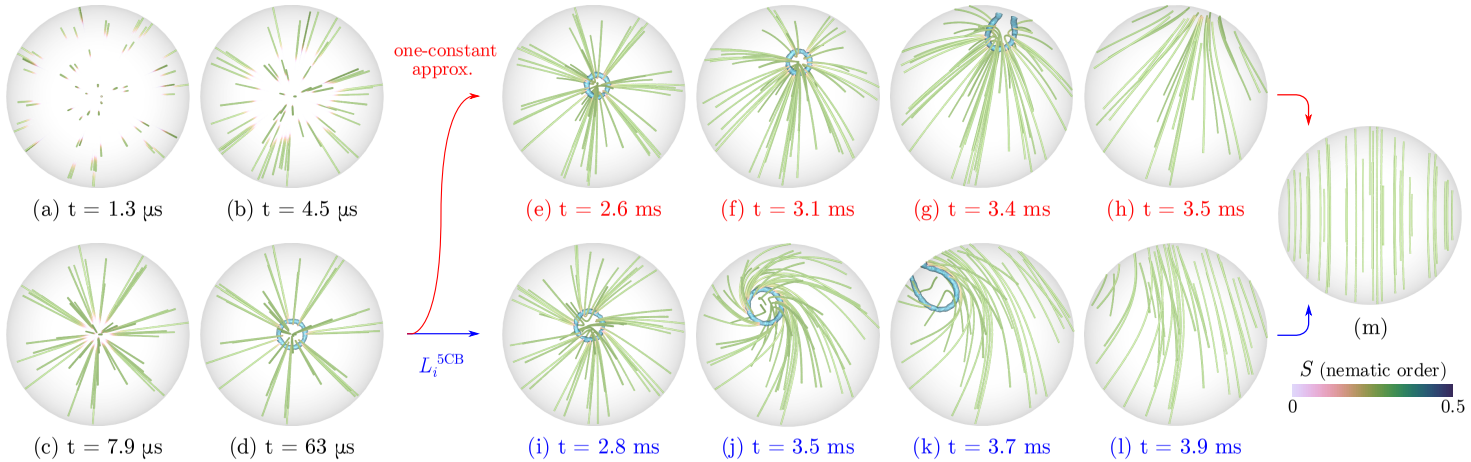

Figure 6.1: Hyperstreamline visualizations of the evolution of the alignment tensor field for a droplet of $R = 375\,\text{nm}$: (a–d) Nematic phase formation (qualitatively identical for both elasticity cases), (e–h) defect loop escape (one-constant elasticity), (i–l) defect loop escape (5CB elasticity), and (m) the equilibrium uniform texture domain. For (a–l) the z-axis is oriented out-of-plane and for (m) it is reoriented in-plane vertical (for clarity).

The relaxation mechanism for the single elastic constant approximation simulation, shown in Figures 6.1e–h, is significantly different compared to that for the 5CB elasticity case, shown in Figures 6.1i–l. For the single elastic constant case, the relaxation process occurs in an intuitive way, through simultaneous defect loop motion towards the domain boundary and bulk texture relaxation. As the defect loop approaches the boundary, the local anchoring deviates significantly from homeotropic alignment and the defect loop "escapes" through the boundary. However, for the 5CB elasticity case, as the defect loop translates toward the boundary, the alignment in the surrounding region also rotates about the axis orthogonal to the plane of the loop. In this way, defect motion is accompanied by a simultaneous twist deformation in the bulk texture. As the defect loop escapes the boundary through local relaxation of the homeotropic anchoring, the bulk nematic texture eventually unravels into a uniform state. Qualitatively, this mechanism results in decreased splay deformation compared to the single-constant case, at the expense of increased twist deformation.

In order to analyze these dynamic processes quantitatively, it is useful to approximate the individual contributions to the tensorial elastic free energy density (Equation 3.7) with respect to the different canonical modes of nematic deformation from the Frank-Oseen model (Equation 3.1). In order to estimate these contributions from the tensorial LdG form of nematic elasticity, the *uniaxial* component of $\mathbf{Q}$ was first calculated for each simulation (i.e., $\mathbf{Q}_{uni} = S(\mathbf{nn} - \frac{1}{3}\boldsymbol{\delta})$, in which $P = 0$). The derived relations between L_i and k_i (Equations 3.8–3.11) [84] were then substituted into Equation 3.7 such that f_{el} is parameterized in terms of k_i:

$$f_{el} = \frac{1}{2S^2}k_{11}\left(-\frac{1}{6}G_1 + G_2 - \frac{1}{2S}G_3\right) + \frac{1}{2S^2}k_{22}\left(\frac{1}{2}G_1 - G_{24}\right) + \frac{1}{2S^2}k_{33}\left(\frac{1}{6}G_1 + \frac{1}{2S}G_3\right) - \frac{1}{2S^2}(k_{22} + k_{24})(G_2 - G_{24}) \tag{6.2}$$

where the energy contributions associated with the different modes of deformation are grouped analogously to Equation 3.1. G_i correspond to the gradient terms in f_{el} as shown in the following:

$$\begin{aligned} f_{el} =& \frac{1}{2}L_1(\partial_i Q_{jk}\partial_i Q_{kj}) + \frac{1}{2}L_2(\partial_i Q_{ij}\partial_k Q_{kj}) + \frac{1}{2}L_3(Q_{ij}\partial_i Q_{kl}\partial_j Q_{kl}) + \frac{1}{2}L_{24}(\partial_k Q_{ij}\partial_j Q_{ik}) \\ =& \frac{1}{2}L_1G_1 + \frac{1}{2}L_2G_2 + \frac{1}{2}L_3G_3 + \frac{1}{2}L_{24}G_{24} \end{aligned} \tag{6.3}$$

Figure 6.2 shows the evolution of these free energy contributions for both cases of elasticity being studied. During the nematic formation process, the elastic contributions to

the free energy are similar for both cases, in that they are governed by the stable nematic surface layer where surface anchoring promotes a radially-oriented nematic "shell" enclosing an unstable isotropic "core". Following nematic formation, their deformation modes predominantly involve high splay deformation, as expected for a radial-like texture. For the single-constant case (Figure 6.2a), the subsequent radial-to-uniform relaxation process involves a monotonic decrease in the splay deformation contribution until the elasticity vanishes entirely, at which point the domain is uniform. However, during the radial-to-uniform relaxation process for the 5CB elasticity case (Figure 6.2b), the splay deformation component decreases more slowly in comparison and is offset by a lesser (energetic) increase in the twist deformation contribution. This increase in the twist deformation contribution coincides with the twisting relaxation process, which is then followed by a decrease in all elastic contributions as the defect loop escapes. Intuitively, this result reflects the fact that the twist elastic constant is lower than both splay and bend for 5CB. Thus, for the case of 5CB elasticity, the splay-dominated relaxation mechanism observed in the single-constant case is a higher-energy dynamic pathway to equilibrium compared to the chiral symmetry-breaking twist mechanism. This interpretation is synonymous with that for equilibrium twisted-radial droplet textures where the magnitude of the twist angle in the texture was dependent on the ratio of twist to splay elastic constants [77].

Additional simulations for nematic droplets with radii ranging from $R = 250$–$750\,\mathrm{nm}$ were then performed using the 5CB elasticity parameters, all within a scale and parameter range where the uniform texture is stable. In all simulations the twist relaxation mechanism was observed and the time scales of the relaxation, which correspond to the region of nonzero twist deformation, were measured (Figure 6.3). For larger radii (e.g., comparable to those accessible via polarized optical microscopy), it is expected that the radial texture resulting from the nematic formation process would be stable due to the eventual dominance of the surface anchoring energy over the bulk elasticity with increasing droplet size [9, 78], and thus the twist relaxation mechanism would no longer occur.

6.4 Conclusions

In conclusion, continuum simulations of the phase transformation of achiral nematic droplets with weak homeotropic anchoring were found to predict a chiral symmetry-breaking dynamic mechanism in the relaxation of the droplet to a stable uniform texture. Additionally, it was found that the use of full anisotropy in nematic elasticity, corresponding to 5CB in the present simulations, is required to observe the twisting relaxation mechanism. In this case, as is true with the class of LC-exhibiting cyanobiphenyl compounds [75], twist deformations are

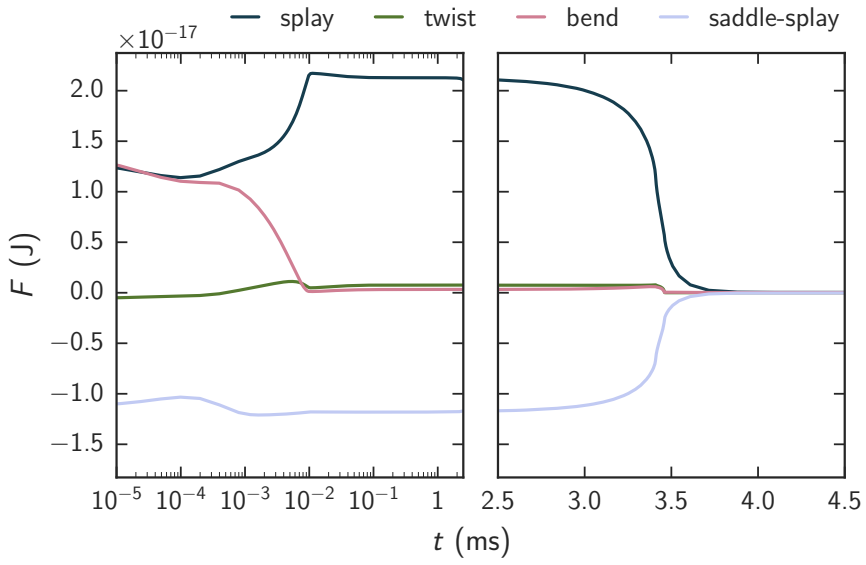

(a)

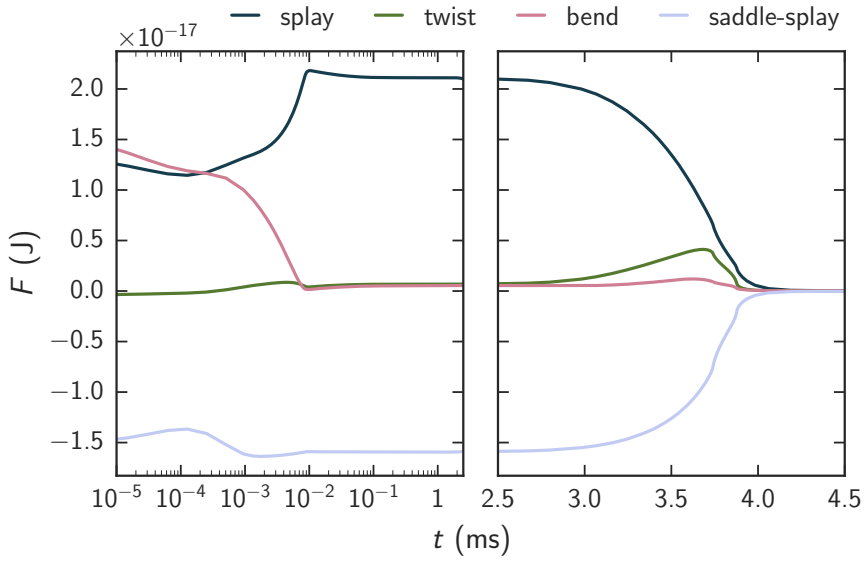

(b)

Figure 6.2: Evolution of the approximate elastic free energy contributions of splay, twist, bend, and saddle-splay deformation modes for the (a) single-constant and (b) 5CB elasticity cases.

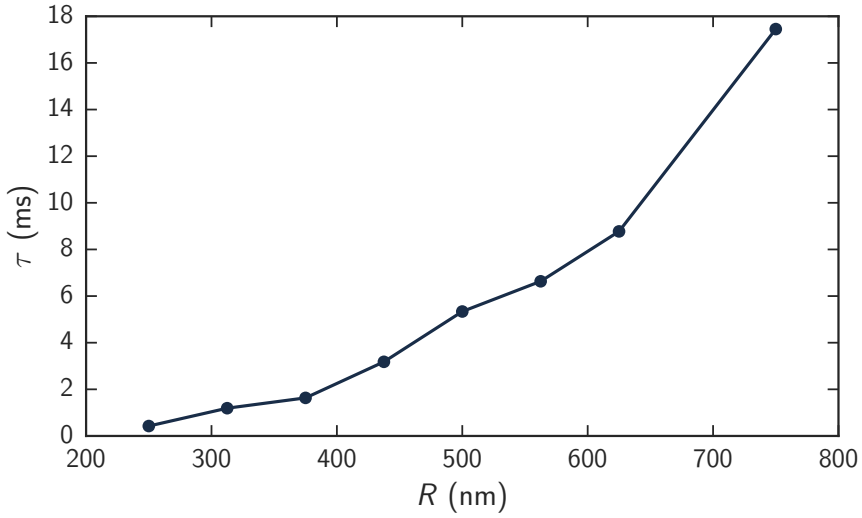

Figure 6.3: Time scale of the twist relaxation mechanism from radial to uniform nematic texture for the 5CB elasticity case versus droplet radius R, measured from the end of the formation process until the escape of the defect loop.

energetically favourable compared to splay and bend. However, a more complex relationship between the nematic elastic constants governing this dynamic mechanism could exist as was found in ref. [78] for equilibrium textures. Finally, the frequently used single-constant elasticity approximation, in which splay, twist, and bend elasticity parameters are assumed equal, is insufficient to predict this relaxation mechanism.

Chapter 7

Conclusions and Recommendations

7.1 Conclusions

In this work, a continuum simulation method using the Landau-de Gennes model was developed and applied to the study of phase formation and field-switching dynamics of nematic liquid crystal droplets. Through the use of continuum theory, the simulation method is able to access length and time scales which are challenging to capture experimentally. Common model simplifications used in past studies were avoided in this work including the use of: the single elastic constant approximation, "strong" surface anchoring conditions, and the use of geometric symmetry.

Application of the model to the study of the effect of shape (aspect ratio) for nematic elliptic capillaries and spheroidal droplets has resulted in the following conclusions:

- Domain shape, while maintaining constant area/volume, has a large impact on the degree of overall alignment of the nematic droplet. The mechanism via which this occurs is due to the varying curvature present within elliptic and ellipsoidal geometries. This is found to affect the formation and motion of defects and result in domains with greater alignment compared to circular/spherical-shaped domains.

- Application of electric fields below a critical field strength results in a frustrated domain texture in which the overall alignment within the droplet is lowered. However, above this critical field strength, the droplet texture reorients into a field-aligned state and the overall alignment can increase past its original value depending on

the competition between the electric field and surface anchoring strength. This observation is not present for circular and spherical domains, in which alignment increases monotonically due to the lack of a preferred alignment in the field-off state.

- Droplet shape results in significant changes in response times for field switching, based upon simulation predictions.

Finally, a novel dynamic symmetry-breaking phase transformation process was observed for the case of nematic phase formation within a spherical droplet. This result reinforces that even relatively minor differences in the elastic moduli for a liquid crystal can result in consequential effects to dynamic pathways, even if the changes do not significantly affect the equilibrium solutions.

7.2 Recommendations

While the simulation method stands as a significant improvement compared to simplified models used for past nematic droplet studies, several key enhancements would improve its capability including modeling hydrodynamics and thermal fluctuations [143]. Hydrodynamics, while not considered significant in this work given that the small domain shape constraints LC flow, would be of interest for domains under high electric field strength in which field-driven reorientation can induce flow effects. Incorporating thermal fluctuations may be relevant to nematic formation, allowing for spontaneous nucleation of nematic domains within the isotropic phase [143]. Accounting for these effects would be quite challenging but would be a worthwhile area of study in terms of model development. One relatively simple yet significant change would be incorporating degenerate planar surface anchoring conditions [17], which is necessary for modelling certain LC/polymer interfaces [18].

Next, studies could be conducted that better approximate droplet switching in the context of PDLC device technology. As noted in Chapters 4 and 5, field-switching simulations were conducted with the goal of observing maximum reorientation, i.e. the electric field was always applied along the major axis of the spheroids and not along the minor axis. In a typical PDLC film however, it would be more common for the electric field direction to be normal to the surface of the film, which would typically be the minor axis direction. This was done in order to focus on the more fundamental physics of nematic texture reorientation. While applying the electric field in the minor axis direction would result in fairly predictable equilibrium textures, such simulations would arguably have greater relevance to PDLC devices. Furthermore, metrics such as critical voltages and characteristic switching times could be very useful for the design of PDLC films.

Along the same lines, additional analysis could be performed that considers the effect of multiple droplets. For example, Kelly and Palffy-Muhoray [33] introduce an additional order parameter metric called the *sample order parameter* which considers the spatial orientation of the droplets themselves.

Finally, computational optics-based analyses would greatly complement this work. Most experimental work in the field still relies on POM for the determination of droplet texture, and it is relatively simple to simulate basic birefringence patterns from simulated director fields [144]. Furthermore, methods to compute transparency in the context of the polymer substrate (instead of placing all the focus on alignment of the LC droplet) would be beneficial for PDLC device optimization.

References

[1] P. J. Collings and M. Hird. *Introduction to Liquid Crystals: Chemistry and Physics*. Taylor & Francis, 1997.

[2] D. S. Miller and N. L. Abbott. Influence of droplet size, pH and ionic strength on endotoxin-triggered ordering transitions in liquid crystalline droplets. *Soft Matter*, 9(2):374–382, 2013.

[3] F. Bloisi and L. R. M. Vicari. *Polymer Dispersed LCDs*, pages 1565–1585. Springer Berlin Heidelberg, Berlin, Heidelberg, 2012.

[4] N. H. Park, S. C. Noh, P. Nayek, M.-H. Lee, M. S. Kim, L.-C. Chien, J. H. Lee, B. K. Kim, and S. H. Lee. Optically isotropic liquid crystal mixtures and their application to high-performance liquid crystal devices. *Liquid Crystals*, 42(4):530–536, 2015.

[5] T. J. Bunning, L. V. Natarajan, V. P. Tondiglia, and R. Sutherland. Holographic polymer-dispersed liquid crystals (H-PDLCs). *Annual Review of Materials Science*, 30(1):83–115, 2000.

[6] P. S. Drzaic. Reorientation dynamics of polymer dispersed nematic liquid crystal films. *Liquid Crystals*, 3(11):1543–1559, 1988.

[7] P. S. Drzaic. Putting liquid crystal droplets to work: a short history of polymer dispersed liquid crystals. *Liquid Crystals*, 33(11-12):1281–1296, 2006.

[8] T. Lopez-Leon and A. Fernandez-Nieves. Drops and shells of liquid crystal. *Colloid and Polymer Science*, 289(4):345–359, 2011.

[9] O. D. Lavrentovich. Topological defects in dispersed liquid crystals, or words and worlds around liquid crystal drops. *Liquid Crystals*, 24(1):117–125, 1998.

[10] R. H. Chen. *Liquid crystal displays*. Wiley, 2011.

[11] D. Frenkel. Order through disorder: Entropy-driven phase transitions. In L. Garrido, editor, *Complex Fluids*, volume 415 of *Lecture Notes in Physics*, pages 137–148. Springer Berlin / Heidelberg, 1993.

[12] N. J. Mottram and C. J. P. Newton. Introduction to Q-tensor theory. 2014.

[13] L. A. Madsen, T. J. Dingemans, M. Nakata, and E. T. Samulski. Thermotropic biaxial nematic liquid crystals. *Physical Review Letters*, 92(14):145505, 2004.

[14] O. D. Lavrentovich. Defects in Liquid Crystals: Surface and Interfacial Anchoring Effects. In O. D. Lavrentovich, P. Pasini, C. Zannoni, and S. Žumer, editors, *Patterns of Symmetry Breaking*, volume 52, pages 161–195. Springer Netherlands, Dordrecht, 2003.

[15] G. Crawford, D. Allender, and J. Doane. Surface elastic and molecular-anchoring properties of nematic liquid crystals confined to cylindrical cavities. *Physical Review A*, 45(12):8693–8708, 1992.

[16] Dissemination of IT for the Promotion of Materials Science. Liquid crystals. https://www.doitpoms.ac.uk/tlplib/liquid_crystals/, 2007. Accessed: July 17, 2017. Licensed under CC BY-NC-SA 2.0 UK.

[17] J.-B. Fournier and P. Galatola. Modeling planar degenerate wetting and anchoring in nematic liquid crystals. *Europhysics Letters*, 72(3):403–409, 2006.

[18] H.-S. Kitzerow. Polymer-dispersed liquid crystals: From the nematic curvilinear aligned phase to ferroelectric films. *Liquid Crystals*, 16(1):1–31, 1994.

[19] O. O. Prischepa, A. V. Shabanov, and V. Y. Zyryanov. Director configurations within nematic droplets doped by lecithin. *Molecular Crystals and Liquid Crystals*, 438(1):141–150, 2005.

[20] S. J. Woltman, G. D. Jay, and G. P. Crawford. Liquid-crystal materials find a new order in biomedical applications. *Nature materials*, 6(12):929–938, 2007.

[21] N. Schopohl and T. Sluckin. Defect core structure in nematic liquid crystals. *Physical Review Letters*, 59(22):2582–2584, 1987.

[22] G. P. Alexander, B. G. Chen, E. A. Matsumoto, and R. D. Kamien. Colloquium: Disclination loops, point defects, and all that in nematic liquid crystals. *Reviews of Modern Physics*, 84(2):497–514, 2012.

[23] Y.-K. Kim, S. V. Shiyanovskii, and O. D. Lavrentovich. Morphogenesis of defects and tactoids during isotropicnematic phase transition in self-assembled lyotropic chromonic liquid crystals. *Journal of Physics: Condensed Matter*, 25(40):404202, 2013.

[24] G. P. Crawford, R. D. Polak, A. Scharkowski, L. C. Chien, J. W. Doane, and S. Zumer. Nematic director-fields captured in polymer networks confined to spherical droplets. *Journal of Applied Physics*, 75(4):1968–1971, 1994.

[25] D. Allender, G. Crawford, and J. Doane. Determination of the liquid-crystal surface elastic constant K_{24}. *Physical Review Letters*, 67(11):1442–1445, 1991.

[26] E. Castellón, M. Zayat, and D. Levy. Molecular configuration transitions of a nematic liquid crystal encapsulated in organically modified silicas. *Physical Chemistry Chemical Physics*, 11(29):6234–41, 2009.

[27] A. Sonnet, A. Kilian, and S. Hess. Alignment tensor versus director: Description of defects in nematic liquid crystals. *Physical Review E*, 52(1):718–722, 1995.

[28] O. O. Prishchepa, V. Y. Zyryanov, A. P. Gardymova, and V. F. Shabanov. Optical textures and orientational structures of nematic and cholesteric droplets with heterogeneous boundary conditions. *Molecular Crystals and Liquid Crystals*, 489(1):84–89, 2008.

[29] A. Tiribocchi, O. Henrich, J. S. Lintuvuori, and D. Marenduzzo. Switching hydrodynamics in liquid crystal devices: a simulation perspective. *Soft Matter*, 10(26):4580–92, 2014.

[30] M. G. Campbell, M. Tasinkevych, and I. I. Smalyukh. Topological polymer dispersed liquid crystals with bulk nematic defect lines pinned to handlebody surfaces. *Physical Review Letters*, 112(19):197801, 2014.

[31] L. Bouteiller and P. LeBarny. Polymer-dispersed liquid crystals: Preparation, operation and application. *Liquid Crystals*, 21(2):157–174, 1996.

[32] R. K. Bharadwaj, T. J. Bunning, and B. L. Farmer. A mesoscale modelling study of nematic liquid crystals confined to ellipsoidal domains. *Liquid Crystals*, 27(5):591–603, 2000.

[33] J. R. Kelly and P. Palffy-Muhoray. The optical response of polymer dispersed liquid crystals. *Molecular Crystals and Liquid Crystals*, 243(1):11–29, 1994.

[34] F. Fu and N. M. Abukhdeir. Formation and field-driven dynamics of nematic spheroids. *Soft Matter*, 13(28):4890–4902, 2017.

[35] P. S. Drzaic. *Liquid Crystal Dispersions*, volume 1 of *Liquid Crystals Series*. World Scientific, 1995.

[36] C. M. Lampert. Large-area smart glass and integrated photovoltaics. *Solar Energy Materials and Solar Cells*, 76(4):489–499, 2003.

[37] J. W. Doane, B. Wu, and J. H. Erdmann. PDLC shutters: where has this technology gone? *Liquid Crystals*, 33(11-12):1313–1322, 2006.

[38] K. V. Wong and R. Chan. Smart glass and its potential in energy savings. *Journal of Energy Resources Technology*, 136(1):012002, 2013.

[39] G. P. Crawford. Ordering and ordering transitions in confined liquid crystals. *Modern Physics Letters B*, 1993.

[40] P. K. Chan. Computer simulation of elongated bipolar nematic droplets I. External field aligned parallel to the droplet axis of symmetry. *Liquid Crystals*, 26(12):1777–1786, 1999.

[41] P. K. Chan. Computer simulation of elongated bipolar nematic droplets II. External field aligned normal to the droplet axis of symmetry. *Liquid Crystals*, 28(2):207–215, 2001.

[42] S. Candau, P. Le Roy, and F. Debeauvais. Magnetic field effects in nematic and cholesteric droplets suspended in a isotropic liquid. *Molecular Crystals and Liquid Crystals*, 23(3-4):283–297, 1973.

[43] H. Mori and H. Nakanishi. On the stability of topologically non-trivial point defects. *Journal of the Physical Society of Japan*, 57(4):1281–1286, 1988.

[44] E. M. Terentjev. Disclination loops, standing alone and around solid particles, in nematic liquid crystals. *Physical Review E*, 51(2):1330–1337, 1995.

[45] E. Penzenstadler and H.-R. Trebin. Fine structure of point defects and soliton decay in nematic liquid crystals. *Journal de Physique*, 50(9):1027–1040, 1989.

[46] E. Gartland and S. Mkaddem. Instability of radial hedgehog configurations in nematic liquid crystals under Landau-de Gennes free-energy models. *Physical Review E*, 59(1):563–567, 1999.

[47] S. Kralj and E. G. Virga. Universal fine structure of nematic hedgehogs. *Journal of Physics A: Mathematical and General*, 34(4):829–838, 2001.

[48] S. Mkaddem and E. Gartland. Fine structure of defects in radial nematic droplets. *Physical Review E*, 62(5):6694–6705, 2000.

[49] M. Kanke and K. Sasaki. Equilibrium configuration in a nematic liquid crystal droplet with homeotropic anchoring of finite strength. *Journal of the Physical Society of Japan*, 82(9):094605, 2013.

[50] A. Golemme, S. Zumer, J. W. Doane, and M. E. Neubert. Deuterium NMR of polymer dispersed liquid crystals. *Physical Review A*, 37(2):559–569, 1988.

[51] O. D. Lavrentovich and V. M. Pergamenshchik. Patterns in thin liquid crystal films and the divergence ("surfacelike") elasticity. *International Journal of Modern Physics B*, 9(18 & 19):2389–2437, 1995.

[52] V. Tomar, S. I. Hernández, N. L. Abbott, J. P. Hernández-Ortiz, and J. J. de Pablo. Morphological transitions in liquid crystal nanodroplets. *Soft Matter*, 8(33):8679, 2012.

[53] J. H. Erdmann, S. Zumer, and J. W. Doane. Configuration transition in a nematic liquid crystal confined to a small spherical cavity. *Physical Review Letters*, 64(16):1907–1910, 1990.

[54] S. Kralj and S. Zumer. Fréedericksz transitions in supra-μm nematic droplets. *Physical Review A*, 45(4):2461–2470, 1992.

[55] V. G. Bodnar, A. V. Koval'chuk, O. D. Lavrentovich, V. M. Pergamenshchik, and V. V. Sergan. Threshold of structural transition in nematic drops with normal boundary conditions in AC electric field. *SPIE*, 1455:61–72, 1991.

[56] V. Bodnar, O. Lavrentovich, and V. Pergamenshchik. Threshold of structural hedgehog-ring transition in drops of a nematic in an alternating electric field. *Soviet Physics JETP*, 74(1):60–67, 1992.

[57] J. Ding, H. Zhang, and J. Lu. Restructuring of polymer-dispersed nematic droplets in external electric field. *Japanese Journal of Applied Physics*, 34(4R):1928–1934, 1995.

[58] E. M. De Groot and G. G. Fuller. Electric field studies of liquid crystal droplet suspensions. *Liquid Crystals*, 23(1):113–126, 1997.

[59] J. W. Doane, A. Golemme, J. L. West, J. B. Whitehead, and B.-G. Wu. Polymer dispersed liquid crystals for display application. *Molecular Crystals and Liquid Crystals*, 165(1):511–532, 1988.

[60] A. Xie and D. A. Higgins. Electric-field-induced dynamics in radial liquid crystal droplets studied by multiphoton-excited fluorescence microscopy. *Applied Physics Letters*, 84(20):4014, 2004.

[61] S. Komura, R. J. Atkin, M. S. Stern, and D. A. Dunmur. Numerical analysis of the radial-axial structure transition with an applied field in a nematic droplet. *Liquid Crystals*, 23(2):193–203, 1997.

[62] A. Kilian. Computer simulations of nematic droplets. *Liquid Crystals*, 14(4):1189–1198, 1993.

[63] W.-Y. Li and S.-H. Chen. Simulation of normal anchoring nematic droplets under electrical fields. *Japanese Journal of Applied Physics*, 38(3A):1482–1487, 1999.

[64] P. Prinsen and P. van der Schoot. Shape and director-field transformation of tactoids. *Physical Review E*, 68(2):21701, 2003.

[65] O. A. Aphonin, Y. V. Panina, A. B. Pravdin, and D. A. Yakovlev. Optical properties of stretched polymer dispersed liquid crystal films. *Liquid Crystals*, 15(3):395–407, 1993.

[66] S. J. Klosowicz, M. Aleksander, and P. Obrzut. PDLC composites with elongated LC droplets. In *SPIE*, volume 5947, pages 59470M–1, 2005.

[67] I. Amimori, N. V. Priezjev, R. A. Pelcovits, and G. P. Crawford. Optomechanical properties of stretched polymer dispersed liquid crystal films for scattering polarizer applications. *Journal of Applied Physics*, 93(6):3248–3252, 2003.

[68] I. Amimori, J. Eakin, J. Qi, G. Skačej, S. Žumer, and G. Crawford. Surface-induced orientational order in stretched nanoscale-sized polymer dispersed liquid-crystal droplets. *Physical Review E*, 71(3):031702, 2005.

[69] J. Erdmann, J. W. Doane, S. Zumer, and G. Chidichimo. Electrooptic response of PDLC light shutters. In *SPIE*, volume 32, pages 32–40, 1989.

[70] V. Y. Rudyak, A. V. Emelyanenko, and V. A. Loiko. Structure transitions in oblate nematic droplets. *Physical Review E*, 88(5):052501, 2013.

[71] N. M. Abukhdeir. Computational characterization of ordered nanostructured surfaces. *Materials Research Express*, 3(8):082001, 2016.

[72] M. Kanke and K. Sasaki. Numerical study of a disclination loop in a nematic liquid crystal droplet. *Journal of the Physical Society of Japan*, 82(3):034601, 2013.

[73] P. K. Chan and A. D. Rey. Simulation of reorientation dynamics in bipolar nematic droplets. *Liquid Crystals*, 23(5):677–688, 1997.

[74] M. Ravnik and S. Žumer. Landau–de Gennes modelling of nematic liquid crystal colloids. *Liquid Crystals*, 36(10-11):1201–1214, 2009.

[75] N. V. Madhusudana and R. Pratibha. Elasticity and orientational order in some cyanobiphenyls: Part IV. reanalysis of the data. *Molecular Crystals and Liquid Crystals*, 89:249–257, 1982.

[76] B. Wincure and A. D. Rey. Interfacial nematodynamics of heterogeneous curved isotropic-nematic moving fronts. *The Journal of Chemical Physics*, 124(24):244902, 2006.

[77] M. J. Press and A. S. Arrott. Theory and experiments on configurations with cylindrical symmetry in liquid-crystal droplets. *Physical Review Letters*, 33(7):403–406, 1974.

[78] R. D. Williams. Two transitions in tangentially anchored nematic droplets. *Journal of Physics A: Mathematical and General*, 19(16):3211–3222, 1986.

[79] F. C. Frank. I. Liquid crystals. On the theory of liquid crystals. *Discussions of the Faraday Society*, 25(I):19, 1958.

[80] M. Kleman and O. D. Lavrentovich. *Soft Matter Physics: An Introduction*. Springer, New York, 2003.

[81] P. G. de Gennes and J. Prost. *The Physics of Liquid Crystals*. Oxford University Press, New York, 2 edition, 1995.

[82] S. Žumer and S. Kralj. Influence of K 24 on the structure of nematic liquid crystal droplets. *Liquid Crystals*, 12(4):613–624, 1992.

[83] Ž. Kos and M. Ravnik. Relevance of saddle-splay elasticity in complex nematic geometries. *Soft Matter*, 2016.

[84] H. Mori, E. C. Gartland, J. R. Kelly, and P. J. Bos. Multidimensional director modeling using the Q tensor representation in a liquid crystal cell and its application to the it cell with patterned electrodes. *Japanese Journal of Applied Physics*, 38(1):135–146, 1999.

[85] E. Lueder. *Liquid Crystal Displays: Addressing Schemes and Electro-Optical Effects*. Wiley, 2010.

[86] J. L. Ericksen. Inequalities in liquid crystal theory. *Physics of Fluids*, 9(6):1205, 1966.

[87] A. Majumdar. Equilibrium order parameters of nematic liquid crystals in the Landau-de Gennes theory. *European Journal of Applied Mathematics*, 21(02):181, 2010.

[88] N. J. Mottram and C. J. P. Newton. Liquid Crystal Theory and Modelling. In J. Chen, W. Cranton, and M. Fihn, editors, *Handbook of Visual Display Technology*. Springer Berlin Heidelberg, Berlin, Heidelberg, 2012.

[89] P. Khayyatzadeh. Geometry and anchoring effects on elliptic cylinder domains of nematic phases. Master's thesis, University of Waterloo, 2014.

[90] A. Majumdar and A. Zarnescu. Landau-de Gennes theory of nematic liquid crystals: the Oseen–Frank limit and beyond. *Archive for Rational Mechanics and Analysis*, 196(1):227–280, 2010.

[91] B.-G. Wu, J. H. Erdmann, and J. W. Doane. Response times and voltages for PDLC light shutters. *Liquid Crystals*, 5(5):1453–1465, 1989.

[92] E. Willman, F. A. Fernández, R. James, and S. E. Day. Modeling of weak anisotropic anchoring of nematic liquid crystals in the Landau–de Gennes theory. *IEEE Transactions on Electron Devices*, 54(10):2630–2637, 2007.

[93] A. Rapini and M. Papoular. Distorsion d'une lamelle nématique sous champ magnétique conditions d'ancrage aux parois. *Le Journal de Physique Colloques*, 30(C4):C4–54–C4–56, 1969.

[94] M. Nobili and G. Durand. Disorientation-induced disordering at a nematic-liquid-crystalsolid interface. *Physical Review A*, 46(10):R6174–R6177, 1992.

[95] A. K. Sen and D. E. Sullivan. Landau–de Gennes theory of wetting and orientational transitions at a nematic-liquid-substrate interface. *Physical Review A*, 35(3):1391–1403, 1987.

[96] G. Barbero and A. K. Zvezdin. Thermal renormalization of the anchoring energy of nematic liquid crystals. *Physical Review E*, 62(5):6711–6721, 2000.

[97] X. Ma, G. P. Crawford, R. J. Crawford, I. Amimori, S. Žumer, G. Skačej, and S. G. Cloutier. Nuclear magnetic resonance of pretransitional ordering of liquid crystals in well defined nano-geometries: the utility of the Landau-de Gennes formalism. *Liquid Crystals*, 36(10-11):1229–1240, 2009.

[98] G. De Luca and A. D. Rey. Point and ring defects in nematics under capillary confinement. *The Journal of chemical physics*, 127(10):104902, 2007.

[99] P. Hohenberg and B. Halperin. Theory of dynamic critical phenomena. *Reviews of Modern Physics*, 49(3):435–479, 1977.

[100] R. James and E. Willman. Finite-element modeling of liquid-crystal hydrodynamics with a variable degree of order. *IEEE Transactions on Electron Devices*, 53(7):1575–1582, 2006.

[101] A. K. Bhattacharjee, G. I. Menon, and R. Adhikari. Numerical method of lines for the relaxational dynamics of nematic liquid crystals. *Physical Review E*, 78(2):1–10, 2008.

[102] R. G. Rice and D. D. Do. *Applied mathematics and modeling for chemical engineers*. John Wiley & Sons, 2012.

[103] A. Logg, K.-A. Mardal, and G. Wells. *Automated solution of differential equations by the finite element method: The FEniCS book*, volume 84. Springer Science & Business Media, 2012.

[104] A. Sparavigna, A. Sanna, B. Montrucchio, and A. Strigazzi. Streamline image analysis: a new tool for investigating defects in nematic liquid crystals. *Liquid Crystals*, 26(10):1467–1478, 1999.

[105] Y.-M. Zhu and P. A. Farrell. A vector grouping algorithm for liquid crystal tensor field visualization. *Liquid Crystals*, 29(10):1259–1264, 2002.

[106] S. Čopar, T. Porenta, and S. Žumer. Visualization methods for complex nematic fields. *Liquid Crystals*, 40(12):1759–1768, 2013.

[107] A. Vilanova, S. Zhang, G. Kindlmann, and D. Laidlaw. An introduction to visualization of diffusion tensor imaging and its applications. In J. Weickert and H. Hagen, editors, *Visualization and Processing of Tensor Fields*, Mathematics and Visualization, pages 121–153. Springer Berlin Heidelberg, 2006.

[108] F. Fu and N. M. Abukhdeir. A topologically-informed hyperstreamline seeding method for alignment tensor fields. *IEEE Transactions on Visualization and Computer Graphics*, 21(3):413–419, 2015.

[109] T. Delmarcelle and L. Hesselink. Visualizing second-order tensor fields with hyperstreamlines. *IEEE Transactions on Visualization and Computer Graphics*, 13(4):25–33, 1993.

[110] M. Warenghem, J. Henninot, and G. Abbate. Non linearly induced self waveguiding structure in dye doped nematic liquid crystals confined in capillaries. *Optics Express*, 2(12):483–490, 1998.

[111] H. J. Coles. Laser and electric field induced birefringence studies on the cyanobiphenyl homologues. *Molecular Crystals and Liquid Crystals*, 49(3):67–74, 1978.

[112] B. M. Wincure and A. D. Rey. Nanoscale analysis of defect shedding from liquid crystal interfaces. *Nano letters*, 7(6):1474–9, 2007.

[113] K. Skarp, S. Lagerwall, and B. Stebler. Measurements of hydrodynamic parameters for nematic 5CB. *Molecular Crystals and Liquid Crystals*, 60(3):215–236, 1980.

[114] E. C. Gartland, P. Palffy-Muhoray, and R. S. Varga. Numerical minimization of the Landau–de Gennes free energy: Defects in cylindrical capillaries. *Molecular Crystals and Liquid Crystals*, 199(1):429–452, 1991.

[115] S. Kralj and S. Žumer. Saddle-splay elasticity of nematic structures confined to a cylindrical capillary. *Physical Review E*, 51(1):366–379, 1995.

[116] S. Aya, K. V. Le, F. Araoka, K. Ishikawa, and H. Takezoe. Nanosize-induced optically isotropic nematic phase. *Japanese Journal of Applied Physics*, 50(5 PART 1), 2011.

[117] G. Barbero and L. R. Evangelista. *Adsorption phenomena and anchoring energy in nematic liquid crystals*. CRC Press, 2005.

[118] S. Bronnikov, S. Kostromin, and V. Zuev. Polymer-dispersed liquid crystals: Progress in preparation, investigation, and application. *Journal of Macromolecular Science, Part B*, 52(12):1718–1735, 2013.

[119] M. Kleman. *Points, Lines and Walls: In Liquid Crystals, Magnetic Systems and Various Ordered Media.* John Wiley & Sons Inc, 1982.

[120] J. Yan and A. D. Rey. Texture formation in carbonaceous mesophase fibers. *Phys. Rev. E*, 65(3):031713, 2002.

[121] D. Sharma and A. D. Rey. Simulation of texture formation processes in carbonaceous mesophase fibres. *Liquid Crystals*, 30(3):377, 2003.

[122] F. Bloisi, C. Ruocchio, P. Terrecuso, and L. Vicari. PDLC: influence of droplet order parameter in light transmittance. *Optics Communications*, 123:449–452, 1996.

[123] D. Coates. Normal and reverse mode polymer dispersed liquid crystal devices. *Displays*, 14(2):94–103, 1993.

[124] G. Luckhurst, D. Dunmur, A. Fukuda, and I. E. Group. *Physical Properties of Liquid Crystals: Nematics*. Institution of Electrical Engineers, 2001.

[125] A. Bogi and S. Faetti. Elastic, dielectric and optical constants of 4'-pentyl-4-cyanobiphenyl. *Liquid Crystals*, 28:729–739, 2001.

[126] R. D. Polak, G. P. Crawford, B. C. Kostival, J. W. Doane, and S. Zumer. Optical determination of the saddle-splay elastic constant K_{24} in nematic liquid crystals. *Physical Review E*, 49(2), 1994.

[127] A. A. Joshi, J. K. J. Whitmer, O. Guzmán, O. Guzman, N. L. Abbott, and J. J. de Pablo. Measuring liquid crystal elastic constants with free energy perturbations. *Soft Matter*, 10(6):882–893, 2014.

[128] E. Mei and D. A. Higgins. Polymer-dispersed liquid crystal films studied by near-field scanning optical microscopy. *Langmuir*, 14(8):1945–1950, 1998.

[129] Wikimedia Commons (User: Ag2gaeh). Spheroid with coordinate axes. https://commons.wikimedia.org/wiki/File:Ellipsoid-rot-ax.svg, 2015. Accessed: March 7, 2016. Licensed under CC BY-SA 4.0.

[130] P. Khayyatzadeh, F. Fu, and N. M. Abukhdeir. Field-driven dynamics of nematic microcapillaries. *Physical Review E*, 92(6):062509, 2015.

[131] A. Shams, X. Yao, J. O. Park, M. Srinivasarao, and A. D. Rey. Theory and modeling of nematic disclination branching under capillary confinement. *Soft Matter*, 8(43):11135, 2012.

[132] A. Shams, X. Yao, O. Park, and A. D. Rey. Disclination elastica model of loop collision and growth in confined nematic liquid crystals. *Soft Matter*, 11:5455–5464, 2015.

[133] S. Kralj, E. G. Virga, and S. Zumer. Biaxial torus around nematic point defects. *Physical Review E*, 60(2):1858–1866, 1999.

[134] I. Drevenšek-Olenik, M. Čopič, M. E. Sousa, and G. P. Crawford. Optical retardation of in-plane switched polymer dispersed liquid crystals. *Journal of Applied Physics*, 100(3):033515, 2006.

[135] G. E. Volovik and O. D. Lavrentovich. Topological dynamics of defects: boojums in nematic drops. *Soviet Physics JETP*, 58:1159–1166, 1983.

[136] P. S. Drzaic. A case of mistaken identity: spontaneous formation of twisted bipolar droplets from achiral nematic materials. *Liquid Crystals*, 26(5):623–627, 1999.

[137] T. Ohzono and J. Fukuda. Zigzag line defects and manipulation of colloids in a nematic liquid crystal in microwrinkle grooves. *Nature Communications*, 3:701, 2012.

[138] D. Vanzo, M. Ricci, R. Berardi, and C. Zannoni. Shape, chirality and internal order of freely suspended nematic nanodroplets. *Soft Matter*, 8(47):11790, 2012.

[139] J. Jeong, Z. S. Davidson, P. J. Collings, T. C. Lubensky, and A. G. Yodh. Chiral symmetry breaking and surface faceting in chromonic liquid crystal droplets with giant elastic anisotropy. *Proceedings of the National Academy of Sciences of the United States of America*, 111(5):1742–7, 2014.

[140] I.-H. Lin, D. S. Miller, P. J. Bertics, C. J. Murphy, J. J. D. Pablo, and N. L. Abbott. Endotoxin-induced structural transformations in liquid crystalline droplets. *Science*, 332(6035):1297–1300, 2011.

[141] D. A. Higgins, J. E. Hall, and A. Xie. Optical microscopy studies of dynamics within individual polymer-dispersed liquid crystal droplets. *Accounts of chemical research*, 38(2):137–45, 2005.

[142] E. Pairam, J. Vallamkondu, V. Koning, B. C. van Zuiden, P. W. Ellis, M. A. Bates, V. Vitelli, and A. Fernandez-Nieves. Stable nematic droplets with handles. *Proceedings of the National Academy of Sciences of the United States of America*, 110(23):9295–300, 2013.

[143] A. K. Bhattacharjee, G. I. Menon, and R. Adhikari. Fluctuating dynamics of nematic liquid crystals using the stochastic method of lines. *The Journal of Chemical Physics*, 133(4):044112, 2010.

[144] R. Ondris-Crawford, E. P. Boyko, B. G. Wagner, J. H. Erdmann, S. Zumer, and J. W. Doane. Microscope textures of nematic droplets in polymer dispersed liquid crystals. *Journal of Applied Physics*, 69(9):6380, 1991.

[145] G. Barbero and L. R. Evangelista. *An Elementary Course on the Continuum Theory for Nematic Liquid Crystals*. World Scientific, 2001.

Appendix A

Euler–Lagrange Equation for Alignment Tensor

This derivation of the Euler–Lagrange equation (also known as Euler's equation) borrows steps from Chapter 1 of ref. [145], but is performed with respect to a free energy based on a three-dimensional tensor field, i.e. $F[\mathbf{Q}]$, instead of a one-dimensional scalar field.

From Landau–de Gennes theory, we know the free energy density with respect to a tensorial order parameter $\mathbf{Q}$ is $f(\mathbf{Q}, \boldsymbol{\nabla}\mathbf{Q})$. The total free energy (also known as the energy *functional*), is given by the integral of the free energy density over the entire domain of the problem plus the surface energy contribution in the case of weak anchoring (Neumann boundary). In three dimensions, this can be written as

$$F[\mathbf{Q}] = F_b + F_s = \iiint_V f(\mathbf{Q}, \boldsymbol{\nabla}\mathbf{Q})\, dV + \oiint_A f_s(\mathbf{Q})\, dA$$

where V represents the volume over space (x_i where $i = 1, 2, 3$) and A is the surface formed by the boundary over the domain. We are interested in the tensor field $\widetilde{\mathbf{Q}}$ which minimizes the value of this functional, i.e. $F[\widetilde{\mathbf{Q}}] = 0$. Any other tensor field and its gradient can be expressed by the equations

$$\mathbf{Q} = \widetilde{\mathbf{Q}} + \alpha\mathbf{T}$$
$$\boldsymbol{\nabla}\mathbf{Q} = \boldsymbol{\nabla}\widetilde{\mathbf{Q}} + \alpha\boldsymbol{\nabla}\mathbf{T}$$

where $\mathbf{T}$ is an arbitrary function (belonging to the same function space as $\mathbf{Q}$, i.e. also a second-rank tensor) and α is a real number. The minimizing function is (obviously) found

when $\alpha = 0$. As a result, we can say that

$$\frac{\mathrm{d}F[\mathbf{Q}]}{\mathrm{d}\alpha}\Big|_{\alpha=0} = 0$$

which we can also represent by $\delta F = 0$, where δF is called the *first variation* of the functional. (Aside: analogously to ordinary functions, for a functional to have a relative minimum, we also require that the *second variation* $\delta^2 F > 0$.)

We can evaluate this condition, starting with the bulk contribution:

$$\begin{aligned}
\frac{\mathrm{d}F_b}{\mathrm{d}\alpha}\Big|_{\alpha=0} &= \iiint_V \left[\frac{\mathrm{d}}{\mathrm{d}\alpha} f(\widetilde{\mathbf{Q}} + \alpha\mathbf{T}, \boldsymbol{\nabla}\widetilde{\mathbf{Q}} + \alpha\boldsymbol{\nabla}\mathbf{T})\right]_{\alpha=0} dV \\
&= \iiint_V \left[\frac{\partial f}{\partial \mathbf{Q}} : \frac{\partial \mathbf{Q}}{\partial \alpha} + \frac{\partial f}{\partial \boldsymbol{\nabla}\mathbf{Q}} \vdots \frac{\partial \boldsymbol{\nabla}\mathbf{Q}}{\partial \alpha}\right]_{\alpha=0} dV \quad \text{(chain rule)} \\
&= \iiint_V \frac{\partial f}{\partial \widetilde{\mathbf{Q}}} : \mathbf{T} + \frac{\partial f}{\partial \boldsymbol{\nabla}\widetilde{\mathbf{Q}}} \vdots \boldsymbol{\nabla}\mathbf{T}\, dV \quad (\alpha = 0, \text{ substitute derivatives})
\end{aligned}$$

Note that the insertion of : and $\vdots$ (double and triple dot products) results from the application of multivariable chain rule where each element of $\mathbf{Q}$ is treated as an independent variable in f, i.e. we find $\frac{\mathrm{d}f}{\mathrm{d}\mathbf{Q}} = \frac{\partial f}{\partial Q_{11}}\frac{\partial Q_{11}}{\partial \alpha} + \frac{\partial f}{\partial Q_{12}}\frac{\partial Q_{12}}{\partial \alpha} + ... = \frac{\partial f}{\partial \mathbf{Q}} : \frac{\partial \mathbf{Q}}{\partial \alpha}$. From here, note that we can rewrite the second term in this equation, since we know from product rule that

$$\begin{aligned}
\boldsymbol{\nabla} \cdot \left(\frac{\partial f}{\partial \boldsymbol{\nabla}\widetilde{\mathbf{Q}}} : \mathbf{T}\right) &= \boldsymbol{\nabla} \cdot \left(\frac{\partial f}{\partial \boldsymbol{\nabla}\widetilde{\mathbf{Q}}}\right) : \mathbf{T} + \frac{\partial f}{\partial \boldsymbol{\nabla}\widetilde{\mathbf{Q}}} \vdots \boldsymbol{\nabla}\mathbf{T} \\
\frac{\partial f}{\partial \boldsymbol{\nabla}\widetilde{\mathbf{Q}}} \vdots \boldsymbol{\nabla}\mathbf{T} &= \boldsymbol{\nabla} \cdot \left(\frac{\partial f}{\partial \boldsymbol{\nabla}\widetilde{\mathbf{Q}}} : \mathbf{T}\right) - \boldsymbol{\nabla} \cdot \left(\frac{\partial f}{\partial \boldsymbol{\nabla}\widetilde{\mathbf{Q}}}\right) : \mathbf{T} \quad \text{(rearranging)}
\end{aligned}$$

(Note that this is analogous to integration by parts, except in three dimensions.) Substituting this expression back into our original integral:

$$\begin{aligned}
\frac{\mathrm{d}F_b}{\mathrm{d}\alpha}\Big|_{\alpha=0} &= \iiint_V \frac{\partial f}{\partial \widetilde{\mathbf{Q}}} : \mathbf{T} - \boldsymbol{\nabla} \cdot \left(\frac{\partial f}{\partial \boldsymbol{\nabla}\widetilde{\mathbf{Q}}}\right) : \mathbf{T} + \boldsymbol{\nabla} \cdot \left(\frac{\partial f}{\partial \boldsymbol{\nabla}\widetilde{\mathbf{Q}}} : \mathbf{T}\right) dV \\
&= \iiint_V \left[\frac{\partial f}{\partial \widetilde{\mathbf{Q}}} - \boldsymbol{\nabla} \cdot \left(\frac{\partial f}{\partial \boldsymbol{\nabla}\widetilde{\mathbf{Q}}}\right)\right] : \mathbf{T}\, dV + \iiint_V \boldsymbol{\nabla} \cdot \left(\frac{\partial f}{\partial \boldsymbol{\nabla}\widetilde{\mathbf{Q}}} : \mathbf{T}\right) dV \\
&= \iiint_V \left[\frac{\partial f}{\partial \widetilde{\mathbf{Q}}} - \boldsymbol{\nabla} \cdot \left(\frac{\partial f}{\partial \boldsymbol{\nabla}\widetilde{\mathbf{Q}}}\right)\right] : \mathbf{T}\, dV + \oiint_A \mathbf{n} \cdot \left(\frac{\partial f}{\partial \boldsymbol{\nabla}\widetilde{\mathbf{Q}}} : \mathbf{T}\right) dA \quad \text{(divergence thm)}
\end{aligned}$$

where $\mathbf{n}$ is the surface normal vector to dA. Imposing our minimization condition ($\frac{\mathrm{d}F}{\mathrm{d}\alpha}|_{\alpha=0}$= 0), we find that, within the domain (in the bulk), the minimizing tensor field $\widetilde{\mathbf{Q}}$ must be a

solution to the following partial differential equation (the Euler–Lagrange equation):

$$\boxed{\frac{\partial f}{\partial \widetilde{\mathbf{Q}}} - \boldsymbol{\nabla} \cdot \left(\frac{\partial f}{\partial \boldsymbol{\nabla} \widetilde{\mathbf{Q}}} \right) = 0}$$

What about on the surface? If we evaluate our condition on the surface contribution of F (which we skipped over earlier), using the same steps, we eventually arrive at

$$\left. \frac{\mathrm{d}F_s}{\mathrm{d}\alpha} \right|_{\alpha=0} = \oiint_A \frac{\partial f_s}{\partial \widetilde{\mathbf{Q}}} : \mathbf{T} \, dA = 0$$

which, when combined with the surface integral resulting from applying the divergence theorem on the derivative of the bulk free energy from earlier, gives us the following expression:

$$\oiint_A \left(\frac{\partial f_s}{\partial \widetilde{\mathbf{Q}}} + \mathbf{n} \cdot \frac{\partial f}{\partial \boldsymbol{\nabla} \widetilde{\mathbf{Q}}} \right) : \mathbf{T} \, dA = 0$$

Therefore we also get the following boundary condition as part of our minimization problem:

$$\boxed{\frac{\partial f_s}{\partial \widetilde{\mathbf{Q}}} + \mathbf{n} \cdot \left(\frac{\partial f}{\partial \boldsymbol{\nabla} \widetilde{\mathbf{Q}}} \right) = 0}$$

Appendix B

Ginzburg-Landau Model Weak Form Derivation

The bulk (thermodynamic and external electric field) and elasticity portions of the Landau–de Gennes free energy density are commonly expressed as the following (in Einstein/index notation):

$$f_b = \frac{1}{2}a(Q_{ij}Q_{ji}) + \frac{1}{3}b(Q_{ij}Q_{jk}Q_{ki}) + \frac{1}{4}c(Q_{ij}Q_{ji})^2 \tag{B.1}$$

$$f_e = -\frac{\varepsilon_0}{8\pi}\left[\frac{\varepsilon_\parallel + 2\varepsilon_\perp}{3}\delta_{ij} + (\varepsilon_\parallel - \varepsilon_\perp)Q_{ij}\right]E_jE_i \tag{B.2}$$

$$f_{el} = \frac{1}{2}L_1(\partial_i Q_{jk}\partial_i Q_{kj}) + \frac{1}{2}L_2(\partial_i Q_{ij}\partial_k Q_{kj}) + \frac{1}{2}L_3(Q_{ij}\partial_i Q_{kl}\partial_j Q_{kl}) + \frac{1}{2}L_{24}(\partial_k Q_{ij}\partial_j Q_{ik}) \tag{B.3}$$

Note $a = a_0(T - T^*_{ni})$ in the above expression. Minimization of the total free energy $F = \int_V f_b + f_e + f_{el}\, dV$ is performed using the time-dependent Ginzburg-Landau model (Model A dynamics) [99], which says that the rate of change of Q_{ij} is proportional to the Euler–Lagrange equation with the following form:

$$\mu_r\frac{\partial Q_{ij}}{\partial t} = -\left[\frac{\delta F}{\delta Q_{ij}}\right]^{ST} = -\left[\frac{\partial F}{\partial Q_{ij}} - \frac{\partial}{\partial x_k}\left(\frac{\partial F}{\partial(\partial_k Q_{ij})}\right)\right]^{ST} \tag{B.4}$$

Thus the right-most expression in this equation needs to be determined to find the evolution of the system.

The following equations or identities are employed in the derivation:

$$
\begin{aligned}
Q_{ij} &= \sum_{ij} Q_{ij}\, \mathbf{e_i e_j} \\
\frac{\partial Q_{ij}}{\partial Q_{lm}} &= \delta_{il}\delta_{jm} \\
\delta_{ij}\delta_{jk} &= \delta_{ik} \\
Q_{ij}\delta_{jk} &= Q_{ik} \\
[Q_{ij}]^S &= \frac{1}{2}(Q_{ij} + Q_{ji}) \\
[Q_{ij}]^T &= Q_{ij} - \frac{1}{3}Q_{kk}\delta_{ij}
\end{aligned}
$$

where $\mathbf{e_i}$ and $\mathbf{e_j}$ are dyadic (basis) vectors associated with a Cartesian coordinate system ($i, j = 1, 2, 3$). And specifically for Q_{ij}, since it is symmetric-traceless:

$$
\begin{aligned}
Q_{ij} &= Q_{ji} \\
Q_{33} &= -(Q_{11} + Q_{22})
\end{aligned}
$$

Also, since tensors are simply summations of products, we can still use regular calculus rules when performing differentiations (e.g. chain rule, product rule).

B.1 Expansion of Euler-Lagrange Equation

The aim is to compute the individual terms in Equation B.4. Contributions to the total free energy F are denoted by F_b for bulk free energy, F_{L_1} for the L_1 contribution of the elastic free energy, etc. (generally following the notation for the free energy density f). Begin by finding $\frac{\partial F}{\partial Q_{ab}}$:

$$
\begin{aligned}
\frac{\partial F_b}{\partial Q_{ab}} &= \frac{a}{2}\frac{\partial (Q_{ij}Q_{ji})}{\partial Q_{ab}} - \frac{b}{3}\frac{\partial (Q_{ij}Q_{jk}Q_{ki})}{\partial Q_{ab}} + \frac{c}{4}\frac{\partial [(Q_{ij}Q_{ji})^2]}{\partial Q_{ab}} \\
&= \frac{a}{2}\left(Q_{ij}\frac{\partial Q_{ji}}{\partial Q_{ab}} + Q_{ji}\frac{\partial Q_{ij}}{\partial Q_{ab}}\right) \\
&\quad - \frac{b}{3}\left(Q_{ij}\frac{\partial Q_{jk}}{\partial Q_{ab}}Q_{ki} + Q_{ij}Q_{jk}\frac{\partial Q_{ki}}{\partial Q_{ab}} + \frac{\partial Q_{ij}}{\partial Q_{ab}}Q_{jk}Q_{ki}\right) + \frac{c}{4}\left(2(Q_{ij}Q_{ji})\frac{\partial (Q_{ij}Q_{ji})}{\partial Q_{ab}}\right) \\
&= \frac{a}{2}\left(Q_{ba} + Q_{ab}\right) - \frac{b}{3}\left(Q_{ia}Q_{bi} + Q_{bj}Q_{ja} + Q_{bk}Q_{ka}\right) + \frac{c}{4}\left(2(Q_{ij}Q_{ji})(Q_{ab} + Q_{ba})\right) \\
&= a(Q_{ab}) - b(Q_{ai}Q_{ib}) + c(Q_{ab}(Q_{ij}Q_{ji}))
\end{aligned}
$$

The first and last terms are obviously symmetric-traceless since they involve only a single Q_{ab}. The second term is symmetric but not traceless,

$$\begin{aligned}\left[\frac{\partial F_b}{\partial Q_{ab}}\right]^{ST} &= a(Q_{ab}) - b(Q_{ai}Q_{ib}) + c(Q_{ab}(Q_{ij}Q_{ji})) + \frac{b}{3}(Q_{ij}Q_{ji})\delta_{ab} \\ &= a(Q_{ab}) - b(Q_{ai}Q_{ib} - \frac{1}{3}(Q_{ij}Q_{ji})\delta_{ab}) + c(Q_{ab}(Q_{ij}Q_{ji}))\end{aligned}$$

Similarly for the electric field term,

$$\left[\frac{\partial F_e}{\partial Q_{ab}}\right]^{ST} = -\frac{\varepsilon_0}{8\pi}(\varepsilon_\parallel - \varepsilon_\perp)(E_iE_j - \frac{1}{3}E_kE_k\delta_{ij})$$

Find $\partial_a\left(\frac{\partial F}{\partial(\partial_a Q_{bc})}\right)$, starting with L_1 term:

$$\begin{aligned}\frac{\partial F_{L_1}}{\partial(\partial_a Q_{bc})} &= \frac{L_1}{2}\frac{\partial(\partial_i Q_{jk}\partial_i Q_{kj})}{\partial(\partial_a Q_{bc})} \\ &= \frac{L_1}{2}\left(\partial_i Q_{jk}\frac{\partial(\partial_i Q_{kj})}{\partial(\partial_a Q_{bc})} + \frac{\partial(\partial_i Q_{jk})}{\partial(\partial_a Q_{bc})}\partial_i Q_{kj}\right) \\ &= \frac{L_1}{2}(\partial_a Q_{cb} + \partial_a Q_{cb}) \\ &= L_1\partial_a Q_{bc}\end{aligned} \tag{B.5}$$

Taking the divergence:

$$\partial_a\left(\frac{\partial F_{L_1}}{\partial(\partial_a Q_{bc})}\right) = L_1\partial_i\partial_i Q_{bc}$$

Note that this is the Laplacian of Q_{ab} and is already symmetric and traceless.

For the L_2 term:

$$\begin{aligned}\frac{\partial F_{L_2}}{\partial(\partial_a Q_{bc})} &= \frac{L_1}{2}\frac{\partial(\partial_i Q_{ij}\partial_k Q_{kj})}{\partial(\partial_a Q_{bc})} \\ &= \frac{L_2}{2}\left(\partial_i Q_{ij}\frac{\partial(\partial_k Q_{kj})}{\partial(\partial_a Q_{bc})} + \frac{\partial(\partial_i Q_{ij})}{\partial(\partial_a Q_{bc})}\partial_k Q_{kj}\right) \\ &= \frac{L_2}{2}\left(\partial_i Q_{ij}\delta_{ka}\delta_{kb}\delta_{jc} + \delta_{ia}\delta_{ib}\delta_{jc}\partial_k Q_{kj}\right) \\ &= \frac{L_2}{2}\left(\partial_i Q_{ic}\delta_{ab} + \delta_{ab}\partial_k Q_{kc}\right) \\ &= L_2\partial_i Q_{ic}\delta_{ab}\end{aligned} \tag{B.6}$$

Taking the divergence:

$$\partial_a \left(\frac{\partial F_{L_2}}{\partial(\partial_a Q_{bc})} \right) = \partial_a \left(L_2 \partial_i Q_{ic} \delta_{ab} \right) = L_2 \partial_b \partial_i Q_{ic}$$

Taking the symmetric-traceless part of this expression, we simply get:

$$\left[\partial_a \left(\frac{\partial F_{L_2}}{\partial(\partial_a Q_{bc})} \right) \right]^{ST} = L_2 \left[\frac{1}{2} \left(\partial_b \partial_i Q_{ic} + \partial_c \partial_i Q_{ib} \right) - \frac{1}{3} \partial_j \partial_i Q_{ij} \delta_{bc} \right]$$

For the L_{24} term, the result eventually ends up being the same as L_2:

$$\begin{aligned} \frac{\partial F_{L_{24}}}{\partial(\partial_a Q_{bc})} &= \frac{L_{24}}{2} \frac{\partial(\partial_k Q_{ij} \partial_j Q_{ik})}{\partial(\partial_a Q_{bc})} \\ &= \frac{L_{24}}{2} \left(\partial_k Q_{ij} \frac{\partial(\partial_j Q_{ik})}{\partial(\partial_a Q_{bc})} + \frac{\partial(\partial_k Q_{ij})}{\partial(\partial_a Q_{bc})} \partial_j Q_{ik} \right) \\ &= \frac{L_{24}}{2} \left(\partial_c Q_{ba} + \partial_c Q_{ba} \right) \\ &= L_{24} \partial_c Q_{ba} \end{aligned} \tag{B.7}$$

Taking the divergence:

$$\begin{aligned} \partial_a \left(\frac{\partial F_{L_{24}}}{\partial(\partial_a Q_{bc})} \right) &= L_{24} \partial_a \partial_c Q_{ba} \\ &= L_{24} \partial_c \partial_a Q_{ab} \quad \text{(same result as in } L_2 \text{ derivation)} \end{aligned}$$

Therefore the final expression is simply:

$$\begin{aligned} \left[\partial_a \left(\frac{\partial F_{L_{24}}}{\partial(\partial_a Q_{bc})} \right) \right]^{ST} &= L_{24} \left[\frac{1}{2} \left(\partial_b \partial_i Q_{ic} + \partial_c \partial_i Q_{ib} \right) - \frac{1}{3} \partial_j \partial_i Q_{ij} \delta_{bc} \right] \\ &= L_{24} \partial_i \left[\frac{1}{2} \left(\partial_b Q_{ic} + \partial_c Q_{ib} \right) - \frac{1}{3} \partial_j Q_{ij} \delta_{bc} \right] \end{aligned}$$

For the L_3 term, which is third order, there is both a $\frac{\partial F_{L_3}}{\partial Q_{ab}}$ and $\partial_a \left(\frac{\partial F_{L_3}}{\partial(\partial_a Q_{bc})} \right)$ component:

$$\begin{aligned} \frac{\partial F_{L_3}}{\partial Q_{ab}} &= \frac{L_3}{2} \frac{\partial(Q_{ij} \partial_i Q_{kl} \partial_j Q_{kl})}{\partial Q_{ab}} \\ &= \frac{L_3}{2} \frac{\partial Q_{ij}}{\partial Q_{ab}} \partial_i Q_{kl} \partial_j Q_{kl} \\ &= \frac{L_3}{2} \partial_a Q_{kl} \partial_b Q_{kl} \end{aligned}$$

This is clearly symmetric, but not traceless, so:

$$\left[\frac{\partial F_{L_3}}{\partial Q_{ab}}\right]^{ST} = L_3\left[\frac{1}{2}\partial_a Q_{kl}\partial_b Q_{kl} - \frac{1}{6}\partial_j Q_{kl}\partial_j Q_{kl}\delta_{ab}\right]$$

For the $\partial_a\left(\frac{\partial F_{L_3}}{\partial(\partial_a Q_{bc})}\right)$ component:

$$\begin{aligned}\frac{\partial F_{L_3}}{\partial(\partial_a Q_{bc})} &= \frac{L_3}{2}\frac{\partial(Q_{ij}\partial_i Q_{kl}\partial_j Q_{kl})}{\partial(\partial_a Q_{bc})} \\ &= \frac{L_3}{2}Q_{ij}\left(\frac{\partial(\partial_i Q_{kl})}{\partial(\partial_a Q_{bc})}\partial_j Q_{kl} + \partial_i Q_{kl}\frac{\partial(\partial_j Q_{kl})}{\partial(\partial_a Q_{bc})}\right) \\ &= \frac{L_3}{2}\left(Q_{aj}\partial_j Q_{bc} + Q_{ia}\partial_i Q_{bc}\right) \\ &= L_3 Q_{aj}\partial_j Q_{bc}\end{aligned} \tag{B.8}$$

Taking the divergence:

$$\begin{aligned}\partial_a\left(\frac{\partial F_{L_3}}{\partial(\partial_a Q_{bc})}\right) &= L_3\partial_a(Q_{aj}\partial_j Q_{bc}) \\ &= L_3(Q_{aj}\partial_a\partial_j Q_{bc} + \partial_a Q_{aj}\partial_j Q_{bc})\end{aligned}$$

This result is already symmetric and traceless.

In summary, the governing Ginzburg-Landau type equation can be written as (note I have renormalized the indices to i, j, k, etc. for clarity):

$$\begin{aligned}\mu_r\frac{\partial Q_{ij}}{\partial t} &= -\left[\frac{\partial F}{\partial Q_{ij}} - \frac{\partial}{\partial x_k}\left(\frac{\partial F}{\partial(\partial_k Q_{ij})}\right)\right]^{ST} \\ &= -\Bigg[a(Q_{ij}) - b(Q_{ik}Q_{kj} + \frac{1}{3}Q_{kl}Q_{lk}\delta_{ij}) + c(Q_{kl}Q_{lk}Q_{ij}) \\ &\qquad - \frac{\varepsilon_0}{8\pi}(\varepsilon_\parallel - \varepsilon_\perp)(E_iE_j - \frac{1}{3}E_kE_k\delta_{ij}) \\ &\qquad - L_1(\partial_k\partial_k Q_{ij}) - (L_2 + L_{24})\partial_k\left(\frac{1}{2}\left(\partial_i Q_{kj} + \partial_j Q_{ki}\right) - \frac{1}{3}\partial_l Q_{lk}\delta_{ij}\right) \\ &\qquad - L_3(Q_{kl}\partial_k\partial_l Q_{ij} + \partial_k Q_{kl}\partial_l Q_{ij} - \frac{1}{2}\partial_i Q_{kl}\partial_j Q_{kl} + \frac{1}{6}\partial_k Q_{lm}\partial_k Q_{lm}\delta_{ij})\Bigg]\end{aligned}$$

Note that the gradient terms we calculated became negative when inserted into the governing equation.

B.2 Boundary Conditions

The Euler–Lagrange equation also has an accompanying boundary condition with the following form:

$$\left[\frac{\partial f_s}{\partial Q_{ij}} - n_i\left(\frac{\partial F}{\partial(\partial_i Q_{jk})}\right)\right]^{ST} = 0$$

where f_s is the surface potential (versus the bulk potential F). We use a linear anchoring potential for homeotropic anchoring:

$$f_s = \alpha n_i Q_{ij} n_j$$

where α is the strength of the anchoring, which should be negative for homeotropic anchoring. Clearly,

$$\left[\frac{\partial f_s}{\partial Q_{ij}}\right]^{ST} = \alpha n_i n_j - \frac{1}{3} n_k n_k \delta_{ij}$$

The other surface terms can be drawn from the previous work in Section B.1 regarding the elasticity terms (only without the divergence in the front).

$$\begin{aligned} n_a \frac{\partial F}{\partial(\partial_a Q_{bc})} &= n_a \left[L_1 \partial_a Q_{bc} + L_2 \partial_i Q_{ic} \delta_{ab} + L_{24} \partial_c Q_{ba} + L_3 Q_{aj} \partial_j Q_{bc}\right] \\ &= L_1 n_a \partial_a Q_{bc} + L_2 n_b \partial_i Q_{ic} + L_{24} n_a \partial_c Q_{ba} + L_3 n_a Q_{aj} \partial_j Q_{bc} \end{aligned}$$

So the final boundary condition is:

$$\begin{aligned} \left[n_a \frac{\partial F}{\partial(\partial_a Q_{bc})}\right]^{ST} &= L_1 (n_a \partial_a Q_{bc}) + L_2 \left(\frac{1}{2}(n_b \partial_i Q_{ic} + n_c \partial_i Q_{ib}) - \frac{1}{3} n_j \partial_i Q_{ij} \delta_{bc}\right) \\ &\quad + L_{24} \left(\frac{1}{2}(n_a \partial_c Q_{ba} + n_a \partial_b Q_{ca}) - \frac{1}{3} n_j \partial_i Q_{ij} \delta_{bc}\right) + L_3 n_a Q_{aj} \partial_j Q_{bc} \\ &= \alpha n_i n_j - \frac{1}{3} n_k n_k \delta_{ij} \end{aligned}$$

which we will employ later.

B.3 Weak Form for Finite Element Method

Following the method of weighted residuals, multiply the PDE (residual) by a test function $\mathbf{v}$ (taking the inner product, i.e. v_{ji}) and integrate over the volume of the domain V:

$$\begin{aligned}\iiint_V \mu_r \frac{\partial Q_{ij}}{\partial t} v_{ji}\, dV = -\iiint_V \Bigg[& a(Q_{ij}) - b(Q_{ik}Q_{kj} - \frac{1}{3}Q_{kl}Q_{lk}\delta_{ij}) + c(Q_{kl}Q_{lk}Q_{ij}) \\ & - \frac{\varepsilon_0}{8\pi}(\varepsilon_\parallel - \varepsilon_\perp)(E_iE_j - \frac{1}{3}E_kE_k\delta_{ij}) - L_1(\partial_k\partial_k Q_{ij}) \\ & - (L_2 + L_{24})\partial_k\left(\frac{1}{2}(\partial_i Q_{kj} + \partial_j Q_{ki}) - \frac{1}{3}\partial_l Q_{lk}\delta_{ij}\right) - L_3\Bigg(Q_{kl}\partial_k\partial_l Q_{ij} \\ & + \partial_k Q_{kl}\partial_l Q_{ij} - \frac{1}{2}\partial_i Q_{kl}\partial_j Q_{kl} + \frac{1}{6}\partial_k Q_{lm}\partial_k Q_{lm}\delta_{ij}\Bigg)\Bigg] v_{ji}\, dV\end{aligned}$$

We can simplify the second derivatives above by applying the following product rule identities (i.e. Green's identity) to the L_1, L_2/L_{24} and L_3 terms.

$$\text{For } L_1\text{:}\quad \partial_k(\partial_k Q_{ij} v_{ji}) = \partial_k Q_{ij}\partial_k v_{ji} + \partial_k\partial_k Q_{ij} v_{ji}$$

$$\begin{aligned}\text{For } L_2/L_{24}\text{:}\quad \partial_k((\partial_i Q_{kj} + \partial_j Q_{ki})v_{ji}) &= \partial_i Q_{kj}\partial_k v_{ji} + \partial_j Q_{ki}\partial_k v_{ji} + \partial_k\partial_i Q_{kj} v_{ji} + \partial_k\partial_j Q_{ki} v_{ji} \\ \partial_k(\partial_l Q_{lk}\delta_{ij} v_{ji}) &= \partial_l Q_{lk}\delta_{ij}\partial_k v_{ji} + \partial_k\partial_l Q_{lk}\delta_{ij} v_{ji}\end{aligned}$$

$$\text{For } L_3\text{:}\quad \partial_k(Q_{kl}\partial_l Q_{ij} v_{ji}) = \partial_k Q_{kl}\partial_l Q_{ij} v_{ji} + Q_{kl}\partial_l Q_{ij}\partial_k v_{ji} + Q_{kl}\partial_k\partial_l Q_{ij} v_{ji}$$

These can be rewritten as integral expressions by integrating both sides and using divergence theorem to convert the volume integrals to surface integrals over A), for example for L_1:

$$\begin{aligned}\iiint_V \partial_k\partial_k Q_{ij}\, dV &= \iiint_V \partial_k(\partial_k Q_{ij} v_{ji})\, dV - \iiint_V \partial_k Q_{ij}\partial_k v_{ji}\, dV \\ &= \oiint_A \partial_k Q_{ij} v_{ji} n_k\, dA - \iiint_V \partial_k Q_{ij}\partial_k v_{ji}\, dV\end{aligned}$$

where n_k is the outward pointing surface normal vector. For the other terms (where the left-hand side here is the term from the integral equation that needs to be substituted):

$$\iiint_V (\partial_k\partial_i Q_{kj} + \partial_k\partial_j Q_{ki}) v_{ji}\, dV = \oiint_A (\partial_i Q_{kj} + \partial_j Q_{ki}) v_{ji} n_k\, dA - \iiint_V (\partial_i Q_{kj}\partial_k + \partial_j Q_{ki}\partial_k v_{ji})\, dV$$

$$\iiint_V \partial_k\partial_l Q_{lk}\delta_{ij} v_{ji}\, dV = \oiint_A (\partial_l Q_{lk}\delta_{ij} v_{ji}) n_k\, dA - \iiint_V \partial_l Q_{lk}\delta_{ij}\partial_k v_{ji}\, dV$$

$$\iiint_V (Q_{kl}\partial_k\partial_l Q_{ij} v_{ji} + \partial_k Q_{kl}\partial_l Q_{ij} v_{ji})\, dV = \oiint_A (Q_{kl}\partial_l Q_{ij} v_{ji}) n_k\, dA - \iiint_V Q_{kl}\partial_l Q_{ij}\partial_k v_{ji}\, dV$$

Substituting these expressions, we can rewrite the weak form of the equation as:

$$\begin{aligned}\iiint_V \mu_r \frac{\partial Q_{ij}}{\partial t} v_{ji}\, dV = -\iiint_V \Bigg[\Bigg(& a(Q_{ij}) - b(Q_{ik}Q_{kj} - \frac{1}{3}Q_{kl}Q_{lk}\delta_{ij}) + c(Q_{kl}Q_{lk}Q_{ij}) \\ & - \frac{\varepsilon_0}{8\pi}(\varepsilon_\parallel - \varepsilon_\perp)(E_iE_j - \frac{1}{3}E_kE_k\delta_{ij}) \Bigg) v_{ji} + L_1(\partial_k Q_{ij}\partial_k v_{ji}) \\ & + (L_2 + L_{24}) \left(\frac{1}{2}(\partial_i Q_{kj}\partial_k v_{ji} + \partial_j Q_{ki}\partial_k v_{ji}) - \frac{1}{3}\partial_l Q_{lk}\partial_k v_{ji}\delta_{ij} \right) \\ & + L_3 \left(Q_{kl}\partial_l Q_{ij}\partial_k v_{ji} + \frac{1}{2}\partial_i Q_{kl}\partial_j Q_{kl} v_{ji} - \frac{1}{6}\partial_k Q_{lm}\partial_k Q_{lm}\delta_{ij} v_{ji} \right) \Bigg]\, dV \\ - \oiint_A \Big[& L_1(\partial_k Q_{ij} v_{ji}) \\ & + (L_2 + L_{24}) \left(\frac{1}{2}(\partial_i Q_{kj} + \partial_j Q_{ki}) v_{ji} - \frac{1}{3}(\partial_l Q_{lk}\delta_{ij} v_{ji}) \right) \\ & + L_3(Q_{kl}\partial_l Q_{ij} v_{ji}) \Big]\, n_k\, dA\end{aligned}$$

where we can note that all terms have been reduced to first derivatives only. We can use the final equation from Section B.2 to replace the surface integrals terms with the preferred surface anchoring energy:

$$\begin{aligned}\iiint_V \mu_r \frac{\partial Q_{ij}}{\partial t} v_{ji}\, dV = -\iiint_V \Bigg[\Bigg(& a(Q_{ij}) - b(Q_{ik}Q_{kj} - \frac{1}{3}Q_{kl}Q_{lk}\delta_{ij}) + c(Q_{kl}Q_{lk}Q_{ij}) \\ & - \frac{\varepsilon_0}{8\pi}(\varepsilon_\parallel - \varepsilon_\perp)(E_iE_j - \frac{1}{3}E_kE_k\delta_{ij}) \Bigg) v_{ji} + L_1(\partial_k Q_{ij}\partial_k v_{ji}) \\ & + (L_2 + L_{24}) \left(\frac{1}{2}(\partial_i Q_{kj}\partial_k v_{ji} + \partial_j Q_{ki}\partial_k v_{ji}) - \frac{1}{3}\partial_l Q_{lk}\partial_k v_{ji}\delta_{ij} \right) \\ & + L_3 \left(Q_{kl}\partial_l Q_{ij}\partial_k v_{ji} + \frac{1}{2}\partial_i Q_{kl}\partial_j Q_{kl} v_{ji} - \frac{1}{6}\partial_k Q_{lm}\partial_k Q_{lm}\delta_{ij} v_{ji} \right) \Bigg]\, dV \\ - \oiint_A & \alpha n_i n_j v_{ji}\, dA\end{aligned}$$

B.4 Dimensionless Scaling

We can non-dimensionalize the system by scaling the dimensional parameters to dimensionless ones in order to improve numerical behaviour by avoiding issues such as round-off or

truncation error. This step also gives insight into the important parameters of the system. We set our dimensionless variables to:

$$\tilde{x} = \frac{x}{l}, \quad \tilde{t} = \frac{t}{\tau}, \quad \tilde{T} = \frac{T - T^*_{ni}}{T^*_{ni}}$$

Recall $a = a_0(T - T^*_{ni})$, $V = x^3$, $A = x^2$, and $\partial_i = \frac{\partial}{\partial x_i}$. Substituting for our dimensional variables (and getting rid of the tildes), and rearranging, we get:

$$\begin{aligned}
\iiint_V \frac{\mu_r}{\tau a_0 T^*_{ni}} \frac{\partial Q_{ij}}{\partial t} v_{ji}\, dV = -\iiint_V \Bigg[\Bigg(& \underbrace{\frac{T}{a}}(Q_{ij}) - \underbrace{\frac{b}{a_0 T^*_{ni}}}_{b}(Q_{ik}Q_{kj} - \frac{1}{3}Q_{kl}Q_{lk}\delta_{ij}) \\
& + \underbrace{\frac{c}{a_0 T^*_{ni}}}_{c}(Q_{kl}Q_{lk}Q_{ij}) - \underbrace{\frac{\varepsilon_0}{8\pi a_0 T_{ni}}(\varepsilon_\parallel - \varepsilon_\perp)}_{\epsilon}(E_iE_j - \frac{1}{3}E_kE_k\delta_{ij}) \Bigg) v_{ji} \\
& + \underbrace{\frac{L_1}{l^2 a_0 T^*_{ni}}}_{L_1}(\partial_k Q_{ij}\partial_k v_{ji}) \\
& + \underbrace{\frac{(L_2 + L_{24})}{l^2 a_0 T^*_{ni}}}_{L_2, L_{24}} \left(\frac{1}{2}(\partial_i Q_{kj}\partial_k v_{ji} + \partial_j Q_{ki}\partial_k v_{ji}) - \frac{1}{3}\partial_l Q_{lk}\partial_k v_{ji}\delta_{ij} \right) \\
& + \underbrace{\frac{L_3}{l^2 a_0 T^*_{ni}}}_{L_3} \Bigg(Q_{kl}\partial_l Q_{ij}\partial_k v_{ji} + \frac{1}{2}\partial_i Q_{kl}\partial_j Q_{kl} v_{ji} \\
& - \frac{1}{6}\partial_k Q_{lm}\partial_k Q_{lm}\delta_{ij} v_{ji} \Bigg) \Bigg]\, dV \\
- \oiint_A & \underbrace{\frac{\alpha}{l a_0 T^*_{ni}}}_{\alpha} n_i n_j v_{ji}\, dA
\end{aligned}$$

where the underbraces denote the relevant dimensionless quantities that are obtained using this scheme. Note that setting the coefficient in the time derivative to unity, we arrive at $\tau = \frac{\mu}{a_0 T^*_{ni}}$ as the time scaling.

An alternative scaling method exposes the nematic coherence length $\lambda_n = \sqrt{\frac{L_1}{a_0(T^*_{ni}-T)}}$ and the surface extrapolation length $\lambda_s = \frac{L_1}{\alpha}$, and scaling the elastic parameters with respect to L_1:

$$\begin{aligned}\iiint_V \frac{\mu_r l^2}{\tau L_1}\frac{\partial Q_{ij}}{\partial t} v_{ji}\, dV = -\iiint_V \Bigg[\Bigg(&\underbrace{\frac{a_0(T-T^*_{ni})}{L_1}}_{a} l^2 (Q_{ij}) - \underbrace{\frac{bl^2}{L_1}}_{b}(Q_{ik}Q_{kj} - \frac{1}{3}Q_{kl}Q_{lk}\delta_{ij}) \\ &+ \underbrace{\frac{cl^2}{L_1}}_{c}(Q_{kl}Q_{lk}Q_{ij}) - \underbrace{\frac{\varepsilon_0 l^2 E_s^2}{8\pi L_1}(\varepsilon_\parallel - \varepsilon_\perp)}_{\epsilon}(E_i E_j - \frac{1}{3}E_k E_k \delta_{ij}) \Bigg) v_{ji} \\ &+ \underbrace{\frac{1}{L_1}}_{L_1}(\partial_k Q_{ij}\partial_k v_{ji}) \\ &+ \underbrace{\frac{(L_2+L_{24})}{L_1}}_{L_2, L_{24}} \left(\frac{1}{2}(\partial_i Q_{kj}\partial_k v_{ji} + \partial_j Q_{ki}\partial_k v_{ji}) - \frac{1}{3}\partial_l Q_{lk}\partial_k v_{ji}\delta_{ij} \right) \\ &+ \underbrace{\frac{L_3}{L_1}}_{L_3} \Bigg(Q_{kl}\partial_l Q_{ij}\partial_k v_{ji} + \frac{1}{2}\partial_i Q_{kl}\partial_j Q_{kl} v_{ji} \\ &- \frac{1}{6}\partial_k Q_{lm}\partial_k Q_{lm}\delta_{ij} v_{ji} \Bigg) \Bigg]\, dV \\ - \oiint_A \underbrace{\frac{\alpha l}{L_1}}_{\alpha} n_i n_j v_{ji}\, dA\end{aligned}$$

which may result in better numerical behaviour (avoiding round-off issues). Note that $a = \left(\frac{l}{\lambda_n}\right)^2$ and $\alpha = \frac{l}{\lambda_s}$ (ratios of lengths) and we set a scaling factor for the electric field $E_s = 1\,\mathrm{V\,\mu m^{-1}} = 1\,000\,000\,\mathrm{V\,m^{-1}}$, which reduces the disparity between ϵ and the other parameters and sets the input for E in $\mathrm{V\,\mu m^{-1}}$ which is more reasonable for our work.

Making this change lowers the range of the parameter space significantly, allowing us to reduce the tolerances of the solver.

Appendix C

Droplet Dynamics: Supplementary Content

C.1 Spherical Droplet Dynamics

This appendix contains supporting information for Chapter 5 of this thesis. Figures C.1, C.2 and C.3 show visualizations of the formation, field-switching, and field release dynamics for a spherical droplets with aspect ratio $R = 1.05$ ($R \approx 1$) where the domain is slightly prolate to prevent. This eliminates a possible degeneracy in alignment which can result in a saddle point in the free energy leading to anomalous dynamics [89]. These figures are analogous to the dynamics visualizations for oblate and prolate droplets, which are presented in the main text.

C.2 Droplet Order Parameter Dynamics

Figure C.4 presents alternative plots for the evolution of the droplet order parameter S_d for spherical, oblate, and prolate droplets, with the time axis being plotted on a logarithmic scale.

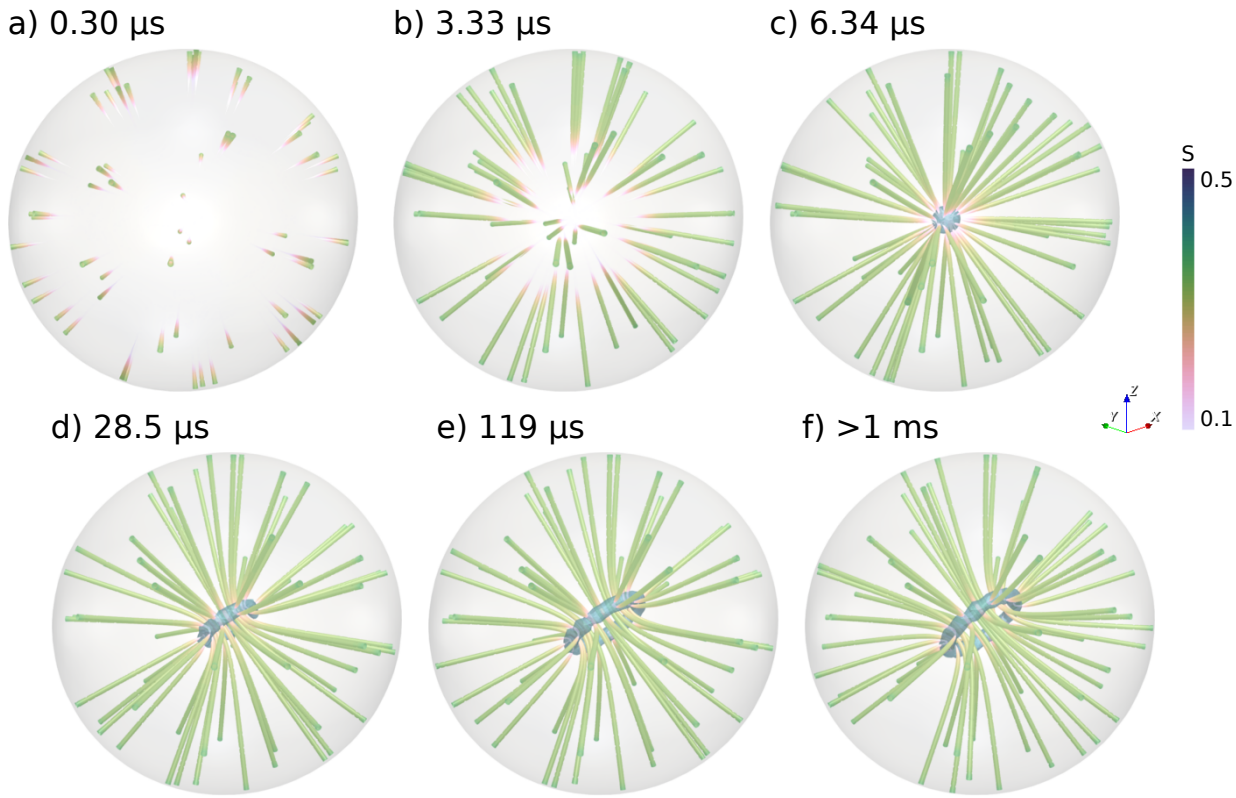

Figure C.1: Visualizations of the formation process of a spherical ($R \approx 1$) nematic droplet from an initially isotropic state. The defect region is indicated by the isosurface (blue, $P \approx 0.03$).

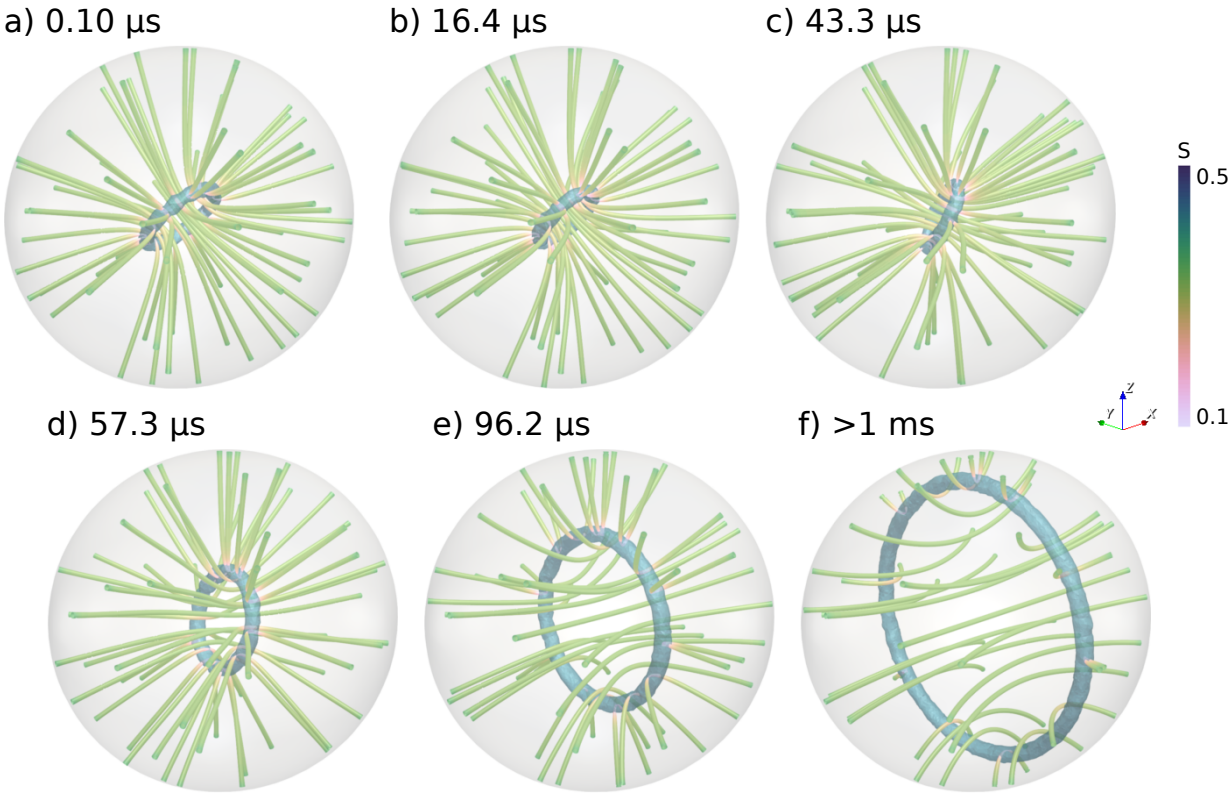

Figure C.2: (a-f) Hyperstreamline visualizations of the electric field-switching process for $E = 14\,\mathrm{V\,\mu m^{-1}} > E_c$ applied along the x-axis of a spherical ($R \approx 1$) nematic droplet starting from (a) the equilibrium texture (following formation) and proceeding to (f) the field-driven equilibrium texture. The defect region is indicated by the isosurface (blue, $P \approx 0.03$).

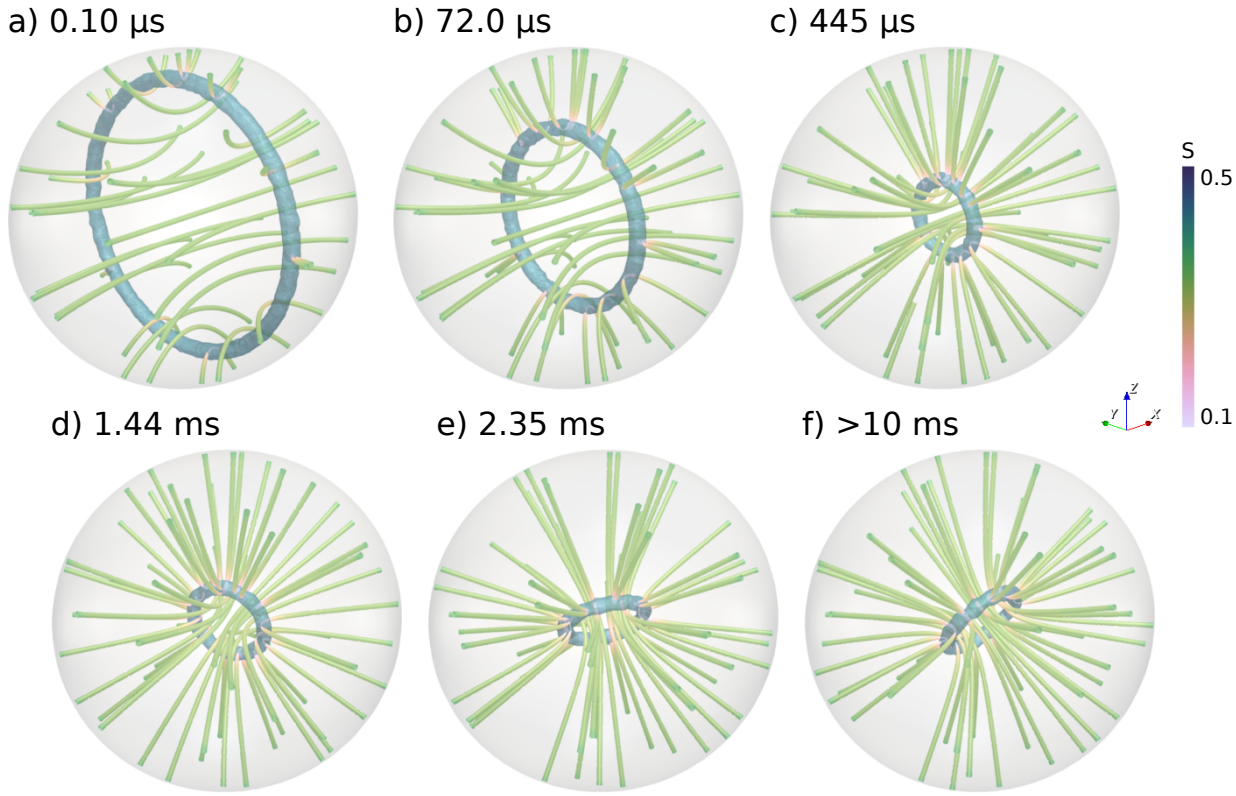

Figure C.3: (a-f) Hyperstreamline visualizations of the field-off relaxation process after applying a field $E = 14\,\mathrm{V\,\mu m^{-1}} > E_c$ along the x-axis of a spherical ($R \approx 1$) nematic droplet starting from (a) the field-on equilibrium texture and proceeding to the (f) the field-off equilibrium texture. The defect region is indicated by the isosurface (blue, $P \approx 0.03$).

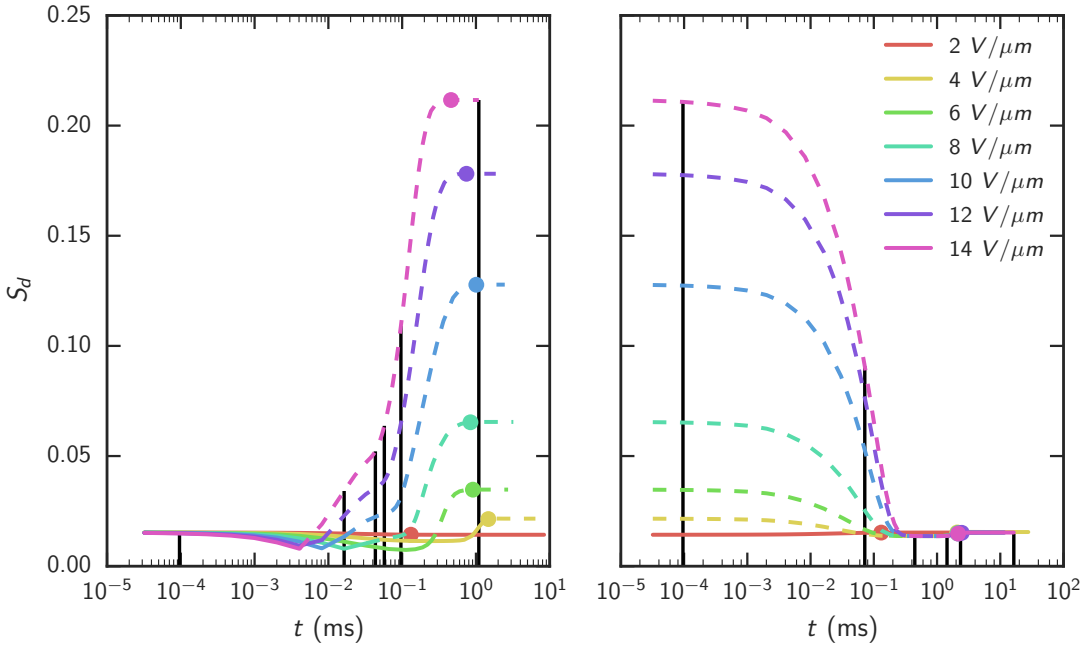
0.25
0.20
0.15
0.10
0.05
0.00
S_d
10^{-5} 10^{-4} 10^{-3} 10^{-2} 10^{-1} 10^{0} 10^{1}
t (ms)
10^{-5} 10^{-4} 10^{-3} 10^{-2} 10^{-1} 10^{0} 10^{1} 10^{2}
t (ms)
2 $V/\mu m$
4 $V/\mu m$
6 $V/\mu m$
8 $V/\mu m$
10 $V/\mu m$
12 $V/\mu m$
14 $V/\mu m$

(a)

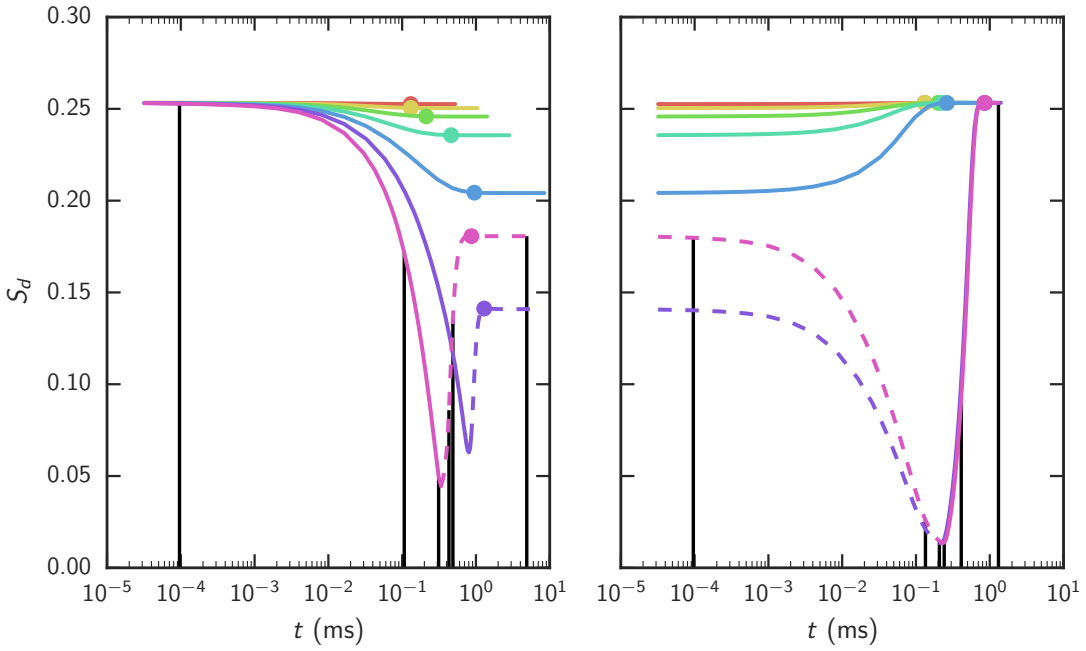
0.30
0.25
0.20
0.15
0.10
0.05
0.00
S_d
10^{-5} 10^{-4} 10^{-3} 10^{-2} 10^{-1} 10^{0} 10^{1}
t (ms)
10^{-5} 10^{-4} 10^{-3} 10^{-2} 10^{-1} 10^{0} 10^{1}
t (ms)

(b)

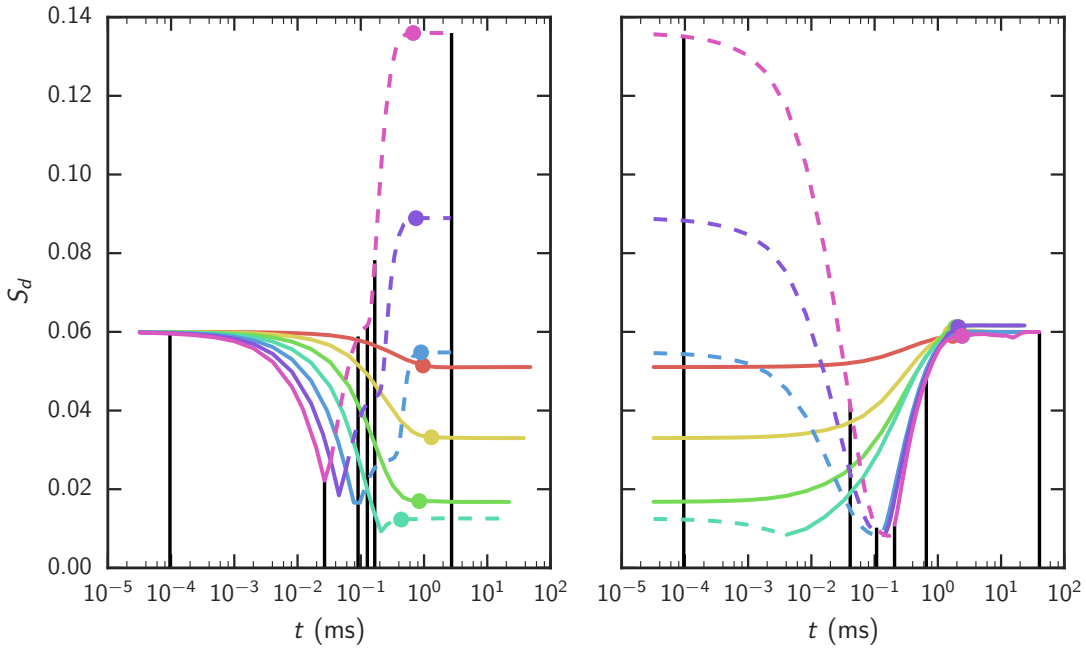

(c)

Figure C.4: Droplet-scale order evolution plots for (a) $R \approx 1$ spherical, (b) $R = 0.5$ oblate, and (c) $R = 2$ prolate nematic droplets resulting from application (left column) and release (right column) of electric fields with strengths ranging from $E = 2$–$14\,\mathrm{V\,\mu m^{-1}}$. Curves represent the droplet scalar order parameter S_d with solid/dotted lines corresponding to the droplet director $\boldsymbol{n}_d$ orthogonal/parallel to the electric field direction. Vertical bars (black) indicate the simulation times at which the corresponding simulation snapshots were taken (see main text). The circle markers denote the estimates for the response times $\tau_{\mathrm{on}}/\tau_{\mathrm{off}}$.